



**UNIVERSITA' DEGLI STUDI ROMA TRE**

SCUOLA DOTTORALE IN GEOLOGIA DELL'AMBIENTE E DELLE RISORSE  
(SDiGAR)

Sezione Geologia Delle Risorse Naturali  
XXVIII CICLO

**PhD Candidate**

Umberto Susta

Dehydration and deprotonation processes in minerals:  
development of new spectroscopic techniques

**Supervisors**

Dott. Fabio Bellatreccia

Prof. Giancarlo Della Ventura

**Reviewers**

Prof. Frank C. Hawthorne  
University of Manitoba

Dr. Roberta Oberti  
CNR Pavia

**Head of the Doctoral School**

Prof. Claudio Faccenna

*A.A. 2014/2015*

## ***Table of Contents:***

Acknowledgements .....	I
Abstract.....	II
Introduction .....	V
Chapter 1. In situ high-temperature XRD and FTIR investigation of hohmannite, a water-rich Fe-sulfate, and its decomposition products.....	1
Chapter 2. High temperature on iron-bearing amphiboles: previous studies ...	12
2.1. The crystal structure of amphiboles .....	13
2.2. Stoichiometry of Fe-oxidation/deprotonation process .....	14
2.3. Possible mechanisms for the process .....	16
2.4. The reduction of crocidolite.....	21
2.5. The kinetics of oxidation of crocidolite .....	27
2.6. Summary .....	29
Chapter 3. Single crystal HT-FTIR spectroscopy of synthetic potassic-ferro-richterite .....	31
3.1. Studied sample and experimental methods .....	33
3.2. Single crystal HT-FTIR spectroscopy.....	34
3.3. Discussion.....	39

---

Chapter 4. Crystal-chemistry of riebeckite from Malawi .....	49
4.1. Experimental methods .....	51
4.2. Experimental results .....	55
4.3. Long Range Order (LRO) .....	61
4.4. FTIR spectroscopy and Short Range Order (SRO) .....	76
Appendix 4.1 .....	80
Chapter 5. HT-FTIR experiments on riebeckite from Malawi .....	81
5.1. Experimental methods .....	82
5.2. Heating FTIR experiments on single crystal.....	83
5.3. HT-FTIR experiments on powders.....	91
Chapter 6. HT-experiments on riebeckite from Malawi: X-ray diffraction and Mössbauer spectroscopy.....	99
6.1. X-ray diffraction on heat-treated single crystals .....	100
6.2. <i>In situ</i> powder diffraction .....	106
6.3. Mössbauer spectroscopy on quenched powders.....	110
Chapter 7. HT-FTIR isothermal experiments and kinetics of deprotonation on riebeckite .....	118
7.1. Isothermal FTIR experiments on single crystals .....	119
7.2. FTIR-FPA imaging on quenched single crystal .....	124



7.3. <i>In situ</i> HT-FTIR on single crystal .....	128
7.4. Isothermal measurements on powders .....	131
7.5. Kinetics of H diffusion in amphiboles.....	135
Chapter 8. Discussion and final remarks.....	141
8.1. The HT study of hohmannite, $\text{Fe}_2[\text{O}(\text{SO}_4)_2 \cdot 8\text{H}_2\text{O}]$ .....	143
8.2. HT of Fe-rich amphiboles.....	144
References.....	156

## Acknowledgements

First of all I would like to thank my supervisors Dr. Fabio Bellatreccia and Prof. Giancarlo Della Ventura for giving me the great opportunity to work together and for their guidance and patience throughout the development of this project.

Thanks to Dr. Francesco Radica for his precious help and for making long days spent in the lab more enjoyable.

I would like to express my gratitude to Prof. Frank Hawthorne for providing me the opportunity to research and work at the University of Manitoba, and for his continued support. I deeply thank Neil Ball, Mark Cooper, Olivier Cagne and Maxwell Day for their help during my stay in Winnipeg.

I am grateful to Dr. Roberta Oberti for her excellent advice throughout the course of this project.

I also thank Dr. Mariangela Cestelli Guidi, Antonio Grilli and the entire staff at the IR lab of INFN in Frascati.

I thank Dr. Gianfelice Cinque for his kind support during our shifts at Diamond Light Source.

I am grateful to Gennaro Ventruti for his kind help during my brief but productive stay in Bari.

A special thank to Dr. Francesco Capitelli for his help in dealing with structural refinements.

Special thanks go to the PhD students of Roma Tre University for their friendship, help and support. In particular I thank Daniele Trippanera, Meisam Tadayon and Daniele La Marra.

Lastly, my deep gratitude goes to my girlfriend Alessandra for being so encouraging in this period. Finally I would like to thank my parents Claudio and Patrizia, my sister Lucia and my grandparents for their support over the years.

---

## Abstract

---

A convenient way to address in detail the mechanisms of dehydration and deprotonation processes in minerals is by using *in situ*-FTIR spectroscopy. This technique allows measuring the variations in the arrangements of either OH or H<sub>2</sub>O molecular groups at the ppm scale, in real-time and directly *in operando*. In this work, high temperature (HT) FTIR methods were preliminarily set-up by studying the dehydration of the Fe-sulfate hohmannite, and then extensively used to study the deprotonation process of iron-rich amphiboles.

The thermal transformation of hohmannite, Fe<sub>2</sub>[O(SO<sub>4</sub>)<sub>2</sub>] · 8H<sub>2</sub>O, a secondary iron-bearing hydrous sulfate, was investigated by *in situ* HT-FTIR spectroscopy. Spectroscopic data were used to complement the X-ray powder diffraction results, allowing to better define the reaction paths for hohmannite and the stability of its HT products. Five dehydration/transformation steps were identified in the heating range of 25 – 800 °C (Ventruti *et al.*, 2015).

Previous HT studies on amphiboles (e.g. Addison *et al.*, 1962a; Ernst and Wai, 1970; Hodgson *et al.*, 1965; Ungaretti, 1980), pointed out a significant coupling between deprotonation and oxidation of Fe<sup>2+</sup>. More recently, oxidation reactions in Fe-rich amphiboles have been considered to be responsible for the enhanced electrical conductivity in subduction zones (Wang *et al.*, 2012).

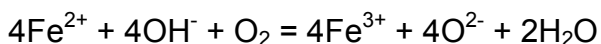
Detailed HT-FTIR experiments were done on a synthetic Fe-rich richterite close to Na(Na,Ca)<sub>2</sub>Fe<sup>2+</sup><sub>5</sub>Si<sub>8</sub>O<sub>22</sub>(OH)<sub>2</sub> and on a riebeckite from Malawi, close to Na<sub>2</sub>Fe<sup>3+</sup><sub>2</sub>Fe<sup>2+</sup><sub>3</sub>Si<sub>8</sub>O<sub>22</sub>(OH)<sub>2</sub>. A multi-methodological approach was used, including HT-FTIR spectroscopy, X-ray powder diffraction, single crystal structural refinement (SREF), and Mössbauer spectroscopy, to characterize possible structural changes induced by increasing temperature. The main results obtained during this study are:

1) IR spectra collected *in situ* for both amphiboles show an anomalous and strong increase in the OH-stretching absorption as a function of *T*, whereas data collected on quenched samples show no OH-loss before the deprotonation temperature.

This feature has never been observed before for OH-bearing minerals and cannot be explained based on the tilting of the O-H vector with  $T$  as proposed, for example, for micas (Tokiwai and Nakashima, 2010). We have no final explanation at present for this issue, but such an increase of the OH-stretching intensity seems to be related to the OH-loss mechanism which is active in the studied amphiboles.

2) X-ray single crystal structural refinements (XR-SREF) done by Oberti *et al.* (2016) on potassic-ferro-richterite and those done here on riebeckite are consistent with an oxidation of  $\text{Fe}^{2+}$  to  $\text{Fe}^{3+}$  occurring completely at  $M(1)$ . The same result was obtained by Mössbauer spectroscopy done on heat-treated riebeckite. Refinement of cell-parameters for both potassic-ferro-richterite (Oberti *et al.*, 2016) and riebeckite (this study) showed an abrupt contraction of the unit cell dimensions in the 350-450°C, and 400-500°C  $T$  range for potassic-ferro-richterite and riebeckite respectively. Such a feature is compatible with oxidation of  $\text{Fe}^{2+}$  at the octahedral sites, coupled to H-loss, responsible in particular, for the contraction along the  $a^*$  crystallographic direction. HT-FTIR experiments done on both amphiboles show in fact the disappearance of the OH-stretching absorption in the same  $T$  range, although a significant shift is observed in the deprotonation  $T$  when comparing data from both techniques. This shift is particularly significant for data collected on single-crystals.

3) HT-FTIR experiments done on riebeckite powders embedded in KBr matrix showed no hydrogen loss after 180 minutes at 520°C, suggesting that, in agreement with previous authors (Addison *et al.*, 1962a; Ernst and Wai, 1970) the Fe-oxidation process, coupled/responsible for the deprotonation process, occurs basically at the crystal surface, where interaction with the atmospheric oxygen is possible. HT-FTIR experiments done on single crystals using a  $\text{N}_2$  flux are compatible with this scenario. On the basis of these results, the deprotonation of Fe-amphiboles can be schematically represented as:



The reactants  $\text{Fe}^{2+}$  and  $\text{OH}^-$  are provided by the amphibole, while  $\text{O}_2$  is provided by the external atmosphere. Single-crystal XRD demonstrates that  $\text{Fe}^{3+}$  and  $\text{O}_2^{2-}$  on the

right-side of this equation are still part of the (oxo)-amphibole, while only  $H^+$  is released, by reacting at the crystal surface with external  $O_2$  to produce  $H_2O$ . For the reaction to proceed, there is the need of continuous availability of  $Fe^{2+}$  and H at the crystal surface, and these must be provided by inside the crystal, via electron and proton diffusion. Comparison on the XRD and spectroscopic data suggests that, as expected, the electron diffusion is faster than the H diffusion. Isothermal experiments done on powdered riebeckite yielded an activation energy ( $E_a$ ) for the H diffusion of  $20 \pm 2$  kJ/mol.

Key words: deprotonation of amphiboles, potassic-ferro-richterite, riebeckite, HT-FTIR spectroscopy, single-crystal and powder HT X-ray diffraction, EMP analysis, Mössbauer spectroscopy.

## Introduction

---

### High-temperature infrared spectroscopy

The aim of the present work is the development of micro-analytical FTIR spectroscopic techniques allowing collection of data across the stability fields of rock-forming minerals. This can be possible by using a device able to reach temperatures up to 1200°C and beyond.

Fourier Transform Infrared Spectroscopy (FTIR) is based on the fact that some molecules (functional groups) present within the sample are subject to rotational-vibrational motions; each motion is characterized by specific resonance frequencies, which in turn correspond to discrete and quantized energetic levels. Observed frequencies are a function of the bond-strengths, the mass of the atoms constituting the molecule, and its interaction with the atoms surrounding the molecule both in the NN (nearest-neighbor) and NNN (next-nearest-neighbor environment). This in turns implies that this technique is unique in providing both LRO (long-range order) and SRO (short-range order) information in minerals, an issue that is difficult to address with other methods (typically XRD).

FTIR thus allows to study the crystal-chemical structure of the sample on a short range scale, in particular to analyze the local distribution on the elements through the different coordination sites, and hence characterize the possible differences with respect to their distribution throughout the entire structure of the crystal. Actually, the information on LRO can be derived by other analytical techniques (e.g. X-ray Single Crystal Structural Refinement), and the possible deviations observed in the IR spectra can be attributed to SRO (Hawthorne *et al.*, 1996), pertaining to local cationic arrangements.

FTIR spectroscopy is a very powerful tool to study light elements like H, both as H<sub>2</sub>O and OH<sup>-</sup>. The study of the loss of H<sub>2</sub>O, typical in the transformations of many minerals at high temperature (HT), or of structural protons (e.g. in the case of amphiboles or micas) associated to oxidation processes, is critical in Earth Sciences.

A thorough comprehension of the dehydration and deprotonation processes is useful to define geological/petrological markers, on the basis of the stability fields of the dehydrated/deprotonated phases, and of other structural changes. Furthermore, this technique is also suitable to characterize the stability fields of minerals with industrial relevance, such as zeolites, layer-silicates (clays), cements and ceramic materials, as well as for studying amorphization processes in asbestos.

In order to test the analytical procedures, during this work we preliminarily tested the experimental set-up in stoichiometrically simple compounds, and then applied extensively the technique to address more complex processes.

*In situ* HT measurements were performed using a heating stage which can be inserted directly under the IR microscope (Figure I.1).

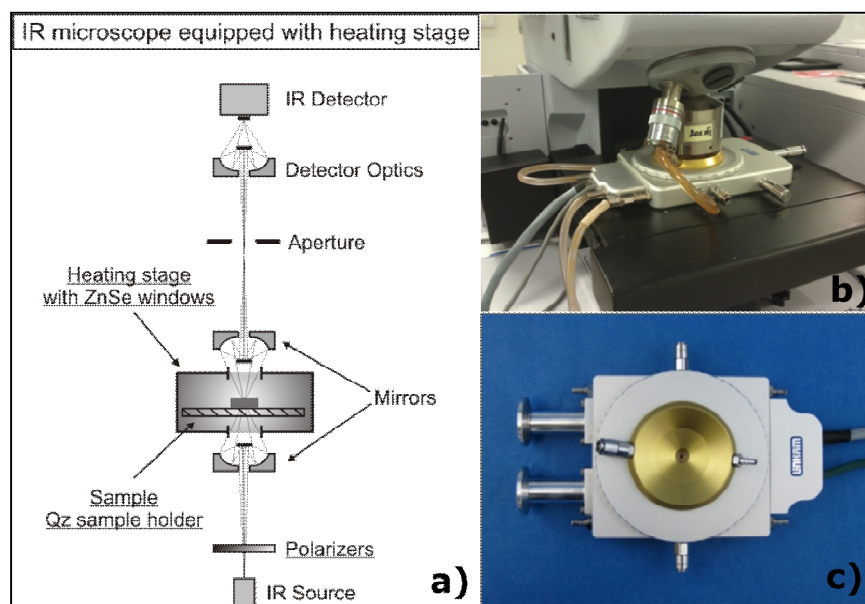


**Figure I.1.** (a) Schematic layout of an infrared-microscope. (b) Photograph of the infrared microscope equipped with the used heating stage, shown in (c).

FTIR spectroscopy can also be applied to the analysis of the spatial distribution of the functional groups by using a bi-dimensional detector (FPA), instead of the conventional point detectors (MCT). This can be done with very short acquisition time, therefore the methodology is suitable for studying both the dehydration kinetics and the coupled diffusion processes in quasi real-time.

## HT-FTIR spectroscopy applied to the transformation of Fe-sulfates

The knowledge of the properties of sulfates is important to define tracers in geology and in planetary geology. Furthermore iron-bearing sulfate minerals are indicators of environmental conditions such as pH, relative humidity, oxygen and sulfate activity in mining and industrial activities. Hence characterization of the different species, their stability fields, transition paths and reaction rates is a critical issue in environmental mineralogy.

Hohmannite typically occurs in sedimentary deposits characterized by arid conditions, moreover it can be associated to other metal-bearing sulfates as an intermediate product in hydrometallurgic processes, thus it has a high industrial relevance.

The HT-FTIR technique was used to investigate the thermal behavior of a sample of hohmannite ( $\text{Fe}_2[\text{O}(\text{SO}_4)_2] \cdot 8\text{H}_2\text{O}$ ) from Chile, and study its transformation path as a function of increasing  $T$ . The data obtained were combined with *in situ* high-temperature X-ray powder diffraction results (Ventruti *et al.* 2015). The published paper is reported in Chapter 1.



## HT-FTIR spectroscopy applied to the deprotonation process of Fe-amphiboles

Oxidation processes in Fe-amphiboles are considered to be responsible for the enhanced electrical conductivity in subduction zones (Wang *et al.*, 2012), however, the actual connection between temperature, Fe-oxidation, loss of hydrogen and electrical conductivity have never been studied in details. Due to the extremely important consequences of this process for both geophysical and material Science applications, most efforts in the present PhD work have been addressed to this topic.

The loss of  $H^+$  in amphiboles is coupled with oxidation of transition elements, in particular Fe. *In situ* FTIR spectroscopy is the only analytical technique that can be used to understand in details the mechanisms of such processes, since it is able to detect variations in OH-group at a ppm scale, real-time and directly at HT. The O-H bond is extremely sensitive to any variation of the local environment induced by HT. In the case of amphiboles the OH-group interacts with the atoms of the surrounding structure at three levels of vicinity. A representation of the local configuration around two OH-groups (black and green spheres linked by a stick) within the structure of an amphibole is given in Figure 1.2.

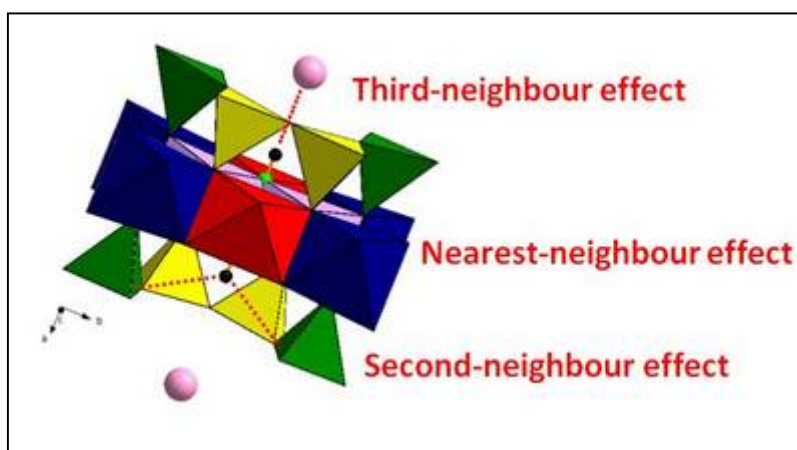


**Figure 1.2.** Graphical representation of the local structural environment around the OH-groups (black-green spheres linked by a stick) within the amphibole structure. The OH-groups interact with the atoms of the structure at three levels of vicinity. See text for description.

The nearest-neighbor effect involves by interaction of the OH-group with the  $M(1)$  and  $M(3)$  octahedra, the second-neighbor effect by interaction with the  $O(7)$  tetrahedral oxygen as well as with cations at the NNN  $M(2)$  and  $M(4)$ -sites, and the third-neighbor effect involves the alkaline site (pink spheres) (Hawthorne and Della Ventura, 2007).

The amphibole samples chosen for the HT experiments are two Fe end-members: (1) synthetic Fe-richterite (ideal composition:  $\text{Na}(\text{NaCa})_2\text{Fe}^{2+}_5\text{Si}_8\text{O}_{22}(\text{OH})_2$ ) is representative of the sodic-calcic amphiboles, common in high-pressure lamproites, and is described in Chapter 3. (2) the second is a riebeckite, a common sodic amphibole with ideal composition:  $\text{Na}_2\text{Fe}^{3+}_2\text{Fe}^{2+}_3\text{Si}_8\text{O}_{22}(\text{OH})_2$  from Malawi (Chapters 4, 5, 6 and 7). This sample was chosen as a test case to address deprotonation/Fe-oxidation process because of its relatively simple chemistry, high Fe content, and wide occurrence in nature as a rock-forming amphibole.

A multi-methodological approach was used, including HT-FTIR spectroscopy, X-ray powder diffraction, single-crystal structural refinement, and Mössbauer spectroscopy, to characterize possible structural changes induced in the sample by increasing temperature.

The data obtained from a set of isothermal HT-FTIR experiments were used to study the kinetics of the deprotonation of riebeckite (Chapter 7), and an estimation of the activation energy of the process.

# **Chapter 1    *In situ*   high-temperature   XRD   and   FTIR investigation of hohmannite, a water-rich Fe-sulfate, and its decomposition products**

---

**G. Ventruti, G. Della Ventura, F. Scordari, U.Susta, A.F. Gualtieri**

**Published on J Therm Anal Calorim (2015), 199. 1793-1802**

# In situ high-temperature XRD and FTIR investigation of hohmannite, a water-rich Fe-sulfate, and its decomposition products

G. Ventruti · G. Della Ventura · F. Scordari ·  
U. Susta · A. F. Gualtieri

Received: 15 April 2014 / Accepted: 16 November 2014 / Published online: 9 December 2014  
© Akadémiai Kiadó, Budapest, Hungary 2014

**Abstract** The thermal dehydration of hohmannite,  $\text{Fe}_2[\text{O}(\text{SO}_4)_2] \cdot 8\text{H}_2\text{O}$ , a secondary iron-bearing hydrous sulfate, was investigated by in situ high-temperature X-ray powder diffraction and in situ high-temperature Fourier transform infrared spectroscopy. Combination of the data from both techniques allowed determining the stability fields and reaction paths for this mineral and its high temperature products. Five main dehydration/transformation steps for hohmannite have been identified in the heating range of 25–800 °C. Temperature behavior of the different phases was analyzed, and the heating-induced structural changes are discussed.

**Keywords** Hohmannite · In situ high-temperature XRPD · In situ high-temperature FTIR

## Introduction

Metal-sulfate and hydrous metal-sulfate minerals are abundant and ubiquitous on the surface of the Earth in diverse environments including acid mine-drainage wastes [1], acid sulfate soils [2], saline lakes [3], hypogene systems

[4], and metallurgical processing plants [5]. They are also known to be present on the surface of Mars [6–9], where they are studied as possible carriers of water [e.g., 10–12].

Iron-bearing sulfate minerals may originate from the weathering of pyrite or pyrrhotite due to bacterial action or to air-oxidation, and are sensitive indicators of environmental conditions such as pH, relative humidity, oxygen activity, and sulfate activity. To obtain information on environmental variables, it is, however, critical to identify and characterize the different species, in terms of chemistry and crystal structure. In addition, knowledge of the properties of sulfates, such as their stability field, transition pathways, and reaction rates, can enhance our understanding of both their technological applications and their use as tracers in geology, and in Mars geology in particular [e.g., 13–15].

Hohmannite,  $\text{Fe}_2[\text{O}(\text{SO}_4)_2] \cdot 8\text{H}_2\text{O}$ , (ICSD card no. 98-003-7328) is a hydrated sulfate of ferric iron typically occurring in sedimentary deposits located in areas characterized by arid conditions (e.g., Sierra Gorda, Chile, e.g., [16]). It has been also identified, associated with other metal-bearing sulfates, as an intermediate product in hydrometallurgical plants [17, 18].

To date, limited data on hohmannite and its thermal stability are available. This mineral belongs to a complex series of variably hydrated compounds: hohmannite, metahohmannite, and amarantite [19, 20], which share structural similarities and close stoichiometries, except a variable water content. According to the single-crystal X-ray diffraction studies [21, 22], the structure of hohmannite is based on centrosymmetric  $[\text{Fe}_4(\text{H}_2\text{O})_8\text{O}_2(\text{SO}_4)_4]$  clusters that polymerize through corner-sharing tetrahedra to form chains of Fe–O–S linkages along the *c*-axis (Fig. 1). Adjacent chains are linked together by hydrogen bonds involving both water molecules linked to  $\text{Fe}^{3+}$  ions and free interstitial ( $\text{H}_2\text{O}$ ) groups. The hydrogen bond

G. Ventruti (✉) · F. Scordari  
Dipartimento di Scienze della Terra e Geoambientali, Università di Bari, via Orabona, 4, 70125 Bari, Italy  
e-mail: gennaro.ventruti@uniba.it

G. Della Ventura · U. Susta  
Dipartimento Scienze Geologiche, Università di Roma Tre, Largo S. Leonardo Murialdo 1, 00146 Rome, Italy

A. F. Gualtieri  
Dipartimento di Scienze Chimiche e Geologiche, Università degli Studi di Modena e Reggio Emilia, L.go S.Eufemia 19, 41121 Modena, Italy

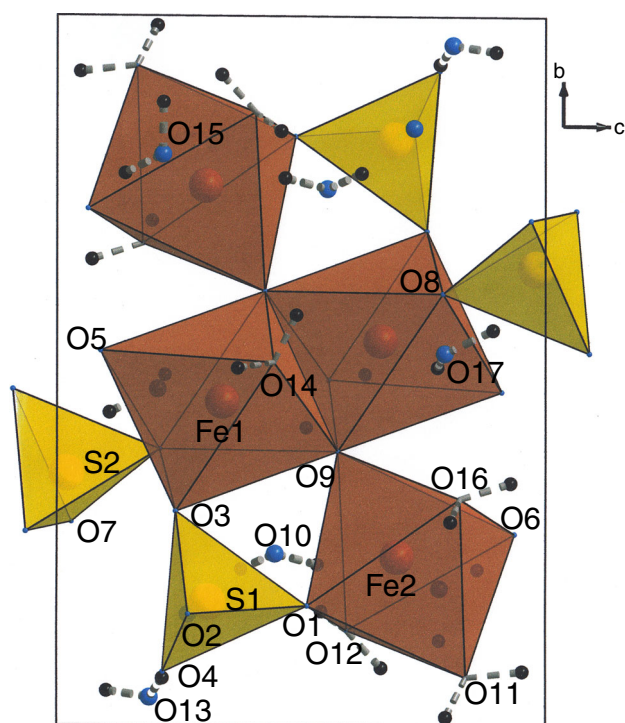


**Fig. 1** The crystal structure of hohmannite viewed along the *a* axis, showing the position of the water molecules

system has been recently investigated through Fourier transform infrared (FTIR), hydrogen position determination by means of difference-Fourier maps, and verified by detailed bond-valence calculations at all relevant oxygen sites [22]. The thermogravimetric analysis performed by Césbron [23] displays four evident mass losses: a first one of about 15 % starting at  $\sim 35$  °C up to a well-defined plateau from 95 to 140 °C, a second one ( $\sim 12$  %) occurring in the 140–240 °C range, and a third one (4.5 %) occurring in the 240–560 °C *T* range, while the last step, from around 560 °C up to 700 °C, is associated to a total mass loss of about 32 %. The differential thermal analysis (DTA) [23] shows three distinct endothermic peaks at about 140, 240, and 745 °C, one endothermic shoulder at about 265 °C and one exothermic peak at 525 °C.

The aim of this work is to investigate the behavior of hohmannite as a function of increasing temperature by combining in situ XRPD, HT-FTIR, and reference thermogravimetric data such as to determine its thermal stability, follow the reaction paths and characterize its high-temperature decomposition products.

## Experimental methods

The crystals investigated in this study were hand picked under a microscope from the original rock specimen from Sierra Gorda (Chile) from which the sample studied by

Scordari [21] had been previously extracted; its chemical composition has been published in [21]. Time-resolved diffraction data were collected at the beamline BM8 (see technical details in [24]) at ESFR (Grenoble, France). The sample was ground in an agate mortar to particle sizes below 400 mesh and packed into a 0.5 mm silica glass capillary open at one end. The capillary was mounted on a standard goniometer head and kept spinning during the collection to increase particle statistics and eliminate preferred orientation effects. Powder data were collected at the fixed wavelength of 0.688808 Å calibrated against the NBS-640b Si standard with  $a = 5.43094(4)$  Å at 25 °C. The sample was heated using a heating gun system; the temperature was varied in the range 22–800 °C at 5 °C min<sup>−1</sup> and monitored with a thermocouple located about 0.5 mm below the capillary. During the heating process, powder diffraction patterns were recorded on the 3 mm slit-delimited portion of a translating imaging-plate detector system (TIPS), mounted perpendicular to the incoming beam [24]. The heating rate of the experiment was synchronized with the speed of the translating system such as to obtain 72 powder patterns with a temperature step separation of about 11 °C. Powder patterns were extracted in the range 4–45° 2 $\theta$  with 0.01° 2 $\theta$  counting step from the stored digitalized file (see [25]) using the original program SCANTIME, developed in house for this purpose.

Rietveld refinements were performed for each powder pattern by means of the GSAS package [26]. The diffraction peaks were modeled using a pseudo-Voigt profile, implemented in GSAS as function number two, with one Gaussian (Gw) and two Lorentzian (Lx and Ly) line-broadening coefficients. The background was fitted with a Chebyshev polynomial function using a relatively high number of parameters (19 coefficients) due to the incoherent contribution of the silica glass capillary. Refinement of the RT pattern was started from the structural model of Scordari [21]. Refinement of metahohmannite obtained from heating hohmannite above 80 °C was carried out using the structural model of Ventruti et al. [20]. Details of the Rietveld refinements at *T* = 33 and 154 °C are reported in Table 1. Refinements of the order–disorder (OD) phase FeOH<sub>2</sub>SO<sub>4</sub> [25, 27] obtained from hohmannite at *T* > 220 °C were also performed by DiffaX+ software [28] in order to model stacking faults along the *c*-axis. Starting parameters were taken from Ventruti et al. [25]. Details of the Rietveld refinement at *T* = 285 °C performed with DiffaX+ are also given in Table 1.

Single-crystal FTIR HT data were collected using a Bruker Hyperion 3000 microscope at INFN (Frascati) over the 2,000–7,000 cm<sup>−1</sup> range between 26 and 600 °C. The temperature step was set at 10 °C, for a 10 °C min<sup>−1</sup> heating rate; the IR spectra were collected immediately when reached the target temperature. For this experiment, a

**Table 1** Crystal data and Rietveld refinement parameters of hohmannite at  $T = 33$  °C, metahohmannite at  $T = 154$  °C, and FeOH $\text{SO}_4$  at 285 °C

	$T = 33$ °C	$T = 154$ °C	$T = 285$ °C
Refinement software	GSAS	GSAS	DiffaX+
Formula	$\text{Fe}_2[\text{O}(\text{SO}_4)_2] \cdot 8\text{H}_2\text{O}$	$\text{Fe}_2[\text{O}(\text{SO}_4)_2] \cdot 4\text{H}_2\text{O}$	FeOH $\text{SO}_4$
Formula weight/ g mol $^{-1}$	462.92	391.87	168.92
Crystal system	Triclinic	Triclinic	Orthorhombic
Space group	$P \bar{1}$	$P \bar{1}$	$Pnma$
$Z$	2	2	4
$D/g \text{ cm}^{-3}$	2.2446	2.5702	3.3443
Unit cell dimensions			
$a/\text{\AA}$	9.1610	7.3379	7.3344
$b/\text{\AA}$	10.9279	9.7675	6.4224
$c/\text{\AA}$	7.2153	7.1481	7.1666
$\alpha/^\circ$	90.566	91.669	90
$\beta/^\circ$	90.546	98.446	90
$\gamma/^\circ$	107.521	86.455	90
Cell volume/ $\text{\AA}^3$	688.72	504.52	337.53
$2\theta \text{ range}/^\circ$	4–45	4–45	4–26
Rp/%	7.03	7.30	7.04
Rwp/%	9.46	9.54	7.17

cleavage fragment, about 20  $\mu\text{m}$  thick, was placed on a CaF $_2$  sample holder within a LINKAM FTIR600 heating stage. Spectra were collected with a Globar source and a KBr beamsplitter, co-adding 128 scans with a nominal resolution of 4  $\text{cm}^{-1}$ .

## Experimental results

### X-Ray powder diffraction data (XRPD)

Examination of the XRPD data shows that hohmannite is stable up to  $\sim 90$  °C (Fig. 2). The evolution of the refined cell dimensions reveals a gradual and anisotropic thermal expansion up to 100 °C (Fig. 3). In particular, the  $a$  and  $c$  parameters increase, with  $a$  showing a steeper slope, while the  $b$  parameter shows a slightly negative trend. The interaxial angles (Fig. 4) also have different behaviors:  $\alpha$  and  $\beta$  decrease, with  $\beta$  showing the largest variation, while  $\gamma$  increases. The cell volume (Fig. 5) shows a linear expansion up to 100 °C. The thermal dependence of lattice parameters and volume of hohmannite over the range 22–100 °C were determined by least-squares regression analysis to calculate thermal expansion coefficients [29]. The following values were found:  $\alpha_a = 9.8(2) \times 10^{-5} \text{ K}^{-1}$ ,  $\alpha_b = -2.4(4) \times 10^{-6} \text{ K}^{-1}$  and  $\alpha_c = 1.9(2) \times$

$10^{-5} \text{ K}^{-1}$ ,  $\alpha_v = 8.0(7) \times 10^{-5} \text{ K}^{-1}$ . Axial expansion is strongly anisotropic with  $\alpha_a:\alpha_b:\alpha_c = 1:-0.02:0.19$ .

The hohmannite structure collapses in the  $T$  range 100–120 °C, while metahohmannite (ICSD card no. 98-009-8821) starts growing in the 80–100 °C temperature range, and becomes the predominant phase for  $T \geq 110$  °C [20]. This first phase transition is in agreement with the thermal analysis data of Césbron [23]: the abrupt mass loss of 15 %, which occurs in this  $T$  range, corresponds with the release of four water molecules from hohmannite (theoretical mass loss 16 %). FTIR spectroscopy (see below) is also in agreement with the water release from the system, although providing a slightly higher  $T$  for this transition ( $\sim 150$  °C).

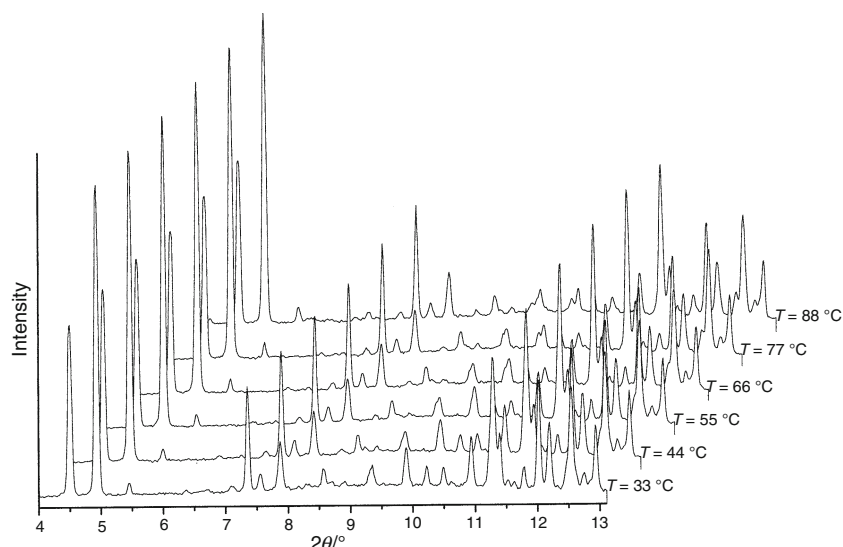
The loss of four water molecules causes the shortening of the chain separations along the  $a$  and  $b$  crystallographic directions (Fig. 3), the rearrangement of the remaining H $_2$ O molecules into a new hydrogen bonding system, and a change in the relative orientation of  $[\text{Fe}_4(\text{H}_2\text{O})_8\text{O}_2(\text{SO}_4)_4]$  clusters to adapt to the new framework [20]. The backbone of the structure, i.e., the  $[\text{Fe}_2(\text{H}_2\text{O})_4\text{O}(\text{SO}_4)_2]$  chain, is, however, topologically the same in both hohmannite and metahohmannite, and this is reflected in the very similar thermal behavior of their cell with  $T$ , see the volume as an example (Fig. 5). The thermal expansion coefficients of metahohmannite were determined to be  $\alpha_a = 3.8(2) \times 10^{-5} \text{ K}^{-1}$ ,  $\alpha_b = 5.2(4) \times 10^{-6} \text{ K}^{-1}$ , and  $\alpha_c = 3.8(4) \times 10^{-5} \text{ K}^{-1}$ ,  $\alpha_v = 8.5(3) \times 10^{-5} \text{ K}^{-1}$ . The axial expansion is again strongly anisotropic with  $\alpha_a:\alpha_b:\alpha_c = 1:0.14:1.0$ .

At about 190 °C, the overall intensity of the metahohmannite diffraction reflections starts decreasing with the simultaneous increase of the background, indicating early amorphisation of the sample, while the peaks of the layered phase FeOH $\text{SO}_4$ , (ICSD card no. 98-002-4079) start showing up. The decomposition of metahohmannite involves the loss of three water molecules directly coordinated by the  $\text{Fe}^{3+}$  ions determining the breakdown of the  $[\text{Fe}_2(\text{H}_2\text{O})_4\text{O}(\text{SO}_4)_2]$  chain and the consequent formation of an intermediate amorphous phase from which the FeOH $\text{SO}_4$  compound originates, according to a typical nucleation and growth reaction process [25]; notably, the same process was observed in the case of sideronatrite [30] a sodium-iron hydrous sulfate with composition  $\text{Na}_2\text{Fe}(\text{SO}_4)_2(\text{OH}) \cdot 3\text{H}_2\text{O}$ . This water loss step is again in accordance with the TG data of Césbron [23], which show a mass loss of  $\sim 12$  %, in the 140–240 °C range.

At about 220 °C, the powder consists of only FeOH $\text{SO}_4$ ; the XRPD data show that this compound is the main phase up to at least 300 °C, while for higher  $T$  the diffraction peaks of  $\alpha$ -Fe $\text{SO}_4$  (ICSD card no. 98-002-3907) appear in the assemblage. Ventruti et al. [25] refined the structure of the FeOH $\text{SO}_4$  compound and described its order–disorder character as revealed by accurate analysis of the X-ray



**Fig. 2** The 3-dimensional plot ( $2\theta$ -intensity-temperature) extracted by integration of the recorded IP data in the temperature range 33–88 °C



pattern. Following their method, successful full-profile refinements of  $\text{FeOH}\text{SO}_4$  at various temperatures were performed here by means of two different methodological approaches: (1) a Le Bail refinement using the Johansson model [31], excluding the Bragg peaks due to stacking disorder; (2) a Rietveld refinement using the DiffaX+ software to model the planar disorder for a finite ensemble of equivalent layers stacking along the  $c$ -axis direction [25]. Only one layer was sufficient to describe the OD structure; the layer was built up from the Johansson model after the interchange of the  $b$  and  $c$  axes. All ordered and disordered stacking sequences of equivalent layers were obtained by ranging the  $\alpha_{11}$  probability of stacking of equivalent layers by the  $(\pm 1/2, 0, 1)$  vector and the  $\alpha_{12}$  ( $= 1 - \alpha_{11}$ ) probability of stacking. The best fit to the observed powder pattern was obtained with  $\alpha_{11} = 0.61$ . Rietveld refinements were performed for patterns collected in the 230–350 °C range (Fig. 6), where the  $\text{FeOH}\text{SO}_4$  compound is the unique or the predominant phase in the powder. Lattice parameters trends determined by both GSAS and DiffaX+ are in agreement. A linear increase of  $b$  and  $c$  and a decrease of the  $a$  cell dimension are observed; the evolution of the cell volume is displayed in Fig. 7. The thermal expansion coefficients for  $\text{FeOH}\text{SO}_4$ , calculated between 230 and 350 °C, are  $\alpha_a = -8.5(6) \times 10^{-6} \text{ K}^{-1}$ ,  $\alpha_b = 2.9(3) \times 10^{-6} \text{ K}^{-1}$  and  $\alpha_c = 1.43(7) \times 10^{-5} \text{ K}^{-1}$ ,  $\alpha_V = 8.6(6) \times 10^{-6} \text{ K}^{-1}$ ; axial expansion is strongly anisotropic along the stacking direction. At about 300 °C, the first diffraction peaks of  $\alpha$ - $\text{FeSO}_4$  appear; its amount increases slightly up to 500 °C, and then decreases suddenly at 550 °C. Reflection peaks of the rhombohedral  $\text{Fe}_2(\text{SO}_4)_3$  compound, (ICSD card no. 98-002-2368), are evident (Fig. 8a) in the diffraction pattern of the material heated to  $\sim 440$  °C and persist in the assemblage up to  $\sim 750$  °C.

The X-ray powder pattern at 500 °C shows the first appearance of an unknown phase, as indicated by the diffraction peaks at  $\sim 11.93$ ,  $7.27$ ,  $7.21$ , and  $7.11$  Å ( $\sim 7.4^\circ$ ,  $12.16^\circ$ ,  $12.25^\circ$ , and  $12.45^\circ$   $2\theta$ , respectively, in Fig. 8b). Over the next 50 °C of heating, the intensity of these peaks increases while the  $\text{FeOH}\text{SO}_4$  peaks decrease, and in fact disappear at  $\sim 550$  °C. This unknown compound is present only in the range 493–668 °C; according to previous studies [32–34], it has a composition  $\text{Fe}_2\text{O}(\text{SO}_4)_2$ . Its amount in the assemblage was estimated in a semi-quantitative way [35] by using the intensity variation of its main reflections at  $12.16^\circ$ ,  $12.25^\circ$  ( $2\theta$ ) in the pattern. In particular, being this compound ( $x$  phase) chemically and structurally close to  $\text{FeOH}\text{SO}_4$ , the density of its unit cell ( $\rho_x$ ) is assumed to be equal to  $\rho_{\text{FeOH}\text{SO}_4}$ , and the mass absorption coefficient of the mixture ( $\mu^*$ ), normalized to the instrumental-geometric-structural constant ( $k$ ), is calculated using the intensities  $I_{hkl, \text{FeOH}\text{SO}_4}$  whose mass ( $w_{\text{FeOH}\text{SO}_4}$ ) is determined from the Rietveld refinements as

$$\mu^* / k = (w_{\text{FeOH}\text{SO}_4} \bullet I_{hkl, \text{FeOH}\text{SO}_4}) / \rho_{\text{FeOH}\text{SO}_4} \quad (\text{a})$$

At higher temperature, up to 740 °C, hematite  $\alpha$ - $\text{Fe}_2\text{O}_3$  (ICSD card no. 98-004-0142) is the only predominant phase, together with minor  $\text{Fe}_2(\text{SO}_4)_3$ .

#### In situ HT-FTIR spectroscopy

In situ evolution of the  $\text{H}_2\text{O}$  absorption in the infrared as a function of  $T$  can be monitored using bands in different regions of the spectrum: (1) the combination region, where  $\text{H}_2\text{O}$  and  $\text{OH}$  may be distinguished from each other because their contributions occur at different wavenumbers (around  $5,100$  and  $4,200 \text{ cm}^{-1}$  for  $\text{H}_2\text{O}$  and  $\text{OH}$ , respectively, e.g., [30, 36]); (2) the stretching region  $3,700$ – $3,000 \text{ cm}^{-1}$ , where

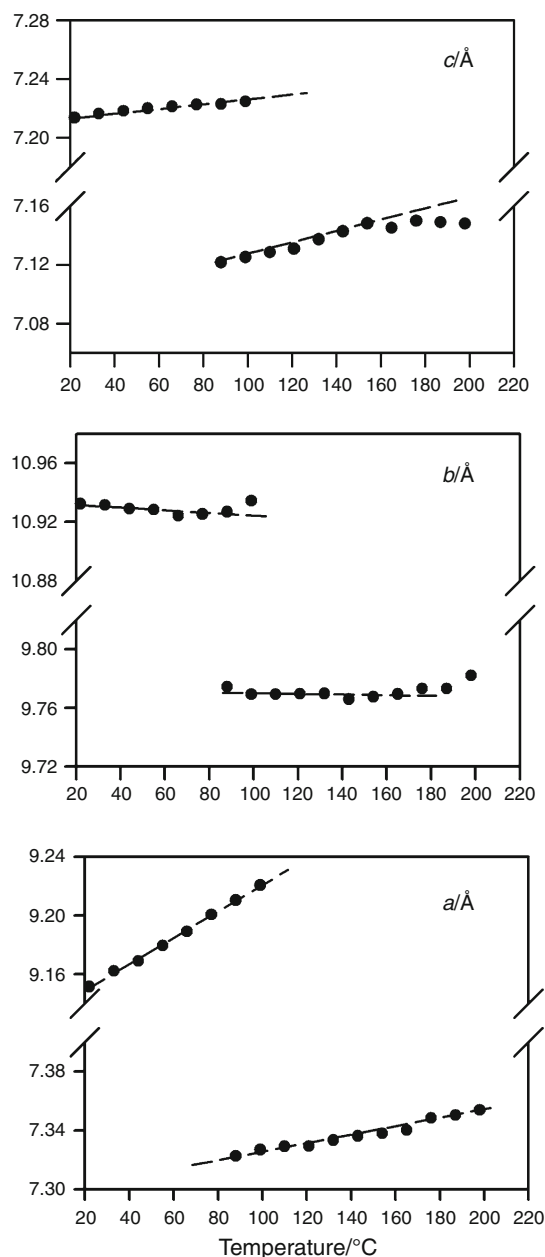


**Fig. 3** Evolution of the cell parameters of hohmannite (20–100 °C range) and metahohmannite (80–200 °C range) computed by Rietveld refinement of in situ XRPD patterns. Standard deviations are smaller than the used symbols; *broken lines* are a guide for the eye

the modes of H<sub>2</sub>O and OH overlap, and (3) the H<sub>2</sub>O bending region (1,600–1,630 cm<sup>-1</sup>). Unfortunately, for hohmannite the absorption in the principal stretching 3,700–3,000 cm<sup>-1</sup> region is too intense, due to the high water content, thus, the signal at room-*T* is out of scale, even for crystal thickness of 20–30 μm. For this reason, in the present study, it was chosen to combine the results collected on a single crystal in the H<sub>2</sub>O/OH combination and bending regions. The evolution of the H<sub>2</sub>O combination mode is displayed in Fig. 9. In this range, the spectra collected up to 40 °C show a relatively

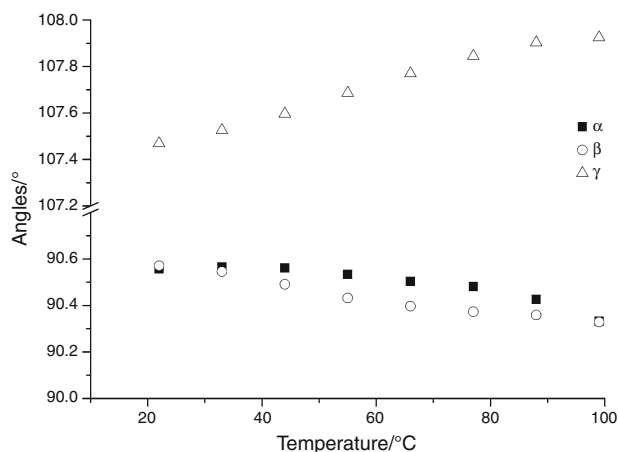


**Fig. 4** Evolution of the interaxial angles of hohmannite up to 100 °C

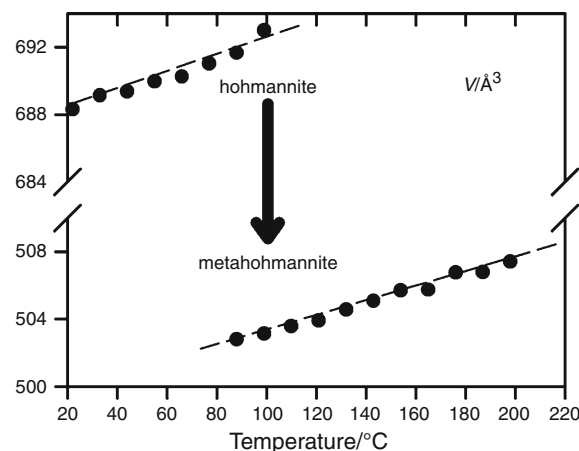


**Fig. 5** Evolution of the cell volume of hohmannite (20–100 °C range) and metahohmannite (80–200 °C range) calculated by Rietveld refinement of in situ XRPD patterns. Standard deviation is smaller than the used symbols; *broken lines* are a guide for the eye

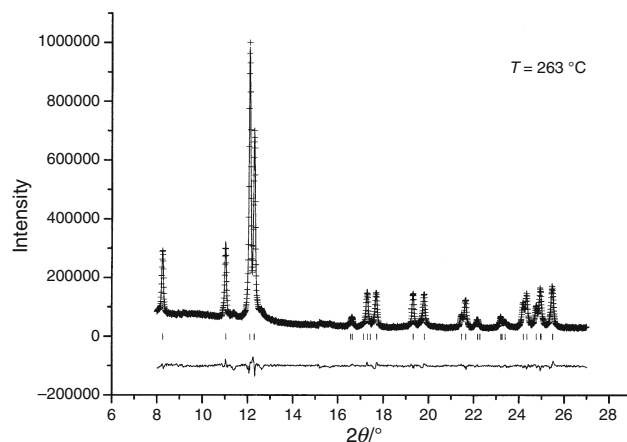


**Fig. 6** Rietveld refinement results for the FeOHSO<sub>4</sub> compound. The *crosses* represent the observed data points, and the *smooth line* through them the calculated pattern using DiffX+



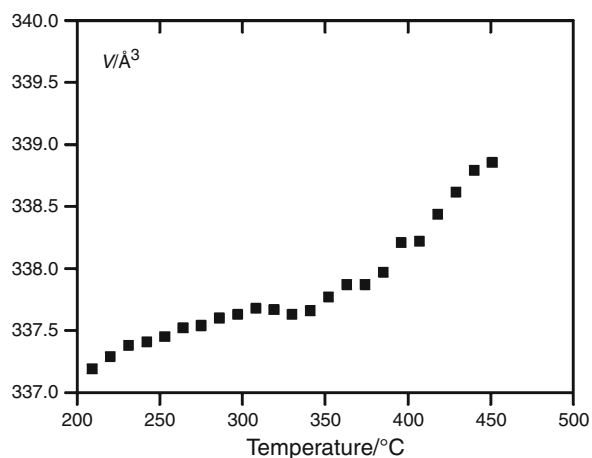


**Fig. 7** Evolution of the cell volume of  $\text{FeOH(SO}_4)_2$  (200–450 °C range) determined from the by Rietveld refinement of in situ XRD patterns (data from GSAS). Standard deviations are smaller than the used symbols

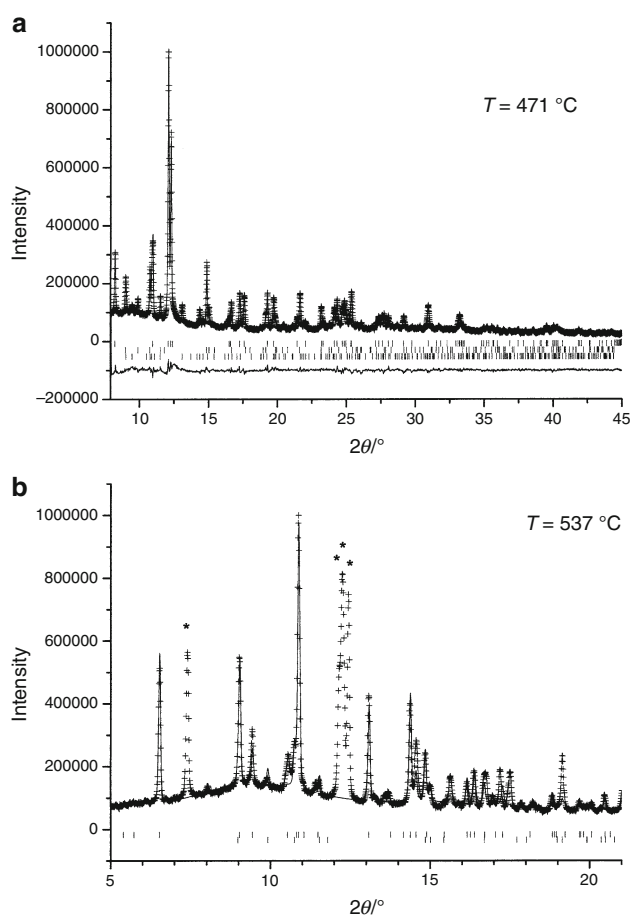


**Fig. 8** Observed, calculated and difference powder patterns, from Rietveld refinements of in situ collected data at **a**  $T = 471$  °C, and **b**  $T = 537$  °C. The *asterisk* symbol indicates peaks of the phase  $\text{Fe}_2\text{O(SO}_4)_2$ . For the explanation, see text

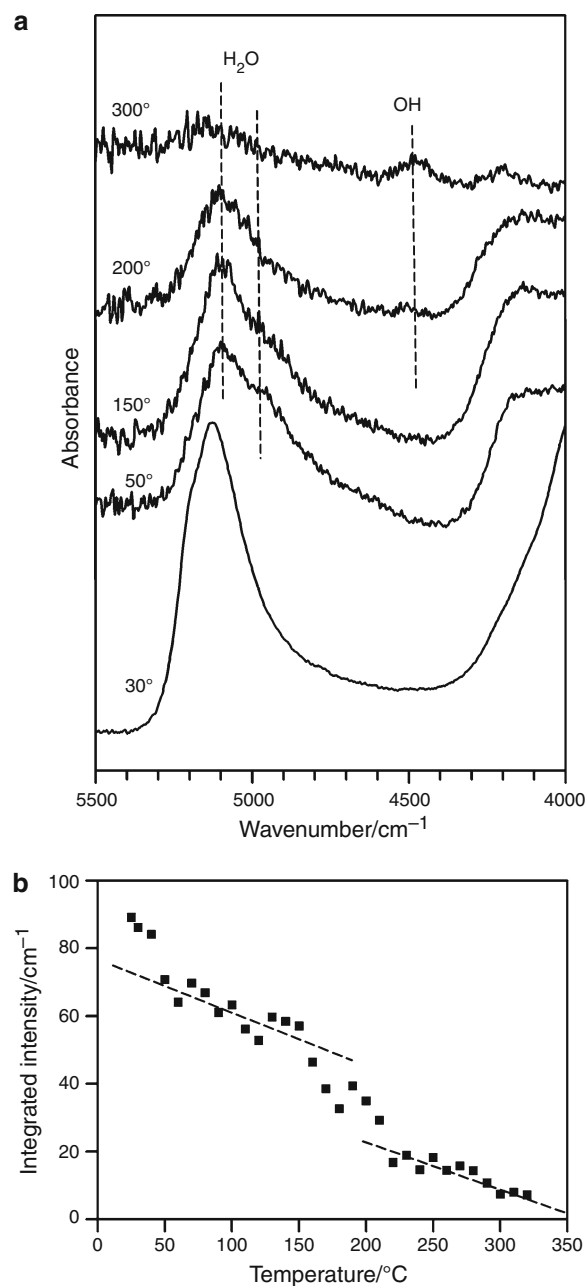


**Fig. 9** **a** In situ FTIR spectra in the 5,500–4,000  $\text{cm}^{-1}$  NIR region; **b** evolution of the integrated intensity of the  $\text{H}_2\text{O}$  combination band at 5,300–4,800  $\text{cm}^{-1}$  as a function of increasing  $T$ ; *broken lines* are a guide for the eye

broad band, at 5,128  $\text{cm}^{-1}$ , with a shoulder at 5,190  $\text{cm}^{-1}$ . The spectrum at 50 °C is significantly different (Fig. 9a), with a much broader band, peaked at 5,046  $\text{cm}^{-1}$  and a shoulder at 4,980  $\text{cm}^{-1}$ . This pattern remains constant for higher  $T$ , and the band gradually reduces its intensity, until complete dehydration. Figure 9b shows a continuous decrease of the band area as a function of  $T$ . At  $\sim 150$  °C, the intensity is halved with respect to its original value. For  $150 < T < 210$  °C, the dehydration proceeds with a steeper

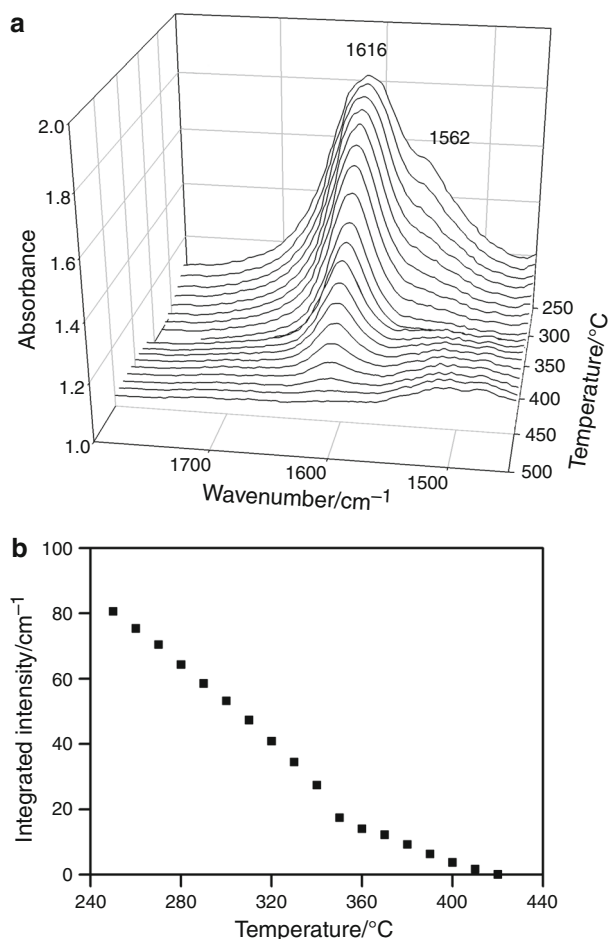


**Fig. 10** **a** In situ FTIR spectra in the 1,800–1,400 cm<sup>-1</sup> region; **b** evolution of the integrated intensity of the H<sub>2</sub>O bending mode as a function of increasing  $T$

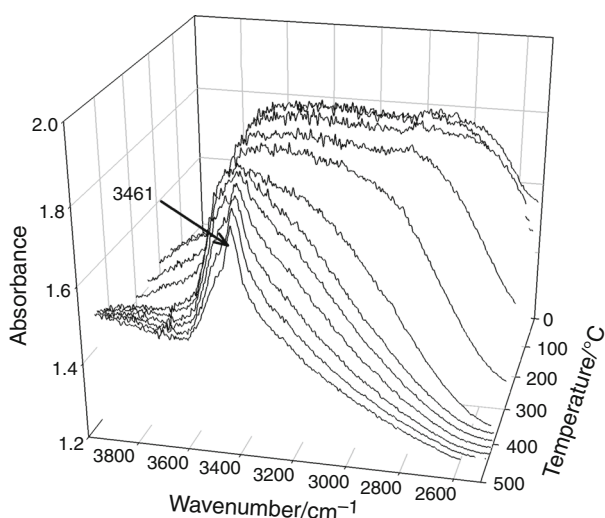


**Fig. 11** **a** In situ FTIR spectra in the 4,000–2,500 cm<sup>-1</sup> region; **b** evolution of the integrated intensity of the H<sub>2</sub>O stretching mode as a function of increasing  $T$

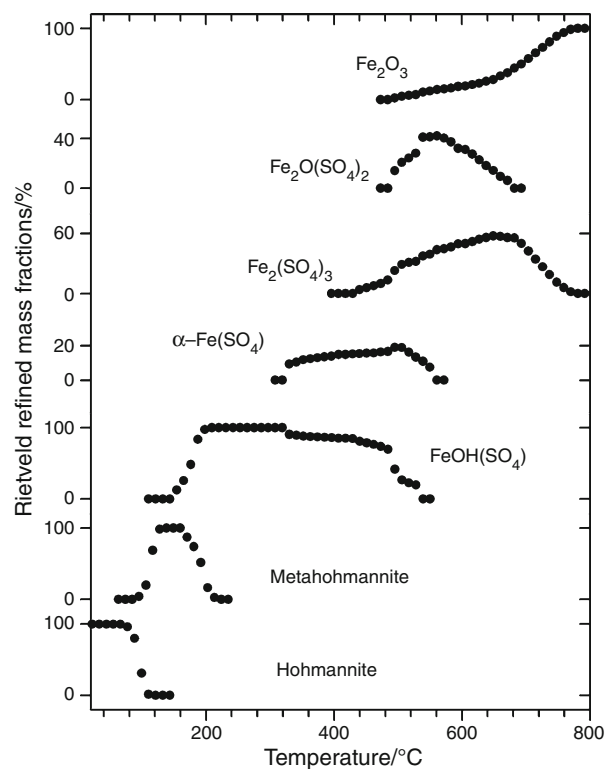


**Fig. 12** Rietveld-refined relative amounts of phases due to the thermal treatment of hohmannite over the entire 22–800 °C temperature range. Standard deviation is smaller than the used symbols

slope; at 210 °C, ~20 % of the initial H<sub>2</sub>O content is retained in the sample; at 350 °C, the combination band is no more visible. For  $T < 250$  °C, the H<sub>2</sub>O bending mode is out of scale; for higher  $T$ , it shows two well-evident components at 1,616 and 1,562 cm<sup>-1</sup>, respectively (Fig. 10a). For  $T > 350$  °C, the higher frequency component disappears, and the 1,616 cm<sup>-1</sup> band keeps decreasing in intensity; at 420 °C it disappears, indicating that at this temperature all H<sub>2</sub>O has been released. The evolution of the bending peak is displayed in Fig. 10b, where the change in the slope at 350 °C is due to the disappearance of the 1,562 cm<sup>-1</sup> component. For  $T > 420$  °C, a relatively sharp band at 3,461 cm<sup>-1</sup> is still present in the OH stretching region of the spectrum (Fig. 11). On the basis of the XRD data, this band can be assigned to the OH groups in the FeOH(SO<sub>4</sub>) compound and it disappears above 530 °C.

In summary, analysis of the different H<sub>2</sub>O/OH bands in the HT-FTIR spectra allows us to conclude that during the heating experiment, under the used conditions, H<sub>2</sub>O is continuously released from the sample and disappears at 420 °C. At ~210 °C, OH hydroxyl groups appear in the spectra (Fig. 10a), together with the appearance of the FeOH(SO<sub>4</sub>) compound in the system. The OH groups disappear for  $T > 530$  °C, in agreement with the diffraction data showing the breakdown of the FeOH(SO<sub>4</sub>) compound at these  $T$  conditions.

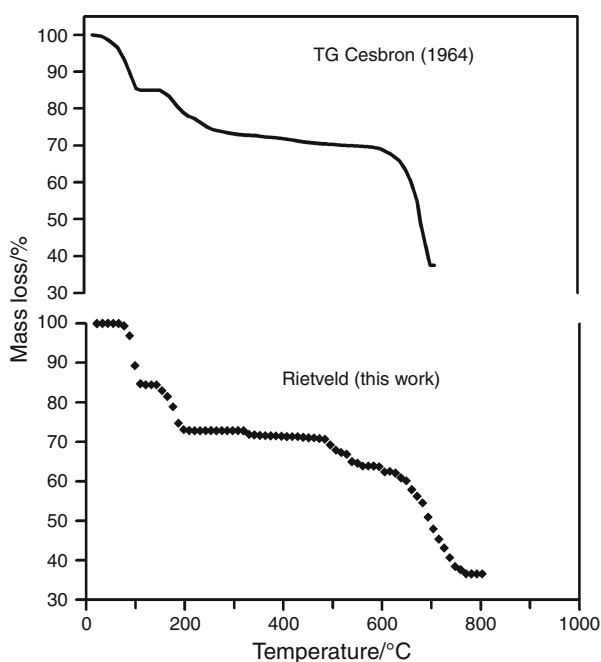


**Fig. 13** Above TG curve redrawn from the image given in Cesbron [23]; below mass loss calculated from the Rietveld-refined phase fractions

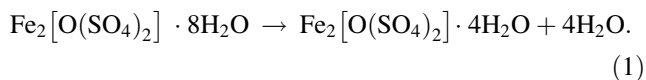
## Discussion and conclusions

In situ synchrotron X-ray diffraction data combined with IR spectroscopy analysis and with the aid of available TG and DTA data [23] provide insight into the dehydration mechanisms produced during heating of hohmannite, and allows following step-by-step the temperature-induced solid-state transformations as well as the structural changes occurring in this system as a function of increasing temperature.

Rietveld refinement of in situ powder diffraction patterns permitted to identify and quantify (mass fractions) the various phases occurring in the decomposition of hohmannite as a function of temperature. The data are presented in Fig. 12, which displays the complex sequence of structural/chemical transformations occurring in the studied system from RT up to 800 °C.

Examination of Fig. 12 shows that the complete thermal decomposition of hohmannite occurs in five steps. These steps are schematically summarized as follows:

1. first step at 80–120 °C: hohmannite–metahohmannite transition transformation, according to



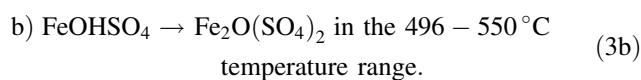
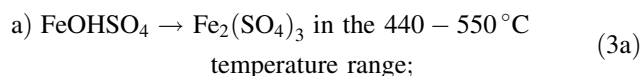
This step involves the release of ~15 mass% water, as it is shown by both TG and FTIR data;

2. Second step at 150–220 °C: decomposition of metahohmannite followed by nucleation and growth of FeOHSO<sub>4</sub> according to



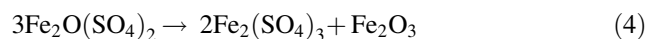
This step involves the release of ~12 mass% water, in accordance with the TG data of Césbron [23]. FTIR spectroscopy shows the appearance of the OH-combination band, and thus of the hydroxyl-bearing Fe-sulfate at 220 °C. The FTIR data in the water bending region (1,600–1,650 cm<sup>-1</sup>) show that weak amounts of H<sub>2</sub>O, connected with both metahohmannite and the amorphous phase, probably persist up to 420 °C.

3. Third step, occurring in the 330–550 °C *T* interval: decomposition of FeOHSO<sub>4</sub> into several Fe–S–O compounds, according to different possible reactions. FTIR spectra show the presence of OH groups, and thus of FeOHSO<sub>4</sub> in the solid products, up to 550 °C. The reaction pathway of the thermal decomposition of FeOHSO<sub>4</sub> has been studied by several authors (e.g., [32–34, 37, 38]), although subjected to some controversy. Most of these authors observed that the thermal decomposition of FeOHSO<sub>4</sub> is characterized by the formation, at *T* > 490 °C, of an intermediate oxo-sulfate, Fe<sub>2</sub>O(SO<sub>4</sub>)<sub>2</sub>, which is decomposed to Fe<sub>2</sub>O<sub>3</sub> above 540 °C. Based on our data, we think that much of the controversy is mainly due to a misinterpretation of reflection peaks of FeOHSO<sub>4</sub> and Fe<sub>2</sub>O(SO<sub>4</sub>)<sub>2</sub>. Our results (Fig. 12) clearly indicate that the decomposition of FeOHSO<sub>4</sub> occurs in two main steps:



As explained above, minor α-FeSO<sub>4</sub> is also observed, whose amount reaches its maximum at *T* = 500 °C, and then quickly decomposes to rhombohedral Fe<sub>2</sub>(SO<sub>4</sub>)<sub>3</sub> up to 550 °C (Fig. 12). This rapid transformation is consistent with the TG data of Césbron [23], which show a sharp and intense DTA exothermic peak at 525 °C. Moreover, our results agree with the data from a combined TG/DSC mass spectroscopy study [39] on the decomposition of FeOHSO<sub>4</sub> according to which the mass loss starts at about 400 °C, and two endothermic peaks at 563 and 750 °C are associated with the loss of water and sulfur dioxide, respectively. In particular, it can be noticed from the mass-spectrometry analysis that the water loss increases for *T* > 500 °C and reaches a maximum at 568 °C followed by a sudden drop at *T* < 600 °C, in perfect agreement with the two reactions described above.

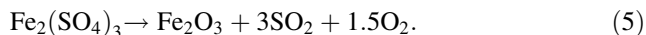
4. In the 550–670 °C *T* range, the Fe<sub>2</sub>O(SO<sub>4</sub>)<sub>2</sub> compound decomposes, according to the reaction:



the TG data of Césbron [23] show a total mass loss of about 32 % in this *T* range which corresponds to the disruption of

SO<sub>4</sub> groups with the subsequent release of SO<sub>2</sub> from the system. Finally,

5. For  $T > 670$  °C, there is the disappearance of Fe<sub>2</sub>(SO<sub>4</sub>)<sub>3</sub> to give hematite, according to



For  $T > 750$  °C, only Fe<sub>2</sub>O<sub>3</sub> is present in the powder.

The Rietveld-refined mass fractions (Fig. 12) were finally used to simulate the mass loss curve which is displayed in Fig. 13. This curve is in excellent agreement with the experimental thermogravimetric curve reported by Césbron [23], thus supporting both the models used to quantify by XRPD the relative phase fractions in the sample and the described transformation reactions.

**Acknowledgements** This work was supported by PRIN 2010–2011 to F. Scordari.

## References

- Bai H, Kang Y, Quan H, Han Y, Sun J, Feng Y. Treatment of acid mine drainage by sulfate reducing bacteria with iron in bench scale runs. *Bioresour Technol.* 2013;128:818–22.
- Fitzpatrick RW, Fritsch E, Self PG. Interpretation of soil features produced by ancient and modern process in degraded landscapes; V. Development of saline sulfidic features in non-tidal seepage areas. *Geoderma.* 1996;69:1–29.
- Glombitza C, Stockhecke M, Schubert CJ, Vetterand A, Kallmeyer J. Sulfate reduction controlled by organic matter availability in deep sediment cores from the saline, alkaline Lake Van (Eastern Anatolia, Turkey). *Front Microbiol.* 2013. doi: [10.3389/fmicb.2013.00209](https://doi.org/10.3389/fmicb.2013.00209).
- Wayne K. Hypogene Karst and sulfate diagenesis of the Delaware Basin: Southeastern New Mexico and Far West Texas, Ph.D Thesis, New Mexico Institute of Mining and Technology, Socorro, New Mexico. 2008.
- Lawrence RW, Marchant PB, Bratty M, Kratochvil D. Applications for biogenic sulphide reagent for copper recovery in copper and gold hydrometallurgical operations. In: *Proceedings of Cu2007, the 6th Copper/Cobre conference, Toronto, August 25–30. 2007.*
- Klingelhöfer G, Morris RV, Bernhardt B, Schröde C. Jarosite and hematite at Meridiani Planum from Opportunity's Mössbauer spectrometer. *Science.* 2004;306:1740–5.
- Johnson JR, Bell JF, Cloutis E, Staid M, Farrand WH, McCoy T, Rice M, Wang A, Yen A. Mineralogic constraints on sulfur-rich soils from Pancam spectra at Gusev crater, Mars. *Geophys Res Lett.* 2007;34:L13202.
- Vicenzi EP, Fries M, Fahey A, Rost D, Greenwood JP, Steele A. Detailed elemental, mineralogical, and isotopic examination of jarosite in Martian Meteorite MIL 03346. 38th Lunar and planetary science conference, (Lunar and Planetary Science XXXVIII), held 12–16 March 2007 in League City, Texas. LPI Contribution No. 1338, p. 2335.
- Lane MD, Bishop JL, Dyar MD, King PL, Parente M, Hyde BC. Mineralogy of the Paso Robles soils on Mars. *Am Mineral.* 2008;93:728–39.
- Gendrin A, Mangold N, Bibring JP, Langevin Y, Gondet B, Poulet F, Bonello G, Quantin C, Mustard J, Arvidson R, Le-Mouélic S. Sulfates in Martian layered terrains: the OMEGA/Mars express view. *Science.* 2005;307:1587–91.
- Bibring JP, Langevin Y, Mustard JF, Poulet F, Arvidson R, Gendrin A, Gondet B, Mangold N, Pinet P, Forget F, The OMEGA Team. Global mineralogical and aqueous mars history derived from OMEGA/Mars express data. *Science.* 2006;312:400–4.
- Wendt L, Gross C, Kneiss T, Sowe M, Combe JPh, LeDeit L, McGuire PC, Neukum G. Mineralogy and stratigraphy of sulfates and ferric oxides in Ophir Chasma, Mars. 42nd lunar and planetary science conference, 1775. 2011.
- Cloutis EA, Hawthorne FC, Mertzman SA, Krenn K, Craig MA, Marcino D, Methot M, Strong J, Mustard JF, Blaney DL, Bell JF III, Vilas F. Detection and discrimination of sulfate minerals using reflectance spectroscopy. *Icarus.* 2006;184:121–57.
- Lu Y, Wang A. Synthesis and spectral characterization of OH-bearing ferric sulfates. XXXXIII Lunar Planet. Sc. Conf., Abstract 2514, Huston. 2012.
- Spratt H, Rintoul L, Avdeev M, Martens W. The thermal decomposition of hydronium jarosite and ammoniojarosite. *J Therm Anal Calorim.* 2014;115:101–9.
- Palache C, Berman H, Frondel C. The system of mineralogy of James Dwight Dana and Edward Salisbury Dana, Yale University 1837–1892, Vol 2, 7th edition. Wiley: New York; 1951.
- Ngenda RB, Segers L, Kongolo PK. Base metals recovery from zinc hydrometallurgical plant residues by digestion method. Hydrometallurgy Conference 2009. The Southern African Institute of Mining and Metallurgy. Symposium Series 54. 2009. pp. 17–29.
- Ruhl AS, Kranzmann A. Corrosion behavior of various steels in a continuous flow of carbon dioxide containing impurities. *Int J Greenh Gas Control.* 2012;9:85–90.
- Strunz H, Nickel EH. Strunz mineralogical tables. chemical structural mineral classification system 9th edition, 870 S., 226 Abb., Best.-Nr. 13-3509. 2001.
- Scordari F, Ventruti G, Gualtieri AF. The structure of metahohmannite, Fe + 32[O(SO<sub>4</sub>)<sub>2</sub>·4H<sub>2</sub>O], by in situ synchrotron powder diffraction. *Am Mineral.* 2004;89:265–70.
- Scordari F. The crystal structure of hohmannite, Fe<sub>2</sub>(H<sub>2</sub>O)<sub>4</sub>[(SO<sub>4</sub>)<sub>2</sub>O]·4H<sub>2</sub>O and its relationship to amarantite, Fe<sub>2</sub>(H<sub>2</sub>O)<sub>4</sub>[(SO<sub>4</sub>)<sub>2</sub>O]·3H<sub>2</sub>O. *Mineral Mag.* 1978;42:144–6.
- G. Ventruti G, Della Ventura G, Orlando R, Scordari F. Crystal structure and vibrational spectroscopy of hohmannite, Fe<sub>2</sub>[(SO<sub>4</sub>)<sub>2</sub>O]·8H<sub>2</sub>O. 2014 (in press).
- Césbron F. Contribution à la Minéralogie des sulfates de fer-hydratés. *Bull Soc Fr Min Cryst.* 1964;87:125–43.
- Meneghini C, Artioli G, Balerna A, Gualtieri AF, Norby P, Mobilio S. Multipurpose imaging-plate camera for in situ powder XRD at the GILDA beamline. *J Synchrotron Radiat.* 2001;8:1162–6.
- Ventruti G, Scordari F, Schingaro E, Gualtieri AF, Meneghini C. The order-disorder character of FeOHSO<sub>4</sub> obtained from the thermal decomposition of metahohmannite, Fe<sub>2</sub><sup>3+</sup>[O(SO<sub>4</sub>)<sub>2</sub>]·4H<sub>2</sub>O. *Am Mineral.* 2005;90:679–86.
- Larson AC, Von Dreele RB. General structure analysis system (GSAS). Los Alamos National Laboratory Report LAUR 86–748. 2000.
- Gomez MA, Ventruti G, Celikin M, Assaoudi H, Putz H, Becze L, Leea KE, Demopoulos GP. The nature of synthetic basic ferric arsenate sulfate [Fe(AsO<sub>4</sub>)<sub>1-x</sub>(SO<sub>4</sub>)<sub>x</sub>(OH)<sub>x</sub>] and basic ferric sulfate (FeOHSO<sub>4</sub>): their crystallographic, molecular and electronic structure with applications in the environment and energy. *RSC Adv.* 2013;37:16840–9.
- Leoni M, Gualtieri AF, Roveri N. Simultaneous refinement of structure and microstructure of layered materials. *J Appl Cryst.* 2004;37:166–73.
- Fei Y. Thermal expansion. In: Ahrens TJ, editor. *Mineral physics and crystallography: a handbook of physical constants*, vol. 2. Washington: American Geophysical Union; 1995. p. 29–44.

30. Della Ventura G, Ventruti G, Bellatreccia F, Scordari F, Cestelli Guidi M. FTIR transmission spectroscopy of sideronatrite, a sodium-iron hydrous sulfate. *Mineral Mag.* 2013;77:499–507.
31. Johansson G. On the crystal structure of  $\text{FeOH}\text{SO}_4$  and  $\text{InOH}\text{SO}_4$ . *Acta Chem Scand.* 1962;16:1234–44.
32. Pelovski Y, Petkova V, Nikolov S. Study of the mechanism of the thermochemical decomposition of ferrous sulphate monohydrate. *Thermochim Acta.* 1996;274:273–80.
33. Petkova V, Pelovski Y. Investigation on the thermal properties of  $\text{Fe}_2\text{O}(\text{SO}_4)_2$ , part I. *J Therm Anal Calorim.* 2001;64:1025–35.
34. Petkova V, Pelovski Y. Investigation on the thermal properties of  $\text{Fe}_2\text{O}(\text{SO}_4)_2$ , part II. *J Therm Anal Calorim.* 2001;64:1037–44.
35. Klug HP, Alexander LE. X-ray diffraction procedures for polycrystalline and amorphous materials. New York: Wiley; 1974.
36. Ventruti G, Scordari F, Della Ventura G, Bellatreccia F, Gualtieri AF, Lausi A. The thermal stability of sideronatrite and its decomposition products in the system  $\text{Na}_2\text{O}-\text{Fe}_2\text{O}_3-\text{SO}_2-\text{H}_2\text{O}$ . *Phys Chem Miner.* 2013;40:659–70.
37. Swamy MSR, Prasad TP. Thermal analysis of iron(II) sulphate heptahydrate in air. V thermal decomposition of hydroxy and oxysulphates. *J Therm Anal Calorim.* 1981;20:107–14.
38. Mahapatra S, Prasad TP, Rao KK, Nayak R. Thermal decomposition of hydrolysis products of  $\text{Fe}(\text{OH})\text{SO}_4$ . *Thermochim Acta.* 1990;161:279–85.
39. Schindler A, Blumm, J. Simultaneous thermal analysis of iron hydroxy sulfate. Application note. 2009. <http://www.azonano.com/article.aspx?ArticleId=2437>.

## **Chapter 2    High temperature experiments on iron-bearing amphiboles: previous studies**

---

A large number of HT studies on the behavior of Fe-amphiboles ("crocidolites") as a function of temperature were published in the 1960-1970's. These studies were prompted by the emerging technical relevance of these minerals in the industry of heat-resistant materials. As it is well known, the use of asbestos has been banned in western countries in the last decades (Basel Convention, 1992) due to their hazardous effects. However, the early papers still represent a precious corpus of information that is fundamental in the interpretation of the data collected during this PhD Thesis.

A quantitative model for the oxidation/reduction of crocidolite, the fibrous form of riebeckite, was provided by Addison *et al.* (1962a, b) who definitively showed how the oxidation of  $\text{Fe}^{2+}$  at 450°C is coupled to a simultaneous loss of hydrogen with production of water. Below we will provide a review of the basic results of the early works, highlighting the most prominent concepts that will be used in the chapters dealing with the experimental results.



## 2.1. The crystal structure of amphiboles

The structure of amphiboles consists in a double chain of corner-sharing tetrahedra and a strip of edge-sharing octahedra, both of which extend in the crystallographic direction  $c$ . The sites occupied by tetrahedrally coordinated cations ( $T$ -group cations) are denoted “ $T$ ”. Two different tetrahedral sites, labeled  $T(1)$  and  $T(2)$  on the basis of bond topology (Hawthorne, 1983), constitute the double chain. The sites occupied by octahedrally coordinated cations ( $C$ -group cations) are denoted “ $M$ ”. The octahedral strip consists of three different octahedral sites, denoted  $M(1)$ ,  $M(2)$  and  $M(3)$ . The  $M(4)$ -sites ensure the connection between the tetrahedral double chain and the octahedral strip, and have variable coordination depending on the  $B$ -group cation occupying the site. The  $A$ -site is located within the hexagonal rings formed by the tetrahedral double chains and can be occupied by  $A$ -cations or be vacant (Hawthorne, 1983). There are seven different anionic sites,  $O(1-7)$ , that are usually occupied by oxygen atoms, though the  $O(3)$ -site may be occupied by  $\text{OH}^-$ ,  $\text{F}^-$ ,  $\text{Cl}^-$  and or  $\text{O}^{2-}$ . A graphical representation of the structure of amphiboles is shown in Figure 2.1.

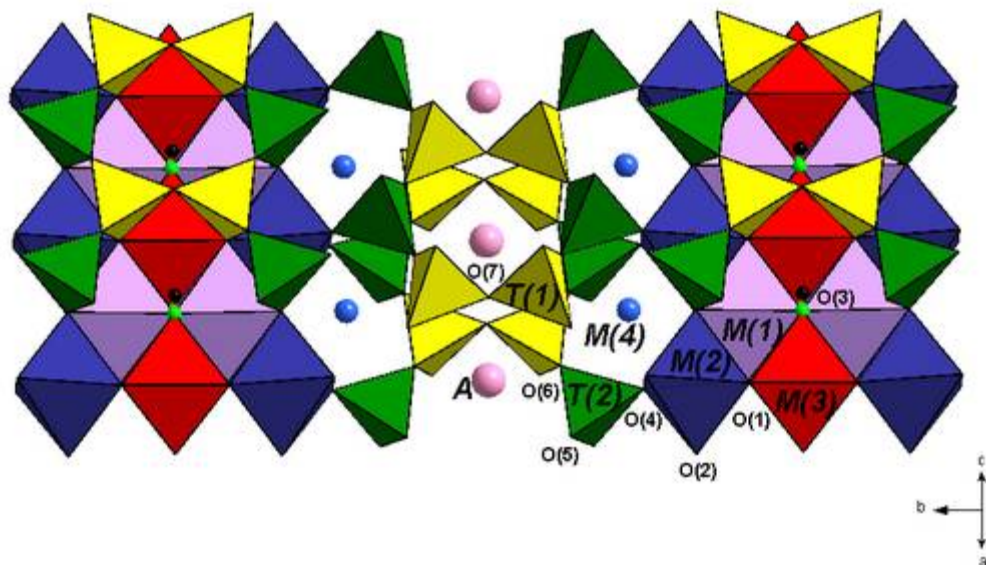
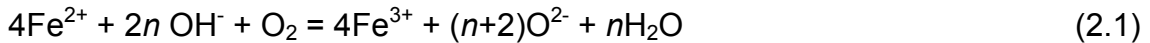


**Figure 2.1.** Graphic representation of the generalized amphiboles structure. The different cationic sites and oxygen positions are indicated. The OH-groups are also depicted with light green and black spheres.

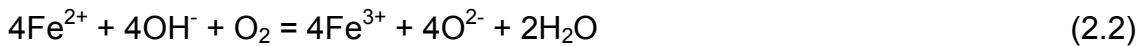
## 2.2. Stoichiometry of the Fe-oxidation/deprotonation process

The earlier study on this topic found in the mineralogical literature is from Barnes (1930) who observed that no structural changes in Fe-poor amphiboles heated in air at about 850°C for 3hrs, while Fe-rich actinolites and hornblendes showed an increase in density, refractive indices, and birefringence, as well as color change from green to brown. Such changes were found to be reversible by retreating the sample in H<sub>2</sub>, and were explained as a consequence of Fe-oxidation rather than of the decrease in water content. By comparing the percent weight loss on heating with the analyzed water content, Barnes (1930) concluded that during the oxidation process, H<sub>2</sub> and not molecular water is lost.

According to Addison and Sharp (1962b), the general equation for the oxidation/deprotonation process in a Fe-bearing mineral heated in air can be represented as:



The value of  $n$  depends on the relative proportions among the three secondary reactions described by the following equations:



Equation 2.2 has been termed by Hodgson *et al.* (1965) “dehydrogenation reaction”. It can be considered a particular case of Equation 2.1 when  $n=2$ ; alternatively it can be derived by adding Equations 2.3 and 2.4 in the ratio 1:2, where the two processes may also occur separately. Equation 2.2 describes the oxidation of Fe<sup>2+</sup> occurring with a simultaneous loss of a proton, with no change in both the number of oxygens and of metal atoms, but only with a loss of hydrogen. It does not cause major changes in the crystal structure but, as shown by X-ray powder patterns of oxidized crocidolite (Addison *et al.*, 1962a), only a small contraction in unit cell dimensions to



accommodate the smaller  $\text{Fe}^{3+}$ . This reaction is supposed to be the predominant mechanism during HT treatments, while Equations 2.3 and 2.4 are possible side-reactions.

Equation 2.3 was termed “oxygenation” by Hodgson *et al.* (1965); it represents an alternative oxidation mechanism of  $\text{Fe}^{2+}$  without simultaneous loss of H, and is supposed to take place on the surface only, when no hydroxyl ions are available. It can be considered a particular case of Equation 2.1 when  $n=0$ . In such a case, these authors reported that a superficial oxide layer is formed, but no major change in the crystal structure occurs. For this reason, they suggested that the amount of  $\text{Fe}^{2+}$  that can be oxidized is dependent on the extent to which the crystal structure can tolerate a gain of oxide ions on the surface, without structural strain. It is worth mentioning that during the experiments done in this Thesis, no proofs for the presence of this oxide layer were observed.

Any further deprotonation of the phase is possible only at higher temperatures thanks to the process described by Equation 2.4 (Addison and Sharp, 1962b). It consists in the elimination of a structural proton, and is supposed to take place, without any oxidation of metals, in all hydroxylated minerals, at relatively high- $T$ . The effect of such process on the structure depends on the mineral phase; in the case of amphiboles it may eventually lead to a completely OH-free oxo-amphibole structure. Successive works (e.g. Phillips *et al.*, 1991) showed that an OH-free oxy-amphibole structure without oxidation of  $M(1,3)$ -metals is prevented, and that the process suggested would lead to the breakdown of the amphibole. A deprotonation without any locally associated Fe-oxidation would also be impossible from a valence-sum perspective (Hawthorne, 1997).

### 2.3. Possible mechanisms for the process

Considering that the diffusion of oxygen into a mineral structure is unlikely, Addison *et al.* (1962a, b) suggested that “dehydrogenation” takes place exclusively on the mineral surface where  $\text{Fe}^{2+}$ ,  $\text{OH}^-$ , and gaseous (atmospheric) oxygen are available. Two factors are needed for the process to proceed: 1) the ions involved in such process (i.e.  $\text{Fe}^{2+}$  and  $\text{OH}^-$ ) must be regenerated on the crystal surface by a mechanism of intra-crystalline diffusion, and 2) the water generated on the surface is continuously removed.

1) According to Addison *et al.* (1962a, b)  $\text{OH}^-$  could be continuously supplied at the surface by hopping of protons on adjacent oxygens from the interior of the crystal. In the same way, the transfer of an electron from a  $\text{Fe}^{2+}$  ion to an adjacent  $\text{Fe}^{3+}$  could ensure an effective presence of the reactant  $\text{Fe}^{2+}$  on the surface. The migration of electrons and possibly protons would require less energy, and hence temperature, than transport of ions. Migration of electrons probably occurs in amphiboles exclusively in the direction of the chain (c-axis), since the distance between octahedral strips is too long. Mössbauer, IR, and X-ray studies on various heat-treated iron-bearing sodic amphiboles are presented in Ernst and Way (1970), and electrical resistivity and Mössbauer experiments were carried out in Schmidbauer *et al.* (2000). These results are in agreement with an electron migration from the initially  $\text{Fe}^{2+}$  ions toward the surface of individual crystals, and with their transfer through the marginal iron cations to external attracted oxygen, which are thereby bound as an anionic surface layer. Addison *et al.* (1962a, b) proposed that the electron transfer can be stopped by ions that cannot accept electrons such as  $\text{Mg}^{2+}$ , consequently the higher the  $\text{Fe}^{2+}$  and the lower the content of  $\text{Mg}^{2+}$  the more easily  $\text{Fe}^{2+}$  can be accessible for oxidation.

2) Water produced on the crystal surface according to Equation 2.1, inhibits the process by separating the reactants. If water is not removed from the surface, any further oxidation has higher activation energy thus requiring higher temperature. It was observed (Addison *et al.*, 1962a) that some oxidation of crocidolite is also possible at 0°C and that, when it is complete, further reaction can be achieved just after removal of water by pumping.

It was also observed that, after the complete oxidation of crocidolite at 450°C, in order to remove all H<sub>2</sub>O produced during oxidation, the sample needed to be immersed into a liquid nitrogen cold trap for at least 12 hours, indicating a very strong retention of surface water. The authors suggested that oxidation process of crocidolite may proceed for hours at a constant rate, independently of the oxygen pressure (unless it becomes too small). This seems compatible with a surface process where a sufficient concentration of Fe<sup>2+</sup> and OH<sup>-</sup> is maintained by electrons and somehow a protons migration.

While according to Equation 2.2 the reaction can stop because of the unavailability of OH<sup>-</sup>, Equation 2.3 suggests that further oxidation is still possible, as long as oxygen ions are available on the surface. Such a mechanism occurs in metals, but is unlikely to happen in silicates without producing a structural collapse. This mechanism is however plausible only at higher temperature, the actual temperature varying from mineral to mineral, depending on the stability of the phase. For amphiboles these kind of structural modifications were suggested to occur in the 920-960°C range, where DTA experiments showed an exothermal peak compatible with an oxidation process (Francis, 1955).

Addison *et al.* (1962a) observed also that water formed by oxidation is slightly less than the amount expected from Equation 2.2; moreover, they also observed that heating to a temperature at which reaction described in Equation 2.3 may occur, some further oxidation of Fe<sup>2+</sup> (5-10%) is feasible.

The activation energy for the oxidation of crocidolite was found to be, by means of DTA experiments, 21 Kcal/mol, which is in good agreement with the value obtained for the diffusion of electrons in the same mineral, where an electromotive force was applied (Addison and Sharp, 1962b). Accordingly, crocidolite has its greatest electrical conductivity value along the c fiber axis.

Addison and White (1968) showed that Fe<sup>2+</sup> can remain unoxidized at high temperature even in presence of hydroxyl, if no route is available for the migration of electrons toward the surface. According to their model, these routes can be blocked by ions such as Mg<sup>2+</sup>, which cannot uptake electrons. The probability of such blocking is less in a layered than in a chain silicate, since in the first case a larger number of different trajectories are possible for electrons. For this reason in amphiboles this effect assumes an important role in HT treatments.

A crocidolite sample from South Africa with a small amount of Mg (approximate composition:  $\text{Na}_2\text{Fe}^{3+}_2(\text{Fe}^{2+}_{2.5}\text{Mg}_{0.5})\text{Si}_8\text{O}_{22}(\text{OH})_2$ ) was studied by Addison *et al.* (1962a), who found that in the temperature range 400 to 450°C, the oxidation terminated before converting all the starting  $\text{Fe}^{2+}$  content. In this early paper, the “dehydrogenation” was already recognized as the principal process, even though the yields of water obtained were always less than the theoretical expected yield, and even if the amount of oxidized ferrous iron was always in excess if compared to what permitted by the hydroxyl content. It was observed at 450°C that, for a series of crocidolites with different Mg/Fe ratio, the higher is the Mg content, the higher is the amount of unoxidized ferrous iron; furthermore, breaking the sample into short fibers before oxidation, allowed a larger amount of iron to be oxidized. Octahedral cations in amphiboles are arranged in a ribbon-like fashion parallel to the *c* (fibre) axis, and any electron transfer is supposed to proceed along the ribbon. If two adjacent *M*(1)-sites, represented by purple octahedra (Figure 2.2), are occupied by Mg, the migration of an electron along this ribbon is stopped. If two such blocks occur within one fiber, those ferrous ions which are trapped between the two blocks cannot be oxidized by a combination of reactions 2.1 and 2.2. The residual ferrous iron which is prevented by magnesium for being oxidized, will become available for oxidation only at higher temperatures where structural transformations can occur.

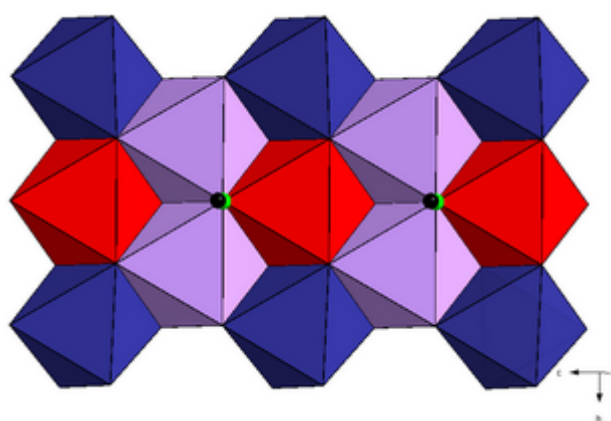


**Figure 2.2.** Diagrammatic representation of the octahedral strip, within the structure of an amphibole, parallel to the *c* axis. The *M*(1)-sites are represented with purple octahedra. The OH-groups at the O(3) positions are shown in black and green.

It was also observed that breaking the sample into short fibers would greatly reduce the likelihood of “Mg blocks” at  $M(1)$ -sites to occur within the same fiber, making the oxidation/dehydroxylation process possible at lower temperatures.

Addison and Sharp (1968) reported how the oxidation of amosite with approximate composition  $\text{Fe}^{2+}_{5.5}\text{Mg}_{1.5}\text{Si}_8\text{O}_{22}(\text{OH})_2$  proceeded by both “oxygenation” and “dehydrogenation”, and that there were evidences that the latter process was completed by 550°C. They also showed that the composition of the oxidized material still contained both  $\text{Fe}^{2+}$  and hydroxyl, possibly due to the presence of magnesium blocking the process. The sample from Bolivia studied in Addison and White (1968) had an intermediate content in Mg, with the composition:  $(\text{Na}_{1.75}\text{K}_{0.10}\text{Ca}_{0.22})(\text{Mg}_{2.50}\text{Fe}^{2+}_{0.55}\text{Fe}^{3+}_{1.92})(\text{Si}_{7.65}\text{Al}_{0.02})\text{O}_{22}(\text{O}_{0.41}\text{OH}_{1.59})$ . They showed that in the temperature range from 420°C to 550°C, the oxidation took place mainly by “dehydrogenation”, and stopped when a significant amount of  $\text{Fe}^{2+}$ , and, according to spectroscopic evidence, a significant amount of hydroxyl ions remained. These experimental results show how, for the Bolivian crocidolite, the suggested process of magnesium blocking could possibly explain, better than for the South African sample, the termination of reaction in these conditions.

It was observed that, for the Bolivian but not for the South African crocidolite, the point at which the oxidation protracts increases with temperature. An explanation to this phenomenon was thought to be the increased mobility of the magnesium ions with temperature, which gradually removes the obstacles to electron migration. In the 400 - 500°C range, the end of the reaction for the low-Mg South African crocidolite occurs when “oxygenation” is the only possible process, since all the hydroxyl groups have been eliminated. By contrast, for the Mg-rich Bolivian sample, both “dehydrogenation” and “oxygenation” are still supposed to be possible.

Ernst and Wai (1970) could detect an apparent cation migration in a Mg-riebeckite heated in air for 1 h at 705°C by means of Mössbauer spectroscopy. Ungaretti (1980) observed the absence of any significant H peak in the difference-Fourier map of a metamorphic riebeckite heated in air at 650°C for 4 days, and concluded that “dehydrogenation” was a consequence of heating. He also observed a shortening of the  $M(1)$ -O(3) and  $M(3)$ -O(3) bond lengths in the structure of the heat-treated sample, and explained it as a compensation for the loss of bond strength at O(3) resulting from “dehydrogenation”.

This author could also observe in the same sample, a considerable change in the number of electrons per octahedral site after heating, compatible with a migration of Na atoms from  $M(4)$  to the previously vacant A-site induced by oxidation/"dehydrogenation". In Hawthorne (1983), the IR spectra collected in Ernst and Wai (1970) on Mg-riebeckite and glaucofane are considered in agreement with the conclusions of Ungaretti (1980). In particular Hawthorne (1983) noted that the IR-band broadening is due to cation disordering, and explained the increased intensity of a small band at  $3685\text{ cm}^{-1}$  with an increase in the Na content at the A-site at the expenses of  $M(4)$ .

Phillips *et al.* (1988) studied the structural changes associated with oxidation/"dehydrogenation" using bond length data from six crystal-structure refinements done on heat-treated samples. The results show a decrease in bond strength at O(3), which is in part compensated by shortening of  $M\text{-O}(3)$  bond lengths. At least part of the loss in bond strength is balanced with interaction between O(3) and the A-site. In particular, in riebeckite a migration of Na from  $M(4)$  towards the previously vacant A-site was observed.

## 2.4. The reduction of crocidolite

The effect of heating crocidolite in hydrogen at different temperatures was described in Addison and Sharp (1962a). The samples used were from Koegas-Westerberg (South Africa). During the reduction in hydrogen, a liquid nitrogen cold trap system was used to remove the water formed; and the water yield was determined. The weight change was determined at the end of the experiment, and the final material was analyzed to determine its ferrous vs. ferric content. In some cases X-ray powder diffraction and infrared analysis were performed. The reduction of crocidolite was followed under various experimental conditions: outgassed and reduced at 450°C; outgassed and reduced at 615°C; outgassed at 615°C and reduced at 450°C; and outgassed, oxidized, and reduced at 450°C. The outgassing consisted by heating the samples *in vacuo*.

The infrared spectrum of the fresh crocidolite showed absorptions at 3623 and 3640 cm<sup>-1</sup>, which were assigned to the hydroxyl group. The same features were still recognizable in the sample outgassed and reduced at 450°C, even though some loss in band intensity was evident. A decrease in intensity of the hydroxyl bands was also observed in the sample outgassed at 615 and reduced at 450°C. The OH-bands disappeared in the sample reduced at 615°C. The X-ray powder patterns of the samples treated up to 450°C turned out to be similar to the initial material, while those collected on samples reduced at 615°C showed them to be amorphous.

The water formed on the reduction of fresh crocidolite both at 450 and 615°C turned out to be one mole H<sub>2</sub>O per mole of hydrogen taken up. After reduction, the ferrous and ferric contents were determined and compared with the analysis of fresh material. The increase in ferrous content, the decrease in ferric content, and the volume of hydrogen taken up, were determined for each experimental condition. Considering that water is always formed during reduction, the authors proposed the following reactions:



It is important to point out that all of these reactions require at least local disruption of the structure.

The experimental results at 450°C are in agreement with Equation 2.7, while those at 615°C are compatible with Equation 2.5 as a main process coupled with Equation 2.6 or 2.7 as side reactions. The formation of  $\text{Fe}^0$ , however, was not observed, thus invalidating Equations 2.7 and 2.6.

Concerning the possible mechanisms of reaction, Addison and Sharp (1962a) suggested that the transport of molecules through the crystal structure is unlikely thus the migration of electrons and protons was preferred to explain the oxidation process. In order to determine the mechanisms of reaction and the likely centers of instability and structural breakdown, the electrostatic potentials for various oxygens in crocidolite were calculated under various conditions (Table 2.1), following Pauling (1961). In this calculation it was assumed that the  $M(4)$ -sites are occupied by sodium, the  $M(2)$ -sites by ferric ions, and the  $M(1)$  and  $M(3)$ -sites by divalent magnesium and ferrous ions.

	Fresh	Oxidized	Gain of $\text{H}^+$ and $\text{e}^-$	Outgassed at 615°C and dehydroxylated	Gain of $\text{H}^+$ and $\text{e}^-$ by dehydroxylated sample
<b>O(1)</b>	2.17	2.38	2.00	2.30	2.13
<b>O(2)</b>	1.96	2.06	1.79	2.03	1.86
<b>O(3)</b>	2.00*	1.32	2.00*	1.20	2.20*
<b>O(4)</b>	1.63	1.63	2.46*	1.63	1.46

**Table 2.1.** Calculated positive electrostatic potentials for various oxygen atoms in crocidolite under different conditions (Addison and Sharp, 1962a). Atoms marked \* are bonded to hydrogen; the conditions described in the third and the last columns are suggested as transient states.



In Figures from 2.3a to f, the oxygen atoms in the crocidolite structure are represented along with the respective coordinated cations.

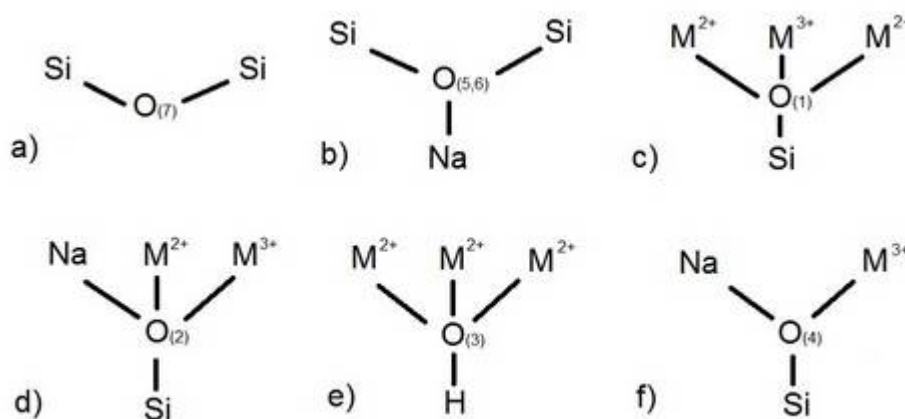


**Figure 2.3.** Diagrammatic representation of the ions bonded to the various oxygen atoms in crocidolite.

The term electrostatic potential is a very old-fashioned term, Brown (1981, 1992) developed a much more convenient approach to chemical bonding in inorganic structures based on the empirical bond-valence curves of Brown & Shannon (1973). Bond-valence is a measure of the strength of a chemical bond and can be calculated based on the empirical bond-valence curves of Brown & Shannon (1973) and Brown & Aftermatt (1985) if the bond lengths are known. The valence-sum rule states that the sum of the bond-valences incident at each atom is equal to the magnitude of the formal valence of that atom. Hawthorne (1983) carried out a bond-valence analysis on a ferro-glaucophane (ideal composition:  $\square\text{Na}_2\text{Fe}^{2+}_3\text{Al}_2\text{Si}_8\text{O}_{22}(\text{OH})_2$ ) sample where the results are compared with the bond strength sums calculated from the formal Pauling scheme for each different oxygen. The results are summarized in Table 2.2.

	<i>M</i> (1)	<i>M</i> (2)	<i>M</i> (3)	<i>M</i> (4)	<i>T</i> (1)	<i>T</i> (2)	$\Sigma$	$\Sigma^p$
<b>O(1)</b>	0.367	0.396	0.339 <sup>x2</sup> <sub>↓</sub>		0.992		2.094	2.167
<b>O(2)</b>	0.361	0.476		0.193		0.977	1.947	1.958
<b>O(3)</b>	0.341 <sup>x2</sup> <sub>→</sub>		0.382				1.064	1.000
<b>O(4)</b>		0.605		0.220		1.072	1.897	1.625
<b>O(5)</b>				0.094	1.019	0.927	2.040	2.125
<b>O(6)</b>				0.175	0.997	0.917	2.089	2.125
<b>O(7)</b>					1.013 <sup>x2</sup> <sub>→</sub>		2.026	2.000
$\Sigma$	2.138	2.954	2.120	1.364	4.021	3.893		

**Table 2.2.** Empirical bond-valence tables for ferro-glaucofane from Hawthorne (1983).

From Table 2.2 it can be seen how for ferro-glaucofane (Hawthorne, 1983), and in general in all the amphiboles (Figure 2.3), O(4) is the most underbonded oxygen.

*Crocidolite outgassed and reduced at 450°C.*

The sample maintains all its hydroxyl groups. Since there is a deficiency of bond-valence at O(4) (Table 2.1), it was suggested that the first step of the reduction is the gain of a proton by O(4). Even in the case that the neighboring Fe<sup>2+</sup> at *M*(2) oxidizes to Fe<sup>3+</sup>, there would be an excess in positive charge at O(4). Hence it was speculated that this point of the structure could be a nucleus for a structural breakdown. Afterwards, the subtraction of all the valence electrons from *M*(2), which becomes Fe<sup>0</sup>, and the loss of a structural oxygen to produce water, are supposed to occur, as described in Equation 2.7. If the maximum observed uptake of hydrogen, corresponding to the reduction of one third of Fe<sup>3+</sup> to the zero-valent state, was achieved, much of the structure would be maintained, in agreement with infrared and X-ray results. Iron atoms would remain dispersed throughout the structure, and this explains why they are not detected with X-rays. Here we stress again that Fe<sup>0</sup> was never detected in heat-treated samples (e.g. Ernst and Wai, 1970), and hence, Equation 2.7 may not be valid.

*Crocidolite outgassed and reduced at 615°C.*

Nearly all of the hydrogen is lost by the structure, but the structure does not collapse. If all of the protons are assumed to be removed from O(3), the calculated electrostatic potentials (Table 2.1, fourth column) show a deficiency of bond-valence at O(3) and O(4), which are both three-coordinated and therefore possible sites for the uptake of a proton. The mechanism suggested for reduction is: addition of a proton to O(3); simultaneous reduction of an  $\text{Fe}^{3+}$  to  $\text{Fe}^{2+}$  by an electron; interaction of another proton with O(4) and reduction from  $\text{Fe}^{2+}$  to  $\text{Fe}^0$  in the adjacent  $M(2)$ -site. Since at this temperature the structure cannot tolerate OH-groups, the structure breaks down, as shown by X-ray and infrared experiments.

*Crocidolite outgassed at 615°C and reduced at 450°C.*

The mechanism is similar to what described above, with the difference that the elimination of OH re-formed at O(3) cannot happen at 450°C during reduction. This leads to a less dramatic structural breakdown then in the case discussed above, and the water yield is less than in the other two cases described.

*Crocidolite outgassed, oxidized and reduced at 450°C.*

Oxidation removes the hydrogen from O(3) without any loss of oxygen, in addition it was observed that 63% of the metal ions in  $M(1)$  and  $M(3)$  become  $\text{Fe}^{3+}$ . In Table 2.1, second column, it is shown how also in this conditions O(3) suffers a deficiency of bond-valence. As it was said, at 450°C a proton can add either to O(3) or O(4). If the hydrogen combines to O(3), an hydroxyl group is generated in its normal position, and an electron changes an  $\text{Fe}^{2+}$  into  $\text{Fe}^{3+}$  in a neighboring  $M$ -site, giving the same situation as in unoxidized material.

If the proton can add to O(4), the reaction described in Equation 2.7 will occur and some water is produced in agreement with experimental results. Here we mention once again that the validity of Equation 2.7 has never been confirmed because of the lack of  $\text{Fe}^0$  formed during the heat-treatment.

## **2.5. The kinetics of oxidation of crocidolite**

Ernst and Wai (1970) showed that in alkali-amphiboles heated in air at 705°C, extensive  $\text{Fe}^{2+}$  oxidation occurs by “dehydrogenation” within 1 or 2 hours. Ungaretti (1980) found that a change in cell parameters of several Fe-bearing amphiboles heated in air at 500°C also indicate that extensive “dehydrogenation” occurs in less than 2 h.

The oxidation rate of crocidolite as a function of  $T$  and pressure was investigated by Addison *et al.* (1962b). The samples used were from Koegas-Westerberg (South Africa), occurring as bundles of fibrous masses, 3 - 40 mm thick. These masses were split into single fibers for the experiments. Each sample, was initially outgassed overnight at  $10^{-6}$  mmHg, then the oxidation was studied for variable values of pressure (up to 450 mmHg with a carbon dioxide cold trap, or to 150 mmHg with a liquid nitrogen one) and for constant temperature values (between 350 and 480°C). The experiments were carried out by allowing the oxygen pressure to decrease as reaction proceeded. The rate of the process turned out to slightly decrease with decreasing pressure. In all experiments the reaction stopped completely even though a significant amount of oxygen pressure was still present in the gas phase.

To study the effect of temperature, the previously outgassed samples were kept at constant temperature (starting from 350°C), and the oxidation was followed for the least time necessary to determine the rate, then further oxidations were performed at successively higher temperatures. Plotting the logarithm of the rate (amount of  $\text{O}_2$  absorbed by a gram of crocidolite in one hour) versus the reciprocal temperature, the activation energy of the process could be calculated from the slope of the regression line obtained. The activation energy for the reaction turned out to be 21 Kcal/mol, when a liquid nitrogen cold trap system was used to remove the freshly formed water from the surface of the crocidolite; the activation energy was 33 Kcal/mol, when a carbon dioxide cold trap was used. It was also observed that the water formed during the reaction was very tightly held on the surface, enough to inhibit further oxidation even at high temperatures.

Since the carbon dioxide trap is considerably less efficient in removing water, the difference between the two activation energies was assigned to the energy necessary for oxygen to penetrate through the monolayer of water. Addison *et al.* (1962b) concluded that the activation energy of the oxidation is 21 Kcal/mol when the active sites of the surface are free from the layer of water. Hence this value is suggested to be the net energy required by the electrons and possibly protons to migrate through the crystal structure, in order to feed the reaction on the surface.

## 2.6. Summary

Several previous studies examined the deprotonation/oxidation of iron-bearing amphiboles at HT. For  $T < 550^{\circ}\text{C}$ , the suggested mechanism is a combination between Equations 2.2 and 2.3, named “dehydrogenation” and “oxygenation”, respectively. The first one consists in a simultaneous oxidation of  $\text{Fe}^{2+}$  and hydroxyl loss, with no change in the number of oxygen or metal atoms (Addison and Sharp, 1962b). The latter represents an alternative oxidation of  $\text{Fe}^{2+}$  when no hydroxyl ions are available, and involves the formation of a superficial iron-oxide layer. The formation of an iron oxide layer, however, has never been proved by analyses. “Dehydrogenation” takes place on the crystal surface where  $\text{Fe}^{2+}$ ,  $\text{OH}^-$  and gaseous oxygen are available. The development of this process is possible only if the ions involved during the process ( $\text{Fe}^{2+}$  and  $\text{OH}^-$ ) are regenerated on the surface by intra-crystalline migration. The migration of electrons and possibly protons is supposed to require less energy than the ionic transport, hence the electron transfer from  $\text{Fe}^{2+}$  to an adjacent  $\text{Fe}^{3+}$  is thought to ensure the presence of the reactant  $\text{Fe}^{2+}$  at the surface, while  $\text{OH}^-$  could be generated at the surface by proton hopping from one oxygen to another (Addison and Sharp, 1962a). Migration of electrons probably occurs in amphiboles exclusively along the double chain direction (c-axis). The electron transfer is hindered by ions that cannot accept extra electrons such as  $\text{Mg}^{2+}$  (Addison *et al.*, 1962a).

Even though the electron hopping process is endorsed by several authors (e.g. Schmidbauer *et al.*, 2000), the mechanisms of the transport of hydrogen are not yet understood. Calculations of the electrostatic potentials on a crocidolite (Addison and Sharp, 1962a) and of bond-valence on a ferro-glaucophane (Hawthorne, 1983) at the various oxygen atoms, showed that there is only one structural site, O(4), potentially able to accept a transient H due to its underbonding (Addison and Sharp, 1962a).

Structural refinements on an heat-treated metamorphic riebeckite showed a migration of Na from M(4)-sites towards the previously empty A-site, associated with an evident loss in hydrogen and an  $\text{Fe}^{2+}$  oxidation within the octahedral sites (Ungaretti, 1980). In this previous study, it was proposed that because of oxidation of ferrous iron, an excess of positive charge was determined on some of the oxygens at M(1) and M(3).

The cationic migration towards the previously empty *A*-site, along with the noticeable variations of some bond distances within octahedra, were hence explained as a processes dictated by bond-valence requirements.

The oxidation rate of crocidolite as a function of *T* and pressure was investigated by Addison *et al.* (1962b). The rate of the process turned out to slightly decrease with decreasing of pressure. Ernst and Wai (1970) showed that in alkali-amphiboles heated in air at 705°C, extensive Fe<sup>2+</sup> oxidation occurs by “dehydrogenation” within 1 or 2 hours. Ungaretti (1980) found that a change in cell parameters of several Fe-bearing amphiboles heated in air at 500°C also indicates that extensive “dehydrogenation” occurs in less than 2 h. A thorough characterization of the Fe-oxidation/deprotonation of Fe-rich amphiboles from a kinetic point of view is still necessary, and would yield important information for the comprehension of the mechanisms involved in the process.



## Chapter 3 Single crystal HT-FTIR spectroscopy of synthetic potassic-ferro-richterite

---

**Note: this chapter is the present version of a paper to be submitted soon for publication.**

The physical and crystal-chemical properties of materials are strongly dependent from temperature, and for this reason several disciplines are interested in their study at high- $T$ ; notable cases are mineralogy, ceramic science, chemical and electrical and mechanical engineering, metallurgy and physics. Most thermal processes do involve chemical transformations and phase-transitions that need to be characterized by using combinations of *in situ* analytical techniques, such as HT-diffraction (both on single crystals or powders), TG/DTA, and HT spectroscopies. Relevant to this point is the fact that most mineral reactions, like dehydration, involve the loss and subsequent migration/diffusion of oxygen/hydrogen molecular arrangements; this process must be associated with simultaneous oxidation of multi-valence elements, such as Fe or Mn, with significant consequences on the physical properties of minerals and thus of the rock where they occur. Enhanced electrical conductivity in Earth's crust and in the upper mantle has been related, for example, to such processes occurring in subducted amphibolites (e.g. Karato and Wang, 2012, Wang *et al.*, 2012, 2013), implying that knowledge of the temperature effects on the physical properties of minerals has paramount interest in geophysical modeling. Despite this, the deprotonation reactions in iron-bearing hydrous minerals, and their role on both electrical conductivity and magnetic properties are still poorly known.

Early HT studies on iron-rich amphiboles have been done during the 60-70's (Addison *et al.*, 1962a, 1962b; Addison and Sharp, 1962a, 1962b, 1968; Addison and White, 1968; Ernst and Wai, 1970) because of the emerging technological relevance

of these minerals for a variety of applications (fire-proof textiles, thermo-acoustic insulators, construction materials, water pipes, electrical spare parts etc.). In the last few years, increasing efforts have been devoted to the study of different amphibole species at non-ambient conditions (see review by Welch *et al.*, 2007) and several features controlling the crystal-chemical and crystal-structural adjustments accompanying HT treatments are now going to be clarified (Welch *et al.*, 2011; Zema *et al.*, 2012; Oberti *et al.*, 2012a, 2012b, 2016). However, notable issues still need to be understood, including the mechanisms and kinetics of proton diffusion throughout the mineral matrix, and the role of multiple-valence elements, notably Fe, in this process.

The present study represents a further step of an ongoing effort on the high-*T* study of Fe-bearing amphiboles, done by using a fully multidisciplinary approach, including microchemistry (EMP and SEM), X-ray diffraction, and spectroscopic methods (FTIR, Mossbauer, XAS). In this paper we describe in particular the FTIR results obtained at HT on the same synthetic amphibole studied by HT-SC-XRD (single crystal X-ray diffraction) by Oberti *et al.* (2016). The aim of this work is twofold: (1) integrate the single crystal HT X-ray results for a better description of the deprotonation process, and (2) study the temperature dependence of the OH-stretching bands of a relatively simple and well-constrained Fe-bearing amphibole, by combining *in situ* and quenched (*ex-situ*) measurements. As it will be discussed below, this issue is in fact a major problem in HT-FTIR spectroscopy, and needs to be properly calibrated if the spectroscopic data are to be used for quantitative studies (e.g. Zhang *et al.*, 2007; Radica *et al.*, 2015).

### 3.1. Studied sample and experimental methods

The sample studied in this paper (labeled Ri1) has been synthesized by Redhammer and Roth (2002) and recently characterized in details by Oberti *et al.* (2016); the reader is referred to the paper of Redhammer and Roth (2002) for full description of the synthesis procedures. According to Oberti *et al.* (2016) the crystal-chemical formula of amphibole Ri1, obtained by combining SC-XR structure refinement and FTIR spectroscopy is:  ${}^A(K_{0.90}Na_{0.07}){}^B(Ca_{0.54}Na_{1.46}){}^C(Fe^{2+}_{4.22}Fe^{3+}_{0.78}){}^T Si_8O_{22}{}^W(OH_{1.70}O^{2-}_{0.30})$ . Although still in the compositional field of richterite, this sample falls close to the richterite/arfvedsonite boundary (see Hawthorne and Oberti, 2007 and Hawthorne *et al.*, 2012 for systematic issues on amphibole nomenclature).

Non-polarized *in situ* and quench single crystal HT-FTIR spectra were collected at INFN (Frascati) using a Linkam 1400XY heating stage, fitted on a Bruker Hyperion 3000 FTIR microscope equipped with a 15X Schwarzschild objective and a MCT N-cooled detector. The microscope was attached to a Vertex optical bench equipped with a KBr beamsplitter and a globar IR source; the beam was reduced to 50  $\mu m$  and 256 spectra were co-added for both mineral and background. The sample was prepared as a doubly-polished, 100  $\mu m$ -thick section, and broken into two fragments, used for two different experiments: during the first experiment, the FTIR spectra were collected *in situ* up to 600°C, with a  $T$  step of 10°C; the heating rate was 10°/min and the spectrum was collected immediately after reaching the target  $T$ . In the second experiment, the same heating rate was employed, but in addition to *in situ* data, a second set of spectra at 50°C intervals was collected on samples quenched at room- $T$  (RT) after annealing the crystal at the target temperature. After the RT collection the sample was re-heated to the next temperature step and so on.

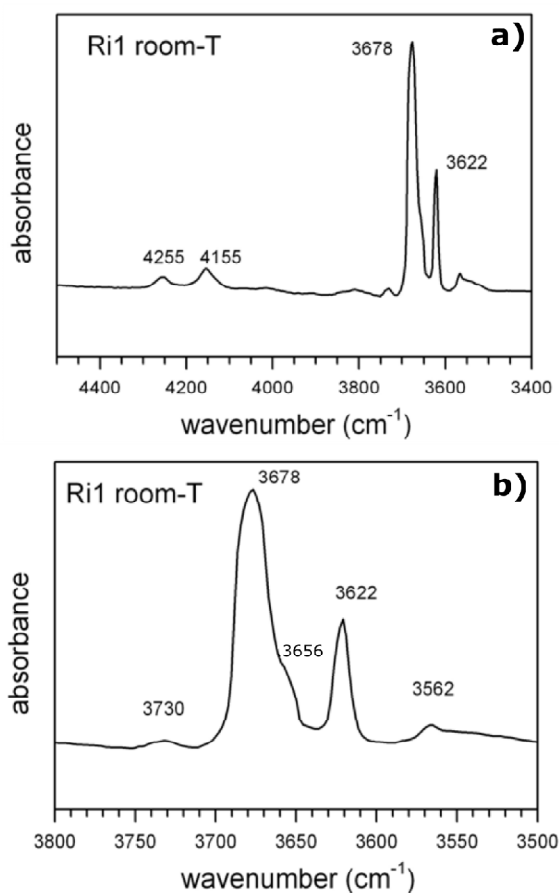
### 3.2. Single crystal HT-FTIR spectroscopy

In this section, we compare the FTIR data collected *in operando* at high- $T$  with those collected at room  $T$  after quenching the sample at each temperature value examined. In our knowledge, this comparison has never been done for amphiboles and is of methodological interest to critically evaluate the results of FTIR analysis.

The spectrum of the unheated crystal (Fig. 3.1) shows a main band at 3678  $\text{cm}^{-1}$  and a minor band at 3622  $\text{cm}^{-1}$ ; a well evident shoulder is also resolved on the lower frequency side of the main band, at 3656  $\text{cm}^{-1}$  (Fig. 3.1b). According to the systematic work on the FTIR spectroscopy of richterites with different cation occupancies at the octahedral sites (e.g. Robert *et al.*, 1989; Della Ventura, 1992; Della Ventura *et al.*, 1996, 1997, 1998, 2005, 2015; Iezzi *et al.*, 2004, 2005), and considering the controlled chemistry of the synthetic system, the main band at 3678  $\text{cm}^{-1}$  is assigned to the  $^{M(1)}\text{Fe}^{2+M(1)}\text{Fe}^{2+M(3)}\text{Fe}^{2+}\text{-OH}$  local environment, with the O-H dipole pointing toward an occupied A-site, while the lower-frequency band can be assigned to the same local configuration but with the O-H group pointing toward an empty A-site. On the basis of the new structure refinement and the behavior observed during the heat-treatment, the 3656  $\text{cm}^{-1}$  band can be assigned (Oberti *et al.*, 2016) to the presence of a minor, but significant, oxo-component in the structure. Two relatively broad but well-defined peaks are observed in the NIR region, at 4255 and 4155  $\text{cm}^{-1}$ , respectively (Fig. 3.1a). This region of the spectrum for amphiboles is rather poorly known; according to literature data (e.g. Clark *et al.*, 1990; Mustard, 1992 and Laukamp 2012) these bands can be assigned to the combination of stretching and bending vibrations of the O-H dipole ( $\nu_3 + \delta_{\text{OH}}$ ).

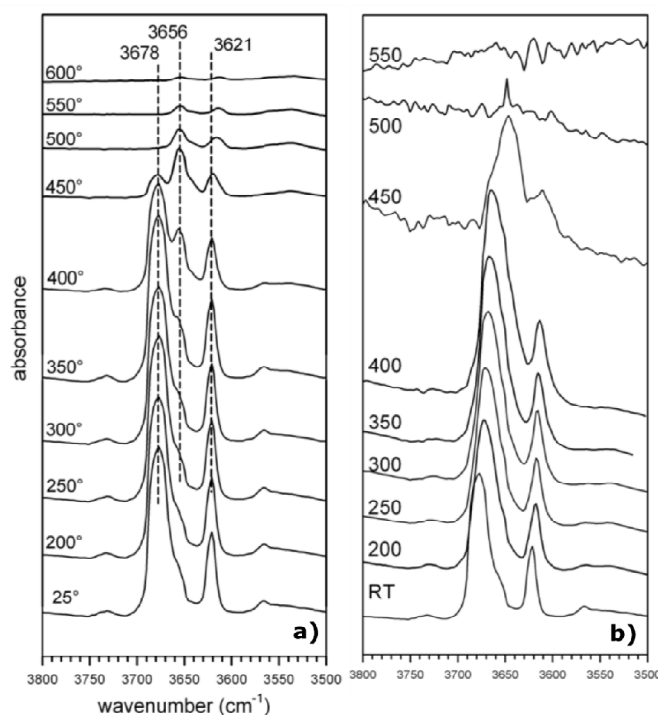
Finally, minor peaks are present at 3730 and 3562  $\text{cm}^{-1}$ , respectively. The frequency of the former corresponds to that of Mg-richterite (e.g. Robert *et al.*, 1989; Della Ventura, 1992; Gottschalk and Andrut, 1998), however, due to the absence of Mg in the synthetic system a possible assignment to an overtone/combination mode of the silicatic structure is more likely; note that such absorptions are invisible in powder FTIR data, but may show up in single crystal data. The minor peak at 3562  $\text{cm}^{-1}$ , because of its frequency cannot be assigned to any of the cationic permutations feasible considering the composition of the examined amphibole, but possibly to some mica-like local configurations (biopyribole defects) or again to

overtone/combination modes of the silicatic structure. In any case, because of their low intensity, these bands can be neglected for the discussion below.



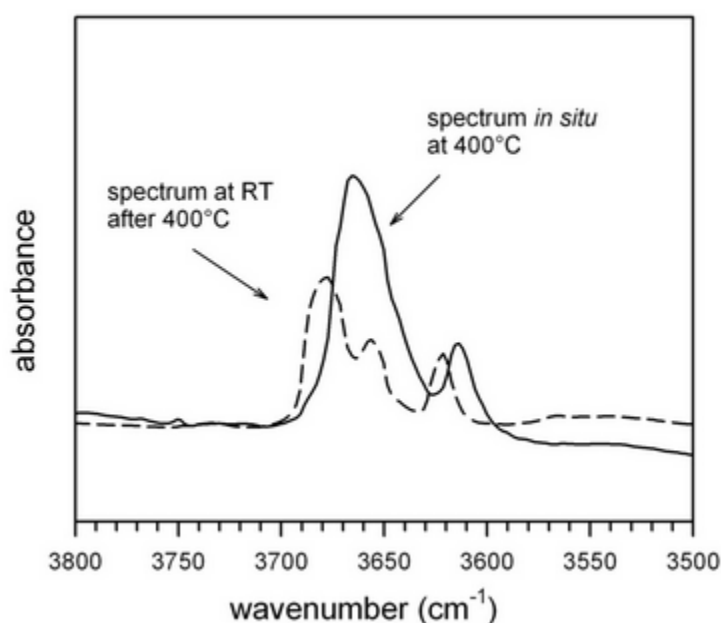
**Figure 3.1.** Room-*T* single crystal unpolarized spectra, collected on randomly oriented 100  $\mu\text{m}$  thick-section; (a) NIR (near infrared red) range; (b) enlargement of the principal OH-stretching region.

Single crystal HT-FTIR spectra collected at room- $T$  on quenched samples are plotted, with the same absorbance scale, in Figure 3.2a. Inspection of the spectra shows clearly that from 25 to 350°C there is very limited variation in band intensity and shape. At 400°C a peak at 3656  $\text{cm}^{-1}$  clearly shows up, however the 3678  $\text{cm}^{-1}$  band still is the major feature in the pattern. The 450°C pattern is completely different from the previous: the main component at 3678  $\text{cm}^{-1}$  has lost most of its intensity, while a new band at 3556  $\text{cm}^{-1}$  is now the most intense. For  $T \geq 500^\circ$  the absorbance decreases drastically; at 600°C the sample still retains a minor amount of OH. The spectra collected *in operando* during the heating ramp (Fig. 3.2b) are different from those collected on quenched crystals: the main band at 3678  $\text{cm}^{-1}$  broadens and shifts to lower frequency and increases in intensity up to 400°C; at 450°C it is replaced by a new broad and multi-component band centered around 3656  $\text{cm}^{-1}$ . For higher temperature the bands disappear abruptly and the signal is extremely noisy. At  $T \geq 550^\circ\text{C}$  no peaks can be resolved from the background.



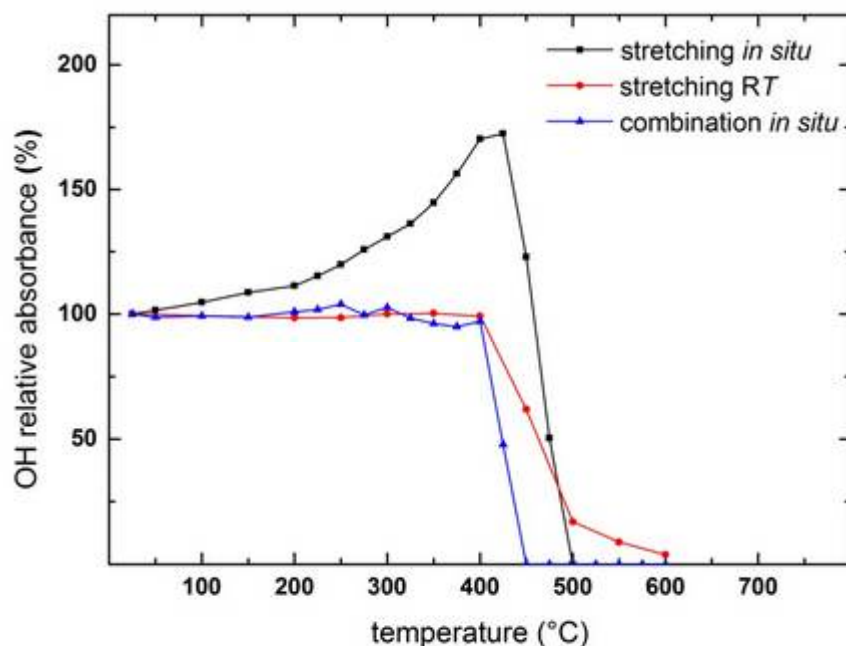
**Figure 3.2.** HT-FTIR spectra collected (a) after quenching the sample annealed at the target  $T$ , and (b) *in situ* during the heating ramp. Spectra plotted with the same absorbance scale.

Figure 3.3 compares, as an example, the O-H stretching band of the studied sample measured *in situ* at 400°C and the same band measured on the quenched sample after annealing at 400°C. It is evident that, because of the combined effect of a general broadening and a red shift of all the absorption components, the resolution between the main bands at 3678 and 3656 cm<sup>-1</sup> is lost in the spectrum collected *in situ*; in addition the overall intensity (area) of the band is significantly modified. It is worth noting that the downward shift of the 3678 cm<sup>-1</sup> component, assigned to the O-H dipole interacting with the alkali cation at the A-site, is almost double than the shift of the band at 3622 cm<sup>-1</sup>, assigned to the O-H dipole pointing toward an empty A-site ( $\Delta_\nu = 20$  cm<sup>-1</sup> vs 10 cm<sup>-1</sup>). This evidence confirms that the increase in the atomic disorder at high  $T$  increases the repulsive coulombic interactions between the O-H bond of the hydroxyl dipole and the A-site cation. An increase in positional disorder of the A-cations at high  $T$  is in fact observed in SC-XRD data (Oberti *et al.*, 2016), together with an ordering of the electron density at the  $A(m)$  position, which is displaced from the center of the cavity (to which the OH dipole points).



**Figure 3.3.** Comparison of the FTIR spectra collected *in situ* at 400°C and after quenching the sample annealed at the same  $T$ .

Figure 3.4 compares the evolution of the relative integrated intensity of the absorption in the  $3710\text{--}3600\text{ cm}^{-1}$  range measured *in operando* during the thermal treatment and after quenching the crystal. The *in situ* data show a significant increase of the intensity which almost doubles in the  $400\text{--}425^\circ\text{C}$  range, a results which is obviously unfeasible. In contrast, the intensity data collected on the quenched sample indicate a constant OH content up to  $400^\circ\text{C}$ , followed by an abrupt loss of the proton in the  $400\text{--}500^\circ\text{C}$   $T$  range. At  $500^\circ\text{C}$ , low amounts (10/15%) of OH are still present in the amphibole; the sample is finally completely deprotonated for  $T > 600^\circ\text{C}$ . Figure 3.4 displays also the data measured *in situ* for the combination modes at  $4255$  and  $4155\text{ cm}^{-1}$ ; it is evident that, although a certain difficulty to integrate the evolution of these weak bands (Fig. 3.1a) the absorbance of these modes follows a trend different from that of the principal stretching bands: it is constant till  $400^\circ\text{C}$  than decreases abruptly.



**Figure 3.4.** Comparison of the relative OH-stretching absorbance measured on the *in situ* (black), quenched samples (red) and *in situ* for the combination bands (blue), as a function of increasing  $T$ .



### 3.3. Discussion

#### *The absorptivity of the OH-bond of potassic-ferro-richterite as a function of $T$*

HT-FTIR studies done during the last years have shown that absorption bands typically broaden and shift with increasing  $T$ . This effect, which has been observed in many different minerals (e.g. Yamagishi *et al.*, 1997; Tokiway and Nakashima, 2010a,b; Zhang *et al.*, 2007, 2010) and glasses (Keppler and Bagdassarov, 1993) has been examined in detail by Zhang *et al.* (2007), who particularly focused on possible variations of absorption coefficients with  $T$ , an issue which has significant consequences for quantitative studies based on the Beer-Lambert relationship. An additional source of complexity in this issue arises from the observation that the dependence of the absorbance on  $T$  can be extremely different for the different vibrational modes in the same sample (Zhang *et al.*, 2007; Radica *et al.*, 2015). Simplifying, the molar absorptivity ( $\varepsilon$ ) in the Beer-Lambert relationship is  $\varepsilon = A/d \cdot C$ , where  $A$  is the measured absorbance (either linear or integrated),  $d$  is the sample thickness and  $C$  is the concentration of the target molecule. Thus,  $\varepsilon$  is the coefficient relating the intensity measured experimentally and the amount of the molecule (or molecular group) absorbing the incoming radiation. In quantitative studies,  $\varepsilon$  must be either calibrated for any matrix or evaluated on the basis of empirical relationships (e.g., Paterson, 1982; Libowitzky and Rossman, 1997). In HT studies, it is generally assumed that the  $\varepsilon$  coefficient is constant over the temperature range examined, although there is increasing evidence (Yamagishi *et al.*, 1997; Whitters *et al.*, 1999; Okumura and Nakashima, 2005; Zhang *et al.*, 2007, 2010; Tokiway and Nakashima, 2010a; Radica *et al.*, 2015) that this is not the case.

During this work, we obtained two different trends for the intensity of the principal OH-band when collecting spectra *in operando* or on quenched samples (Fig. 3.4). The trend obtained on quenched samples indicates that up to 400°C the OH concentration ( $C$ ) is constant; the sample thickness also can be considered constant because the expansion coefficients reported by Oberti *et al.* (2016) show a negligible variation over this  $T$  range. Therefore, in the Beer-Lambert relationship given above, the significant increase in absorption intensity observed during *in situ*

measurements (Fig. 3.4) can be solely attributed to a temperature-induced change of the integral molar absorptivity ( $\epsilon$ ). A similar conclusion was shown to be the case for muscovite (Tokiway and Nakashima, 2010a) and several other minerals (Zhang *et al.*, 2007).

The first consequence of this finding is that *in situ* FTIR data cannot be converted directly into quantitative information for the studied amphibole. The reason for the dependence of the molar absorptivity on temperature is not clear; for muscovite Tokiway and Nakashima (2010a) hypothesized a possible role of a variation in the O-H orientation, i.e. a tilting of OH dipoles with respect the  $c^*$  crystallographic direction (from  $75^\circ$  at room- $T$  to  $43^\circ$  at  $650^\circ\text{C}$ ) for increasing  $T$ , however we have no evidence of such a process in our amphiboles.

The intriguing point in Figure 3.4 is that the intensities measured *in operando* for the studied amphibole increase significantly in the range considered and finally almost double close to the onset of deprotonation (around  $400\text{--}425^\circ\text{C}$ ) whereas, in all previous HT-FTIR studies on different minerals, a decrease in the  $\text{H}_2\text{O}/\text{OH}$  intensity is systematically observed, for the fundamental modes, during heating (i.e. Zhang *et al.*, 2007; Tokiway and Nakashima, 2010a). Multiphonon (combination or overtone) bands, on the other side, have been reported to increase in some minerals, a notable case being provided by talc (Zhang *et al.*, 2007). It is also worth to note that a similar increase in intensity of the fundamental stretching band as a function of  $T$  seems to be typical for the  $\text{CO}_2$  absorption; this feature has been recently observed in cordierite (Radica *et al.*, 2015) and in different sodalite-group minerals (unpublished).

The reason for the anomalous intensity increase of Figure 3.4 is currently unknown. The main fundamental band at  $3678\text{ cm}^{-1}$  at room- $T$  shifts to  $3636\text{ cm}^{-1}$  at  $400^\circ\text{C}$  (Fig. 3.4) and this red shift is compatible with the fact that the O-H band in richterite is not involved in hydrogen bonds with the nearest-neighbor oxygen atoms (Hawthorne and Della Ventura, 2007). Therefore, the increase in molar absorption coefficient could be related somehow to an increase in the O-H bond strength. What is clear is that such a behavior is reproducible for Fe-amphiboles because a similar trend has been observed for riebeckite (Susta *et al.*, 2016) and for actinolite (unpublished). A second feature worth of note is that apparently this effect seems to be less pronounced for powders than for single crystals (Susta *et al.*, 2016; see Chapter 5).

*The behavior of potassic-ferro-richterite during heating*

Figure 3.5 compares the evolution of cell volume of potassic-ferro-richterite from Oberti *et al.* (2016) with the evolution of the OH-stretching absorbance (quenched data) obtained in this study. The X-ray diffraction data show (Fig. 3.5a) that in the  $R7 < T < 350^{\circ}\text{C}$  range the structure expands as a function of the thermal treatment; for increasing temperature there is a significant and fast contraction of the cell volume starting at  $350^{\circ}$  and completed within  $100^{\circ}\text{C}$ . On the basis of the refined structural parameters (electron densities, site-occupancies and octahedral bond lengths), Oberti *et al.* (2016) concluded that the observed contraction is due to the oxidation of  $^{M(1)}\text{Fe}^{2+}$  to  $^{M(1)}\text{Fe}^{3+}$ , correlated to a loss of H at the relevant O(3) sites, to produce an oxo-amphibole. For  $T > 450^{\circ}\text{C}$  up to  $800^{\circ}\text{C}$  the oxo-amphibole structure is still retained and keeps expanding with the same trend as the OH-amphibole. The FTIR data (Fig. 3.5b) add another piece of information to this picture, and directly show the loss of OH accompanying the transformation. A point that deserves a comment here is that the dehydration temperature provided by SC-FTIR ( $400/450^{\circ}\text{C}$ , Fig. 3.4) is  $\sim 100^{\circ}\text{C}$  higher than that reported by Oberti *et al.* (2016) for the same amphibole studied by SC-XRD. This  $T$  shift cannot be assigned to thermocouple malfunctions because both heating systems (our HT stage and the furnace used by Oberti and co-workers) were calibrated against the melting point of known substances. The different heating regime used for the two experiments ( $\sim 2$  hrs for FTIR vs.  $\sim 48$  hrs for XRD) cannot either be responsible for the  $T$  shift because refinement of XRD powder data collected *in situ* for the same potassium-ferro-richterite (unpublished), using a heating regime close to that used here for FTIR, gave the same results of Oberti *et al.* (2016), i.e. a deprotonation  $T$  close to  $350^{\circ}\text{C}$ . Unfortunately, we could not collect HT-FTIR powder data on the studied amphibole because of sample unavailability. A possible explanation to this conundrum is suggested by the results of Susta *et al.* (2016) for riebeckite (see also Chapter 5). Due to the availability of large amount of sample, these authors could compare the *in situ* HT-FTIR data on crystals vs. powders and observed that the dehydration  $T$  obtained on powders, under the same experimental conditions, is systematically  $100^{\circ}\text{C}$  lower than that obtained on single crystals. In other words, while X-ray diffraction provides the same results on both powders and single crystals, the infrared data obtained on single crystals (as in the

present work) are shifted 100°C to higher  $T$  with respect to those obtained on powders.

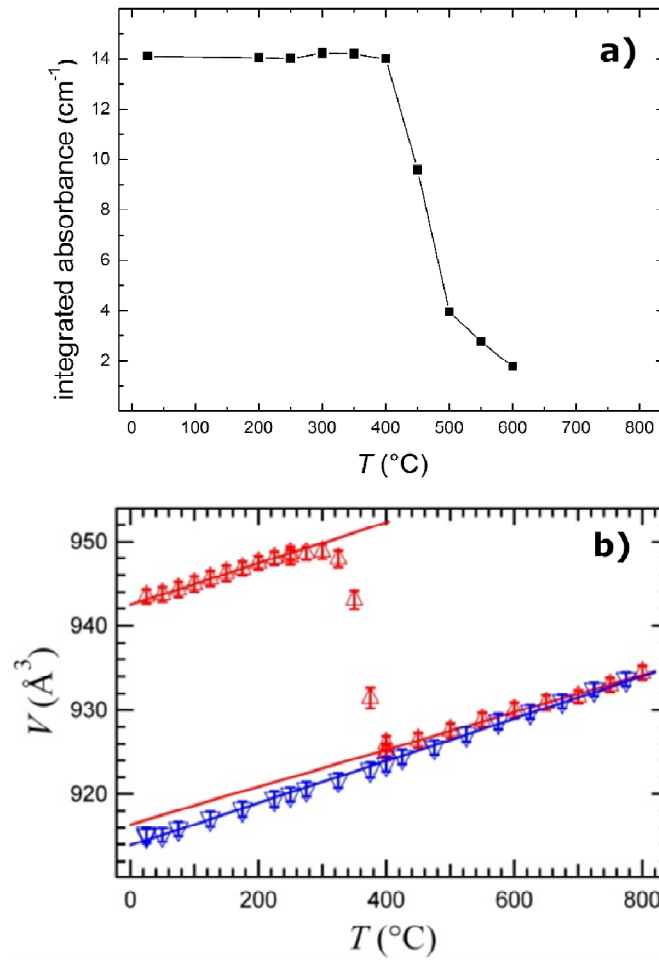


**Figure 3.5.** Evolution (a) of the OH-stretching absorbance (quenched data) obtained in this study, and (b) of the cell volume of potassic-ferro-richterite (from Oberti *et al.*, 2016).

*Local order in the deprotonation process of potassic-ferro-richterite*

The recent work of Oberti *et al.* (2016) done by HT-SC-XRD shows that, for increasing  $T$ , the structure of the studied amphibole expands linearly up to 300°C; for 300°C <  $T$  < 400°C there is an abrupt contraction of all cell edges, up to 400°C; for higher  $T$  the expansion continues until 800°C. Structure refinements at selected  $T$  revealed that in the 300-400°  $T$  interval almost all H is lost from the structure; the charge unbalance at the anionic O(3)-site is compensated by the oxidation of an equal amount of Fe<sup>2+</sup> to Fe<sup>3+</sup>. Careful refinement of site scatterings and bond length evolution at the relevant octahedral sites shows that the Fe oxidation occurs almost exclusively at the OH-coordinated  $M(1)$ -site, while the  $M(3)$  and  $M(2)$  sites are virtually unaffected. For 400°C <  $T$  < 800°C the resulting oxo-amphibole ("oxo-ferro-richterite") is stable, and its structure is perfectly retained upon reversal to room- $T$ , showing a linear behavior for all the unit cell parameters. The HT-FTIR data collected during the present work add further elements to model the deprotonation process obtained from SC-XRD. The evolution of the overall intensity of the OH-signal, measured on quenched samples for the 3710-3600 cm<sup>-1</sup> integration range (Fig. 3.4), is in agreement with the SC-XRD data and shows no loss of hydrogen for  $T$  up to 400°C while deprotonation occurs in a relatively narrow  $T$  range (100°C); at  $T$  > 600°C, the amphibole is totally anhydrous.

Focusing on the crystal-chemical mechanisms involved in the deprotonation process, inspection of Figure 3.2 shows that for  $T$  < 350°C no significant changes occur in the OH-spectrum and hence in the local environment of the O-H dipole, i.e. in the cation order at the adjacent sites; at 350°C, a weak increase in intensity of the 3656 cm<sup>-1</sup> component is observed. It is assigned to  $^{M(1)}\text{Fe}^{2+M(1)}\text{Fe}^{3+M(3)}\text{Fe}^{2+}$  configurations locally associated with one <sup>W</sup>OH<sup>-</sup> on one side of the strip, and one <sup>W</sup>O<sup>2-</sup> on the other side of the strip. This component is well prominent in the spectrum collected for the sample annealed at 400°C, and becomes the main component in the spectra collected at  $T \geq 450^\circ\text{C}$ . In order to obtain the best possible fitting of the experimental spectra, the digitized spectra obtained from the quenched samples were decomposed by interactive optimization followed by least-squares refinement (Della Ventura *et al.*, 1996) using the Peakfit® program by Jandel Scientific; the background was treated as linear and all bands were modeled as symmetric

Gaussians (Strens, 1974); the spectra were fitted to the smallest number of peaks needed for an accurate description of the spectral profile, based on the knowledge of the behavior of OH-bands in this spectral region accumulated during the last years (e.g. Hawthorne and Della Ventura, 2007). The spectral parameters (position and width) of some overlapping peaks (see for example the  $3656\text{ cm}^{-1}$  component) were refined where these peaks are most prominent, and then fixed during the refinement of the other samples. At convergence, the peak positions were released and the FWHM only were constrained to be roughly constant in all spectra. Figure 3.6 displays one example of spectrum fitting, while all results are shown in Figure 3.7.

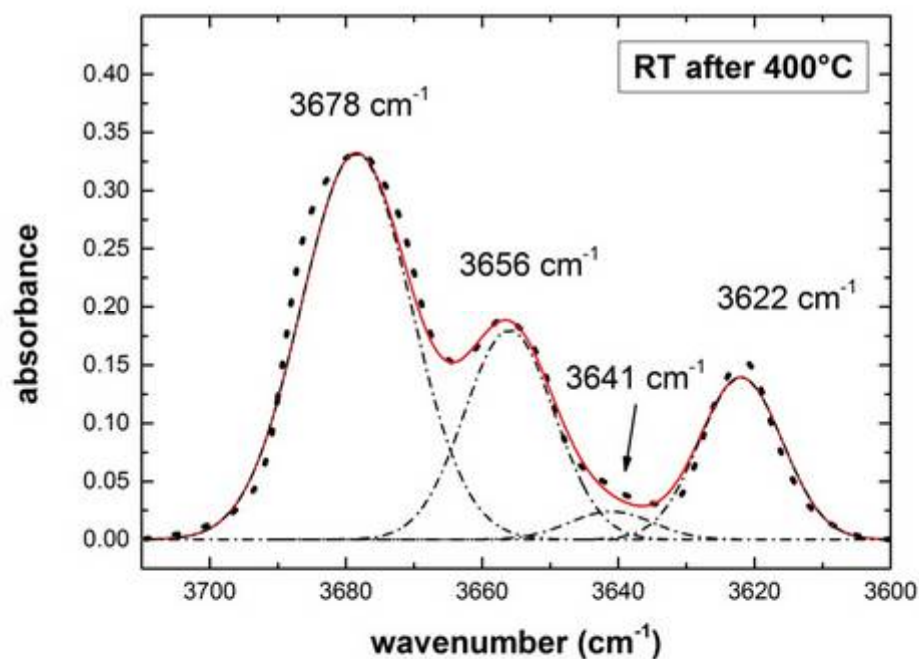


**Figure 3.6.** Bands resolved in the spectra of Figure 3.2. See text for the assignment of the components.

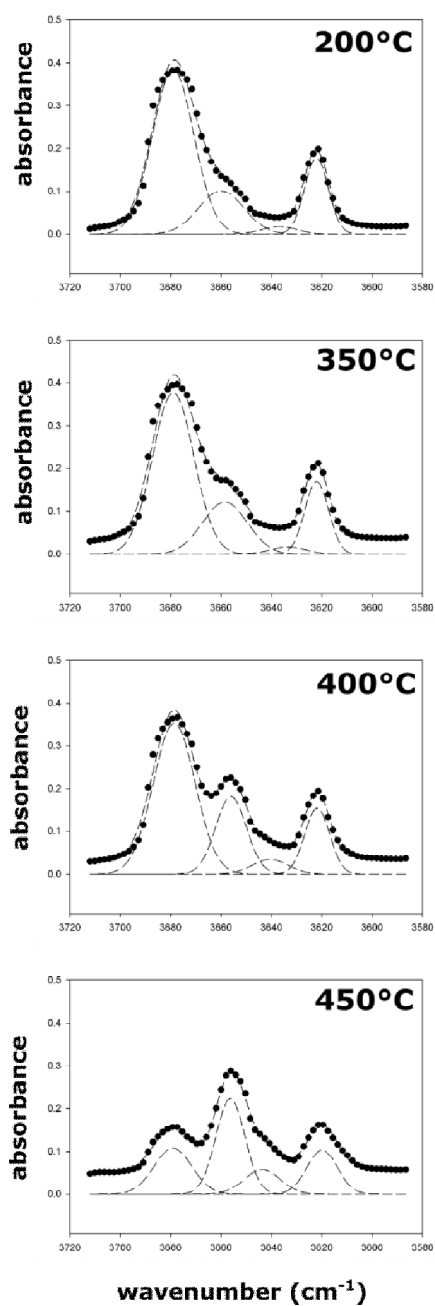


**Figure 3.7.** Fitted OH-stretching spectra collected on quenched samples after annealing at the indicated  $T$ .

Figure 3.8a shows the temperature dependence of the relative integrated intensities of the 3678 and 3656  $\text{cm}^{-1}$  components; it is apparent that between 300 and 400°C the higher-frequency peak only slightly decreases in intensity, whereas it disappears at 500°C. In contrast, the lower-frequency component at 3656  $\text{cm}^{-1}$  slightly increases between 300 and 400°C and increases significantly in the 400-500°C range. Therefore, Figure 3.8a suggests that, in the  $T$  range 400-500°C, notwithstanding a drastic drop in intensity of the overall OH-absorption, the intensities of the two components invert their relations. A better picture of the process is however provided by Figure 3.8b, where the absolute intensities of these two bands are plotted against  $T$ . Note that the spectra have been collected always on the same point of a crystal chip with constant thickness. The data of Figure 3.8b show that the intensity of the 3678  $\text{cm}^{-1}$  component is constant up to 400°C, then decreases drastically, while that of the 3656  $\text{cm}^{-1}$  component slightly increases up to 400°C and then starts dropping. At 500°C, all OH remaining in the amphibole is associated with this band, in other words all remaining OH is associated with an octahedral trimer  $\text{Fe}^{2+}\text{Fe}^{2+}\text{Fe}^{3+}$ . Residual intensity after fitting the 3678, 3656 and 3622  $\text{cm}^{-1}$  bands described above needs an additional peak at 3641  $\text{cm}^{-1}$  to be introduced in the refinement, whose assignment is not clear at the moment. Given its frequency and the controlled chemistry of the system this peak must be due to some configuration involving  $\text{Fe}^{3+}$ , however its intensity is low and it can be neglected for the discussion below.

The behavior of the OH-bands plotted in Figure 3.8b suggests that the oxidation process occurs *via* the creation of a local O-O order; as a matter of fact, if the  $^{M(1)}\text{Fe}^{2+} \rightarrow ^{M(1)}\text{Fe}^{3+}$  reaction occurred randomly, we would have observed in Figure 3.8b a significant increase of the 3656  $\text{cm}^{-1}$  component at the expense of the 3678  $\text{cm}^{-1}$  component, and this is not the case: for  $T > 450^\circ\text{C}$  both bands in fact decrease.



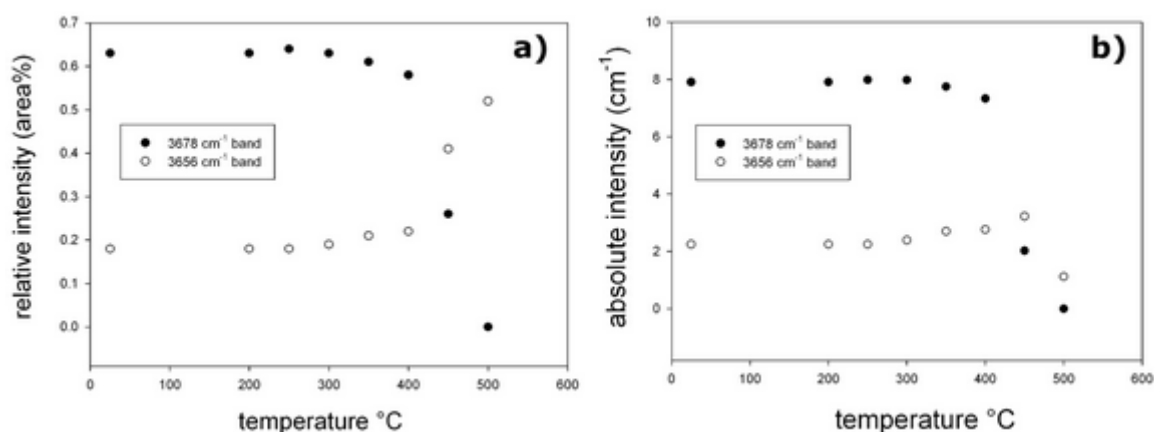


**Figure 3.8.** Temperature dependence of the 3679 vs 3656  $\text{cm}^{-1}$  and components as a function of  $T$ . (a) relative intensity, (b) absolute intensity.

An interesting feature is suggested by the temperature dependence of the 3622  $\text{cm}^{-1}$  band assigned to the configurations including vacant A-site. Figure 3.9 compares the relative (3.9a) and the absolute (3.9b) intensity evolution of this component with increasing  $T$ . The plots show that although this bands quickly disappears at  $T > 400^\circ\text{C}$  (Fig. 3.9b, absolute intensity), its intensity actually increases relatively to all other components (Fig. 3.9a). Thus the plots of Figure 3.9 suggest that the local configurations associated with a vacant A-site are less affected by the deprotonation process than those associated with an occupied A-site. As discussed before, this behavior can be explained by the Coulombic repulsive interactions between Na/K and H in the A-cavity, which imply ordering of the A-cations at the subsites  $A(2)$  and  $A(m)$  at RT and favor deprotonation at HT. Also, the presence of the A-cation may help to obtain local electroneutrality after H loss.

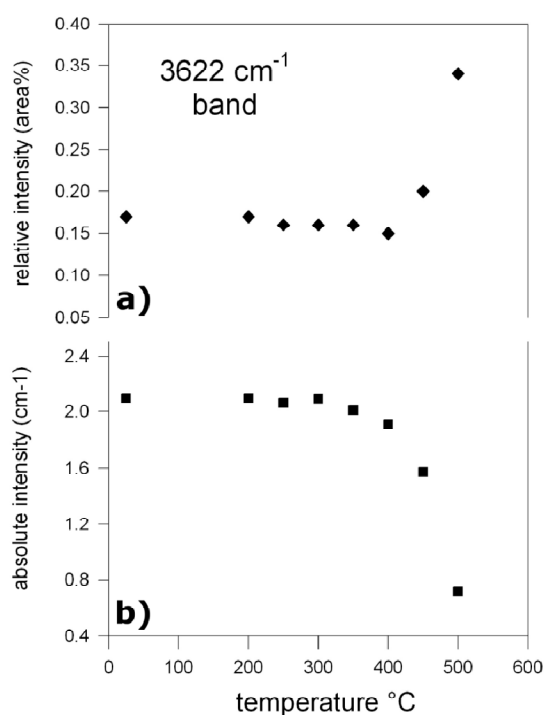


**Figure 3.9.** Temperature dependence of the 3622 cm<sup>-1</sup> and components as a function of  $T$ . (a) relative intensity, (b) absolute intensity.

The data discussed above thus suggest a stringent control of the local configuration on the deprotonation process and this reasoning could be extended to justify the relatively lower thermal stability observed in  $A$ -filled, Fe-rich amphiboles. Pertinent to this point, we can anticipate preliminary experiments done on actinolite that showed a thermal stability > 1100°C. However, the great compositional variety of amphibole suggests a more systematic work on this issue, which we are going to undertake in the next future. This evidence is however also in agreement with previous findings on layer silicates (Zhang *et al.*, 2007). For these minerals, the presence of K at the interlayer site decreases the thermal stability; indeed, sericite has a lower deprotonation temperature (Zhang *et al.*, 2005) than talc (Ward, 1975) and phengite (Wang *et al.*, 2002).

## Chapter 4 Crystal-chemistry of riebeckite from Malawi

---

Riebeckite is a sodic amphibole which crystallizes in the  $C/2m$  space group, its ideal crystal-chemical formula is:  $\square\text{Na}_2\text{Fe}^{2+}_3\text{Fe}^{3+}_2\text{Si}_8\text{O}_{22}(\text{OH})_2$  (i.e. it is the ferro-ferri-counterpart of glaucophane). Its crystal structure has been first determined by Hawthorne (1978), using a fluoro-riebeckite from a granitic pegmatite in the Pikes Peak area of Colorado. Syntheses of riebeckite were performed by Ernst (1962).

A sample of riebeckite from Malawi was chosen for the present work because its composition was very close to that of the end-member and it was available as large and almost homogeneous crystals. A complete crystal-chemical characterization of the specimen was done using a multidisciplinary approach. This step was in fact mandatory for using the amphibole as a starting material for high temperature studies. In this chapter the data are discussed in terms of both long-range (LRO) and short-range order (SRO). We remind here that LRO is defined as site occupancies averaged over the whole crystal, while SRO is related to local configurations and possible clustering. The first step in determining SRO is assigning accurate long-range site occupancies from the single crystal structure refinement (SREF), performed based on chemical data obtained via Electron Microprobe Analysis (EMPA); the possible presence of Li, frequently reported in the literature for this type of amphiboles (Hawthorne, 1978) was checked by means of Laser Ablation Inductively Coupled Plasma Mass Spectroscopy (LA ICP-MS) analysis.

Both powder and single crystal infrared spectra were collected using a Fourier Transform Infra Red Spectrometer (FTIR), to characterize the cation distribution in the octahedra close to the H atom. For amphiboles it is known that the frequency of the OH-stretching absorption in the infrared spectrum is a function of the relative strength of the O-H bond that is highly sensitive to cationic arrangement at the  $M(1)$

and  $M(3)$ -sites. Careful analysis of the OH-stretching spectra thus provide information on the possible SRO at these sites (Hawthorne and Della Ventura, 2007).

## 4.1. Experimental methods

### Single Crystal X-Ray Diffraction (SC-XRD)

The sample used for X-ray diffraction was cut to an approximate size of 40 x 40 x 100  $\mu\text{m}$  and attached to a tapered glass fiber. XRD data were collected at the University of Manitoba, Department of Geological Sciences, with MoK $\alpha$  X-ray radiation on a Bruker D8 three-circle diffractometer equipped with a rotating-anode generator, multilayer optics, and an APEX-II CCD detector. A total of 16000 intensities was collected to 60° 2 $\theta$  using 2–4 second per 0.2° frame with a crystal-to-detector distance of 5 cm. Empirical absorption corrections (SADABS, Sheldrick 2008) were applied. Equivalent reflections were merged (XPREP), resulting in ~5350 reflections; geometrical corrections pertaining to the *C2/m* space group resulted in ~1400 unique reflections. Unit cell dimensions were obtained by least squares refinement of the positions of ~4000 reflections with  $I > 10 \sigma I$  and are listed in Table 4.1.

	Riebeckite from Malawi
a (Å)	9.770(6)
b (Å)	18.080(10)
c (Å)	5.339(3)
$\alpha$ (°)	90
$\beta$ (°)	103.599(13)
$\gamma$ (°)	90
Crystal size ( $\mu\text{m}$ )	40x40x100
Radiation	Mok $\alpha$
No. of total reflections	16415
No. of Ewald reflections	5346
No. unique reflections	1386
R <sub>1</sub> %	1.79
R(int)%	1.19
wR%	5.75
GoF	0.854
Z	2

**Table 4.1.** Unit cell dimensions and crystallographic data from structure refinement of riebeckite from Malawi.

Intensity and reflection values were averaged and reduced to structure factors. The structure was refined in the space group *C2/m* with the SHELXTL version 6.14 program (Bruker AXS) to *R* indices of ~2%. Weighting parameters are given in Table 4.4, and interatomic distances are listed in Table 4.5.

### **Electron Microprobe Analysis (EMPA)**

After the X-ray data collection, the same crystal was embedded in resin and polished for EMPA. Analyses were done at the University of Manitoba, Department of Geological Sciences using a Cameca SX-100 electron microprobe in wavelength-dispersive (WDS) mode; operating conditions were: voltage of 15 kV, a beam current of 20 nA, and a beam size of 1 µm. The following standards were used (*K $\alpha$*  lines): Na, albite; Si, Ca, diopside; F, F-riebeckite; Mg, olivine; Al, andalusite; K, orthoclase; Ti, sphene; Fe, fayalite; Mn, spessartine; Cl, tugtuphite; V,  $\text{VP}_2\text{O}_7$ ; Cr, chromite; and Zn, gahnite. 17 analytical points were measured on the sample. The averaged chemical composition and the related unit formula, calculated on the basis of 24 anions (O, OH, F, Cl), are reported in Table 4.2.

### **LA ICP-MS**

Laser Ablation Induced Coupled Plasma Mass Spectroscopy (LA ICP-MS) analyses were performed at the University of Manitoba, Department of Geological Sciences. The same mount prepared for EMPA was used for LA ICP-MS.

A Merchantek New Wave UP-213 laser ablation device was used with a Nd:YAG source, wavelength = 213 nm, a 4 nsec pulse width, a repetition rate of 10 Hz, a flat top beam, a 3 to 5 J/cm<sup>2</sup> fluence, a beam size of 15-30 µm, a spot ablation mode, an ablation and a background time of 30 s. A Thermo Finnigan Element2 sector field ICP-MS was used with a plasma power of 1386 W, 15.8 l/min of cool gas, 0.86 l/min of auxiliary gas, 0.71 l/min of sample gas, 0.38 l/min of ablation carrier gas and a ThO/Th of 0.15 %.

The analytical method consisted in 10 % mass window, 10 ms of sample time, a sample/peak of 10, an integration window of 10 %, an EScan scanning type and an average integration type. The data reduction was carried out with the Iolite 2.212 software, using a NIST SRM 610 standard reference material and an SiO<sub>2</sub> internal standard.

### **Mössbauer spectroscopy**

A Mössbauer spectrum was collected at RT at the University of Manitoba, Department of Geological Sciences, using a <sup>57</sup>Co(Rh) point source. The sample was finely ground under acetone to avoid oxidation and mixed with sugar. The sample was loaded into a Pb ring (with a 2 mm inner diameter) and covered with tape on both sides. Assuming a recoilless fraction of 0.7, the amount of sample corresponds to an absorber thickness of ~4 mg Fe/cm<sup>2</sup>. The spectrometer was calibrated against α-Fe.

The data evaluation was done with the program RECOIL (Rancourt & Ping 1991; Rancourt *et al.*, 1993; Rancourt *et al.* 1996) using a classical full static Hamiltonian approach with Lorentzian shaped doublets.

## **Fourier Transform Infrared (FTIR) spectroscopy**

IR data were collected using a Bruker Tensor 27 FTIR spectrometer equipped with a KBr beam splitter and a DLATGS detector, at the Department of Geological Sciences, University of Manitoba. A fragment of crystal was finely ground, and a KBr pellet was prepared with a ratio of 5/150 mg; the spectrum was collected at *RT* over the 400-4,000  $\text{cm}^{-1}$  range co-adding 100 scans with a nominal resolution of 4  $\text{cm}^{-1}$ . The spectra decomposition was done by interactive optimization followed by least-squares refinement (Della Ventura *et al.*, 1996) using the Peakfit® program by Jandel Scientific; the background was modeled as linear, and all bands were modeled as symmetric Gaussians (Strens, 1974); the spectrum was fitted with the smallest number of peaks needed for an accurate description of the spectral profile, based on the knowledge of the peak parameters for the OH-bands in this type of amphiboles available in literature (e.g. Hawthorne and Della Ventura, 2007). The full width half maximum (FWHM) was refined for the most prominent peak, and then constrained to be roughly constant for the other peaks.

A single crystal spectrum was also collected on a 111  $\mu\text{m}$ -thick doubly-polished sample using the same experimental set-up.



## 4.2. Experimental results

### EMP Analysis and crystal-chemical formula

The microchemical composition obtained as an average of 17 analysis points is given in Table 4.2. The chemical formula was calculated on the basis of 24 (O, OH, F, Cl) (Hawthorne and Oberti, 2007). Based on the assumption that  $O(3) = (OH,F) = 2$  apfu the  $H_2O$  content was calculated using the MINCALC software. The FeO to  $Fe_2O_3$  ratio was estimated on the basis of electroneutrality requirements. LA ICP-MS analysis gave 71(12) ppm, averaged over 6 analysis points, thus Li was not included in the calculations. The resulting formula (apfu) is given in Table 4.2.

O24	wt%	O24	apfu
SiO <sub>2</sub>	51.52	Si <sup>4+</sup>	7.97
Al <sub>2</sub> O <sub>3</sub>	0.71	Al <sup>3+</sup>	0.03
TiO <sub>2</sub>	0.04	TOTAL T	8
Fe <sub>2</sub> O <sub>3</sub>	14.08	Al <sup>3+</sup>	0.10
FeO	23.09	Ti <sup>4+</sup>	0.01
MnO	0.37	Fe <sup>3+</sup>	1.64
NiO	0.02	Fe <sup>2+</sup>	2.94
ZnO	0.03	Mn <sup>2+</sup>	0.05
MgO	1.12	Mg <sup>2+</sup>	0.26
CaO	0.79	TOTAL C	5
Na <sub>2</sub> O	6.26	Fe <sup>2+</sup>	0.05
K <sub>2</sub> O	0.19	Ca <sup>2+</sup>	0.13
F	0.20	Na <sup>+</sup>	1.82
H <sub>2</sub> O	1.84	TOTAL B	2
O=F	-0.08	Na <sup>+</sup>	0.06
TOTAL	100.18	K <sup>+</sup>	0.04
		TOTAL A	0.10
		F <sup>-</sup>	0.10
		H <sup>+</sup>	1.90
		TOTAL O(3)	2
		O <sup>2-</sup>	23.90
		CATIONS SUM	15.10
		ANIONS SUM	24

**Table 4.2.** Chemical formula of riebeckite from Malawi calculated on the basis of 24 anions.

## Ferric vs. ferrous iron

Mössbauer data evaluation was started using a model with one doublet for  $\text{Fe}^{3+}$  at  $M(2)$  and two for  $\text{Fe}^{2+}$  at  $M(1)$  and  $M(3)$ . However, the calculated amount of  $\text{Fe}^{3+}$  was 32.7 % of total iron, corresponding to 1.5 apfu. Such number was too low to completely fill the  $M(2)$ -sites with  $\text{Fe}^{3+}$  along with the other elements present at  $M(2)$ , as found in EMP analysis (Table 4.2). Furthermore, the three doublet model provided additional inconsistencies in the site occupation, with too small  $\text{Fe}^{2+}$  contents at  $M(1)$  (1.4 apfu) and too high  $\text{Fe}^{2+}$  contents (1.22 apfu) at  $M(3)$ . Thus a new model was chosen including  $\text{Fe}^{2+}$  at  $M(2)$  and an additional doublet corresponding to  $\text{Fe}^{2+}$  on  $M(4)$ . This latter component was added because of a small but detectable shoulder at  $\sim +1.7$  mm/s, which could be resolved introducing a doublet with hyperfine parameters compatible with  $\text{Fe}^{2+}$  at  $M(4)$  (Hafner and Ghose, 1971). Using this model, it was possible to obtain final plausible site populations with fully occupied  $M(1)$ – $M(3)$  octahedral sites. The derived hyperfine parameters (Table 4.3) are consistent with data from literature (Ernst and Wai, 1970), with  $\text{Fe}^{2+}$  at  $M(1)$  having a quadrupole splitting of  $\sim 2.85$  mm/s. Intermediate values of  $\sim 2.5$  mm/s are found for  $\text{Fe}^{2+}$  at  $M(3)$ -site and  $\text{Fe}^{2+}$  at  $M(2)$ -sites displays a value around 2.2 mm/s. The final fitting model is displayed in Figure 4.1. The results of the fitting, including site proportions, are listed in Table 4.3.

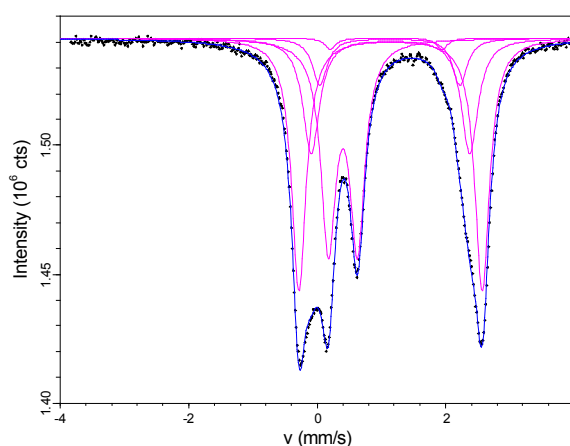


**Figure 4.1.** Analysis of the Mössbauer spectrum of riebeckite from Malawi based on classical full static Hamiltonian approach with Lorentzian shaped doublets.

	Fe <sup>2+</sup> M(1)	Fe <sup>2+</sup> M(3)	Fe <sup>2+</sup> M(2)	Fe <sup>3+</sup> M(2)	Fe <sup>2+</sup> M(4)
<b>IS</b> (mm/s)	1.141(5)	1.140(8)	1.129(5)	0.400(5)	1.074(5)
<b>QS</b> (mm/s)	2.85(2)	2.47(2)	2.18(2)	0.453(8)	1.74(2)
<b>%</b>	39.0(10)	20.4(10)	7.3(10)	31.9(10)	1.4(10)

**Table 4.3.** Mössbauer site distribution parameters and site properties for our sample derived from the fitting shown in Figure 4.1.

The preliminary estimation of the Fe<sup>2+</sup> to Fe<sup>3+</sup> ratio based on the EPMA results shown in Table 4.2 yields the following relative amounts of total Fe<sup>2+</sup> and Fe<sup>3+</sup>.

$$\text{Fe}_{\text{tot}}^{3+} = 1.64 / 4.58 = 0.36$$

$$\text{Fe}_{\text{tot}}^{2+} = 2.94 / 4.58 = 0.64$$

The relative amounts of total Fe<sup>2+</sup> and Fe<sup>3+</sup> throughout the various *M*-sites, calculated from the Mössbauer results listed in Table 4.3, are calculated as follows:

$$\text{Fe}_{\text{tot}}^{3+} = 0.32$$

$$\text{Fe}_{\text{tot}}^{2+} = 0.39 + 0.204 + 0.073 + 0.014 = 0.68$$

There is a very good agreement with the two sets of data, the small difference being due to the fact that the Fe<sup>2+</sup> to Fe<sup>3+</sup> ratio based on the EPMA results is a preliminary estimation. In the following sections we describe how this ratio was properly adjusted while maintaining a consistency with the total iron content detected via EMPA.

### Single crystal Structure REFinement (SREF)

Atomic positions, displacement parameters, and site scattering values were refined using the SHELXT software via least-squares procedure. An anisotropic model was used for the refinement. The weighting parameters are reported in Table 4.4.

Weighting parameters
$\text{Weight} = 1 / [ \sigma^2(F_o^2) + ( 0.0298 * P )^2 + 0.93 * P ] \quad \text{where } P = ( \text{Max} ( F_o^2, 0 ) + 2 * F_c^2 ) / 3$

**Table 4.4.** Weighting parameters used in the structural refinement of riebeckite from Malawi.

SREF allows to calculate the lengths of all bonds within the structure (Table 4.5), and yields absolute scattering values for each site. The site scattering values were refined starting from a simplified site population based on the chemical analysis:  $O(1,7) = O^{2-}$ ,  $T(1,2) = Si$ ,  $M(1,2,3) = Fe$ ,  $M(4) = Na$ , and  $A = K$ .

	Interatomic distances (Å)
T(1)-O(1)	1.6256(15)
T(1)-O(5)	1.6266(12)
T(1)-O(6)	1.6283(13)
T(1)-O(7)	1.6204(10)
<T(1)-O>	1.6252(13)
T(2)-O(2)	1.6254(14)
T(2)-O(4)	1.5996(13)
T(2)-O(5)i	1.6450(12)
T(2)-O(6)	1.6566(12)
<T(2)-O>	
M(1)-O(1)	2.1088(14)
M(1)-O(1)d	2.1088(14)
M(1)-O(2)	2.1128(13)
M(1)-O(2)d	2.1128(13)
M(1)-O(3)	2.1344(12)
M(1)-O(3)e	2.1344(12)
<M(1)-O>	2.1187(13)
M(2)-O(1)	2.1352(13)
M(2)-O(1)f	2.1352(13)
M(2)-O(2)b x2	2.0371(13)
M(2)-O(4)c x2	1.9216(12)
<M(2)-O>	2.0313(13)
M(3)-O(1)a x3	2.1364(13)
M(3)-O(1)	2.1364(13)
M(3)-O(3)e x2	2.0971(17)
<M(3)-O>	2.1233(14)
M(4)-O(2)	2.4322(16)
M(4)-O(2)d	2.4322(16)
M(4)-O(4)c x2	2.3404(14)
M(4)-O(5)c x2	2.8992(15)
M(4)-O(6)c x2	2.4921(16)
<M(4)-O>	2.5410(15)
A(m)-O(3)h	3.2870(190)
A(m)-O(5)	2.9989(119)
A(m)-O(5)a	2.9989(119)
A(m)-O(5)g x2	2.8257(108)
A(m)-O(6)h x2	2.8583(121)
A(m)-O(7)	2.5530(192)
A(m)-O(7)g	2.7016(191)
A(m)-O(7)h	3.1577(190)
<A(m)-O>	2.9065(146)

**Table 4.5.** Interatomic distances (Å) for riebeckite from Malawi. \*a: x, -y, z; b: x, y, z-1; c: -x+1/2, -y+1/2, -z+1; d: -x, y, -z+1; e: -x, -y, -z+1; f: -x, y, -z; g: -x+1, -y, -z; h: -x+1, -y, -z+1; i: x, y, z+1.

Refined atom positions and anisotropic displacement parameters are listed in Appendix 4.1, while observed refined site scattering values are shown in Table 4.15.

### Infrared spectrum

The IR spectra, collected on a KBr pellet (a) and on a single crystal (b) of riebeckite from Malawi, are shown in Figure 4.2. In both cases a linear baseline correction was applied. As can be seen, the spectrum collected from the KBr pellet features sharper and better resolved peaks, while a more rounded profile was obtained from the single crystal, due to the broader absorptions. Three peaks can be clearly seen at 3650, 3635 (3637  $\text{cm}^{-1}$  in the single crystal), and 3618  $\text{cm}^{-1}$ . A further minor component is resolved at about 3667  $\text{cm}^{-1}$  in the spectrum obtained from the crystal. The differences in relative intensities from the two spectra is due to the different widths of the single components between the spectra and possibly to small compositional dishomogeneities.

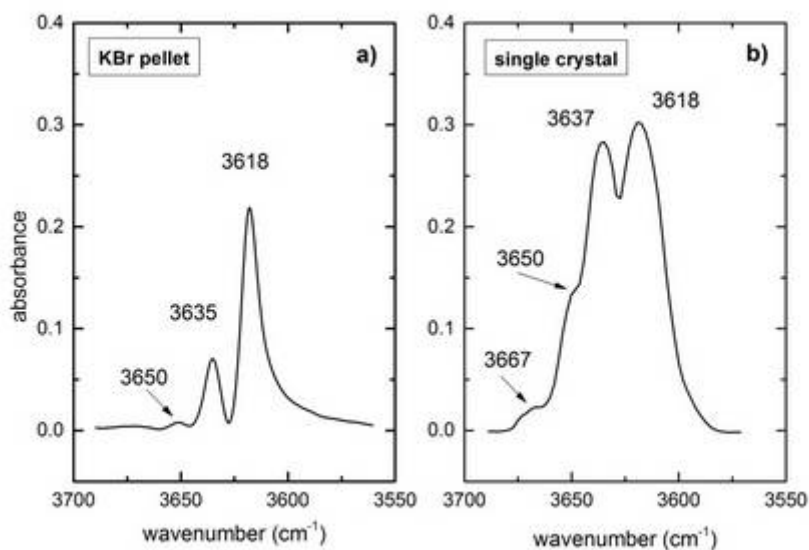


**Figure 4.2.** Background-subtracted IR spectra of the sample studied, collected on a KBr pellet (a) and on a 111  $\mu\text{m}$ -thick single crystal (b).

### 4.3. Long Range Order (LRO)

Site populations can be derived combining structural data, such as site scattering values and bond lengths from SREF, with the results from EMPA shown in Table 4.2.

#### ***M*(1,2,3)-sites occupancies**

*M*(1,2,3)-sites are mainly occupied by  $\text{Fe}^{2+}$  and  $\text{Fe}^{3+}$ , with  $\text{Mg}^{2+}$ ,  $\text{Al}^{3+}$ , and  $\text{Ti}^{4+}$  in minor amounts (Table 4.2). Accordingly with Oberti *et al.* (2007) it can be argued that  $\text{Fe}^{2+}$  is distributed across the *M*(1,2,3)-sites,  $\text{Fe}^{3+}$  is ordered at *M*(2), and  $\text{Mg}^{2+}$  is distributed among *M*(1,2,3). The amount of  $\text{Al}^{3+}$  remaining after allotting the necessary  ${}^7\text{Al}$  to fill the tetrahedral sites to 8 apfu, and the barely detectable amount of  $\text{Ti}^{4+}$  were tentatively assigned to *M*(2)-sites. Starting from the assumption that *M*(1) and *M*(3) sites are fully occupied by  $\text{Mg}^{2+}$  and  $\text{Fe}^{2+}$ , and using refined site scattering values for each *M*-site, a first estimation of the  $^{[6]}$ *M*-sites populations can be done.

#### ***M*(1)-sites**

Considering the observed site scattering value of 49.79 epfu (Table 4.10) and the atomic numbers for Fe and Mg, the population of the two *M*(1)-sites in the amphibole structural formula can be calculated as follows.

$$26 (\text{Fe}^{2+}) + 12 (2 - \text{Fe}^{2+}) = 49.79$$

$${}^{M(1)}\text{Fe}^{2+} = 1.84 \text{ apfu}$$

$${}^{M(1)}\text{Mg}^{2+} = 2 - 1.84 = 0.16 \text{ apfu}$$

### *M(3)-site*

Considering the observed site scattering value of 25.08 epfu (Table 4.10) and the atomic numbers for Fe and Mg, the population of the *M(3)*-site in the amphibole structural formula can be calculated as follows.

$$26 (\text{Fe}^{2+}) + 12 (1 - \text{Fe}^{2+}) = 25.08$$

$${}^{M(3)}\text{Fe}^{2+} = 0.93 \text{ apfu}$$

$${}^{M(3)}\text{Mg}^{2+} = 1 - 0.93 = 0.07 \text{ apfu}$$

### *M(2)-sites*

Since 0.26 apfu of Mg were provided by EMPA, 0.03 apfu of Mg (0.26 – 0.07 – 0.16 = 0.03) remain to be allocated at the *M(2)*-sites. Considering the observed site scattering value of 50.40 epfu (Table 4.10), the results of chemical analysis (Table 4.2) and the atomic numbers for Fe, Mg, Al, Mn and Ti, the amount of  $\text{Fe}^{2+}$  in the two *M(2)*-sites in the amphibole structural formula can be calculated as follows.

$$12 (0.03) + 22 (0.01) + 13 (0.10) + 25 (0.05) + 26 (1.64) + 26 (\text{Fe}^{2+}) = 50.40$$

$${}^{M(2)}\text{Fe}^{2+} = 0.18 \text{ apfu}$$

### *Site population assessment by means of mean bond lengths*

Hawthorne and Oberti (2007) have studied the variables that influence <sup>[6]</sup>*M*-sites cation to oxygen mean bond lengths over a great number of *C2/m* amphibole samples. This study yielded the regression equations listed in Table 4.6. The correlation between  $\langle\langle M(1,2,3)\text{-O}\rangle\rangle$  distances and the  $\langle\langle r^{M(1,2,3)}\rangle\rangle$  (mean aggregate radius of *M(1,2,3)*-cations), along with the correlation between  $\langle\langle M(1,2,3)\text{-O}\rangle\rangle_{\text{obs}}$  and  $\langle\langle M(1,2,3)\text{-O}\rangle\rangle_{\text{calc}}$  distances, calculated from the regression results given in Table 4.6, may be used to adjust the *M(1,2,3)*-sites assignments derived above for our sample



$y$	$x_i$	$y_o$	$a_i$	$R$	st. error of estimate (Å)
$\langle\langle M(1,2,3)-O \rangle\rangle$	$\langle\langle r^{M(1,2,3)} \rangle\rangle$	1.497(15)	0.805(21)	0.950	0.0063
$\langle\langle M(1,2,3)-O \rangle\rangle$	$\langle\langle r^{M(1,2,3)} \rangle\rangle$	1.0709(25)	0.784(14)	0.990	0.0028
	$\langle r^{O(3)} \rangle$		0.347(17)		
	$\langle r^{M(4)} \rangle$		-0.020(3)		
$\langle M(1)-O \rangle$	$\langle r^{M(1)} \rangle$	0.932(24)	0.799(12)	0.990	0.0027
	$\langle r^{O(3)} \rangle$		0.467(16)		
	$\langle r^{M(4)} \rangle$		-0.0532(28)		
	$^{[4]}Al$		0.00358(30)		
$\langle M(2)-O \rangle$	$\langle r^{M(2)} \rangle$	1.476(7)	0.845(9)	0.991	0.0053
$\langle M(3)-O \rangle$	$\langle r^{M(3)} \rangle$	0.627(61)	0.775(19)	0.970	0.0058
	$\langle r^{O(3)} \rangle$		0.728(40)		
	$\langle r^{M(2)} \rangle$		-0.080(12)		
	$\langle r^{M(4)} \rangle$		-0.029(7)		
	$Z^A$		0.0064(18)		

**Table 4.6.** Regression results for  $^{[6]}M$ -sites-O distances and aggregate radii of cations at  $M$ -sites for  $C2/m$  amphiboles (Hawthorne and Oberti, 2007).

The average  $\langle M(1)-O \rangle$ ,  $\langle M(2)-O \rangle$  and  $\langle M(3)-O \rangle$  distances were calculated for our sample while maintaining consistent cation sums ( $\sum M(1) = 2$ ,  $\sum M(2) = 2$ ,  $\sum M(3) = 1$ ). The average  $\langle r^{M(1)} \rangle$ ,  $\langle r^{M(2)} \rangle$  and  $\langle r^{M(3)} \rangle$  values were determined using the site populations from the calculations described above, and the atomic radii for the six-coordinated cation species (Shannon, 1976). The point corresponding to the  $\langle\langle M(1,2,3)-O \rangle\rangle_{\text{obs}}$  as a function of  $\langle\langle r^{M(1,2,3)} \rangle\rangle_{\text{calc}}$  for our sample is plotted with the relative standard deviation in Figure 4.3b. The scatter of  $C2/m$  amphibole samples data from Hawthorne and Oberti (2007) showed in Figure 4.3a, suggests that  $\langle\langle r^{M(1,2,3)} \rangle\rangle$  is not the only variable influencing  $\langle\langle M(1,2,3)-O \rangle\rangle$  distances.

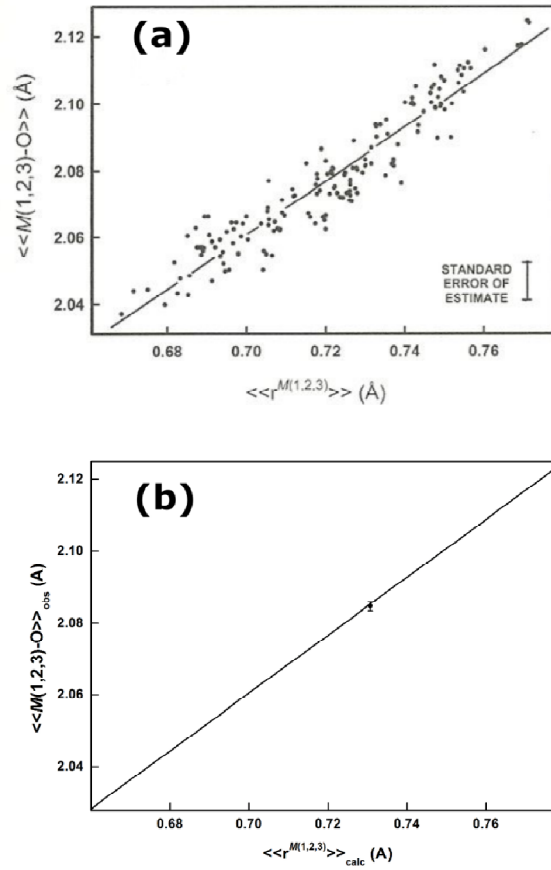


**Figure 4.3.** (a) Data points from Hawthorne and Oberti (2007) of the  $\langle M(1,2,3)-O \rangle$  variation versus the mean radius of the constituent  $M(1,2,3)$ -cations  $\langle r^{M(1,2,3)} \rangle$ . The relatively significant scattering suggests that  $\langle M(1,2,3)-O \rangle$  is affected by additional variables. (b) Variations of the same parameters for riebeckite from Malawi with error bar indicated. The black lines in both graphs are the 1:1 line of the ideal match between observed data and points calculated from the regression relations of Table 4.6.

As discussed above, site populations need to be also verified by studying the associated mean bond lengths. The  $\langle M(1,2,3)-O \rangle_{\text{calc}}$ ,  $\langle M(1)-O \rangle_{\text{calc}}$ ,  $\langle M(2)-O \rangle_{\text{calc}}$  and  $\langle M(3)-O \rangle_{\text{calc}}$  distances were calculated via the regression equations provided in Table 4.6 and listed here:

$$y = ax + by + cz + k$$

(4.1)

$$\langle\langle M(1,2,3)\text{-O}\rangle\rangle_{\text{calc}} = \langle r^{M(1,2,3)}\rangle \times 0.784 + \langle r^{O(3)}\rangle \times 0.347 + \langle r^{M(4)}\rangle \times 0.02 + 1.0709$$

(4.2)

$$\langle M(1)\text{-O}\rangle_{\text{calc}} = \langle r^{M(1)}\rangle \times 0.799 + \langle r^{O(3)}\rangle \times 0.467 + \langle r^{M(4)}\rangle \times 0.0532 + [^4\text{Al}] \times 0.00358 + 0.932$$

(4.3)

$$\langle M(2)\text{-O}\rangle_{\text{calc}} = \langle r^{M(2)}\rangle \times 0.845 + 1.476$$

(4.4)

$$\langle M(3)\text{-O}\rangle_{\text{calc}} = \langle r^{M(3)}\rangle \times 0.775 + \langle r^{O(3)}\rangle \times 0.728 + \langle r^{M(2)}\rangle \times 0.08 + \langle r^{M(4)}\rangle \times 0.029 + Z^A \times 0.0064 + 0.627$$

The point corresponding to the  $\langle\langle M(1,2,3)\text{-O}\rangle\rangle_{\text{obs}}$  as a function of  $\langle\langle M(1,2,3)\text{-O}\rangle\rangle_{\text{calc}}$  determined for our sample via Equation 4.1, is shown in Figure 4.4b. A similar plot from Hawthorne and Oberti (2007) is shown in Figure 4.4a. The minimal scatter in Figure 4.4a, if compared with the scatter in Figures 4.3a, shows how the additional variables ( $\langle r^{O(3)}\rangle$  and  $\langle r^{M(4)}\rangle$ ) affect  $\langle\langle M(1,2,3)\text{-O}\rangle\rangle$  distances.

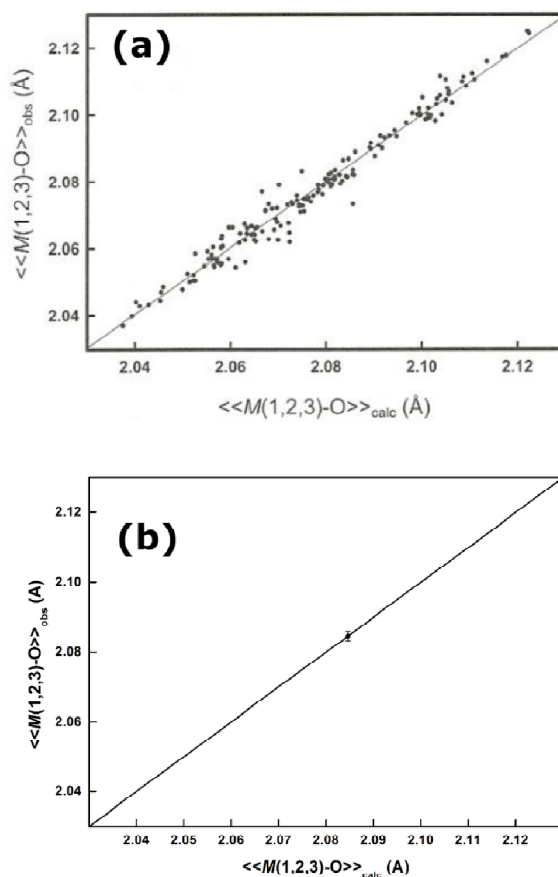


**Figure 4.4.** (a) Data points from Hawthorne and Oberti (2007) of the  $\langle M(1,2,3)\text{-O} \rangle_{\text{obs}}$  variation versus  $\langle M(1,2,3)\text{-O} \rangle_{\text{calc}}$ . Note that the scatter is less than in Figure 4.3a. (b) Variations of the same parameters for riebeckite from Malawi with error bar indicated. The black lines in both graphs are the 1:1 line.

The stepwise linear regression applied to  $\langle M(1)\text{-O} \rangle$  and  $\langle M(3)\text{-O} \rangle$  for  $C2/m$  amphiboles in Hawthorne and Oberti (2007) yielded a significant scatter (Figures 4.5a,d,c,f), due to the fact that the cations occupying the  $M(1)$  and  $M(3)$ -sites are coordinated by anions at the O(3)-site (OH, F, Cl, O), which have different radii. The regression results in Hawthorne and Oberti (2007) showed that  $\langle M(1)\text{-O} \rangle$  and  $\langle M(3)\text{-O} \rangle$  are also affected by  $\langle r^{M(4)} \rangle$  and  $^{[4]}\text{Al}$  content. Figures 4.5d and 4.5f compare the observed and calculated  $\langle M(1)\text{-O} \rangle$  and  $\langle M(3)\text{-O} \rangle$  distances, respectively, and show considerable scatter. In Oberti *et al.* (2007)  $\langle M(1)\text{-O} \rangle$  and  $\langle M(3)\text{-O} \rangle$  distances were compared and it was shown that  $M(1)$  and  $M(3)$  occupancies cannot be accurately

correlated to the sizes of their respective octahedra. On the other hand, Figures 4.5b and 4.5e show minimal scatter, which indicates how  $\langle M(2)-O \rangle_{\text{calc}}$  is affected only by  $\langle r^{M(2)} \rangle$ .

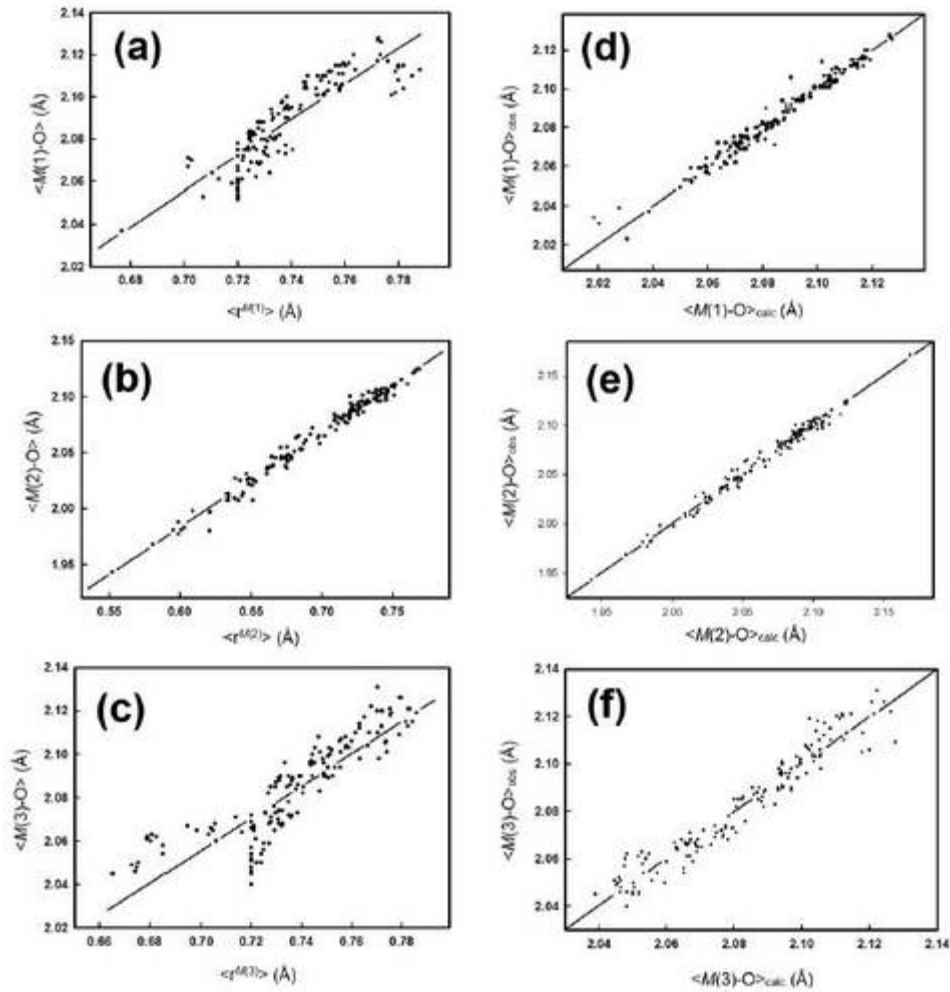


**Figure 4.5.** Variation in  $\langle M-O \rangle$  distance as a function of the mean aggregated radius of the  $M$ -cations in  $C2/m$  amphiboles: (a)  $M(1)$ ; (b)  $M(2)$ ; (c)  $M(3)$ . Comparison of the observed  $\langle M-O \rangle$  distances and the ones calculated from the regression relations of Table 4.6: (d)  $M(1)$ ; (e)  $M(2)$ ; (f)  $M(3)$ . Modified from Hawthorne and Oberti (2007).

For our sample we went through an iterative process in which the departure from the values predicted by the linear regressions were minimized.  $M(1,2,3)$ -sites occupancies were slightly changed maintaining a consistency with the EMPA data, as well as with the observed scattering values obtained from the refinement for each site. At the end of each cycle, the averaged  $\langle M(2)\text{-O} \rangle$  bond distances were calculated with Equation 4.3 and plotted against the observed ones.  $\langle M(2)\text{-O} \rangle$  bond distance was chosen because it is dependent from only one variable, which is the aggregate size of the constituent cations  $\langle r^{M(2)} \rangle$ , and for that reason it can be considered the most reliable parameter to take into account. The process was repeated until the plotted calculated  $\langle M(2)\text{-O} \rangle$  versus the observed  $\langle M(2)\text{-O} \rangle$  point was as close as possible to the 1:1 line. The final occupancy model is the one which yielded the best compromise between minimal calculated to observed site scattering differences, and low discrepancies between the observed and calculated  $\langle M(2)\text{-O} \rangle$ . Figure 4.6b represents the best match between observed and calculated  $\langle M(2)\text{-O} \rangle$  values obtained at the end of the process. A comparison among observed and calculated  $\langle M(1,2,3)\text{-O} \rangle$  distances for the final  $M(1,2,3)$ -sites populations obtained for our sample, are shown in Figures 4.6. The departure from the ideal 1:1 line, corresponding to the linear regression from Hawthorne and Oberti (2007), allows to assess the accuracy of the *M-sites* assignments.

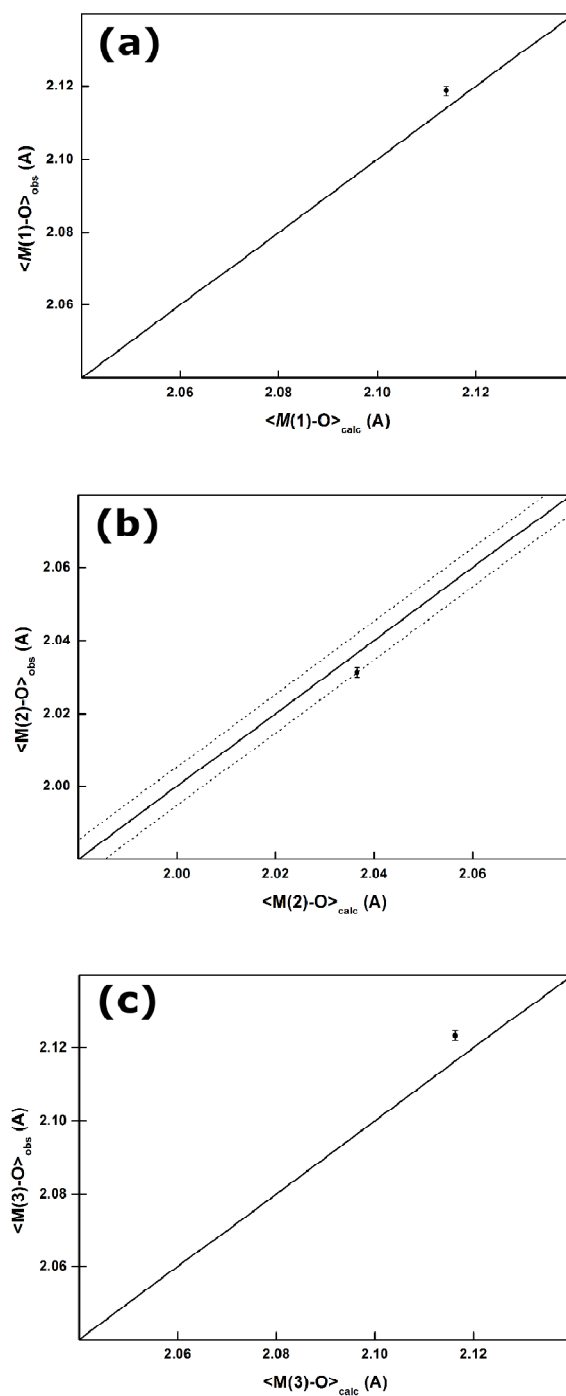


**Figure 4.6.** Comparison of the observed  $\langle M-O \rangle$  distances and the ones calculated from the regression relations of Table 4.6 using the final occupancy model for our sample: (a)  $M(1)$ ; (b)  $M(2)$ ; (c)  $M(3)$ . The plotted calculated  $\langle M(2)-O \rangle$  versus the observed  $\langle M(2)-O \rangle$  point in (b) is within the error reported for the regression relation (dashed lines).

The final site populations obtained for the  $M(1,2,3)$ -sites are listed in Table 4.7. The aggregate size values of the constituent cations, calculated as the average radii weighted for the cation occupancies at the  $M(1,2,3)$ -sites obtained at the end of the iterative process, are shown in Table 4.8.

Site	Site population (apfu)
<b><math>M(1)</math></b>	$1.84\text{Fe}^{2+}; 0.16\text{Mg}^{2+}$
<b><math>M(2)</math></b>	$0.04\text{Mg}^{2+}; 0.08\text{Al}^{3+}; 0.01\text{Ti}^{4+};$ $1.57\text{Fe}^{3+}; 0.25\text{Fe}^{2+}; 0.05\text{Mn}^{2+}$
<b><math>M(3)</math></b>	$0.94\text{Fe}^{2+}; 0.06\text{Mg}^{2+}$

**Table 4.7.** Final site  $M(1,2,3)$ -sites population for our sample, obtained at the end of the iterative process described in the text.

	Calculated mean aggregate radii (Å)
$\langle r^{M(1)} \rangle$	0.7752
$\langle r^{M(2)} \rangle$	0.6634
$\langle r^{M(3)} \rangle$	0.7764
$\langle \langle r^{M(1,2,3)} \rangle \rangle$	0.7307

**Table 4.8.** Averaged sizes of the constituent cations for the  $M(1,2,3)$ -sites, calculated on the final occupancies obtained for our sample at the end of the iterative process.

The final averaged calculated  $M$ -sites to O bond distances, obtained using the method described above, are presented in Table 4.9.

	Bond lengths (Å)
$\langle M(1)\text{-O} \rangle_{\text{calc}}$	2.1140
$\langle M(2)\text{-O} \rangle_{\text{calc}}$	2.0366
$\langle M(3)\text{-O} \rangle_{\text{calc}}$	2.1163
$\langle \langle M(1,2,3)\text{-O} \rangle \rangle_{\text{calc}}$	2.0847

**Table 4.9.** Bond lengths values predicted for our sample. The present values are the final ones obtained at the end of the iterative process.



The calculated *M*-sites scattering values for the final occupancy model are compared with the ones observed from the refinement in Table 4.10. As can be seen the differences are acceptable if we consider the standard deviations associated with the observed values.

Site scattering values:	<i>M</i> (1)	<i>M</i> (2)	<i>M</i> (3)
Obs	49.79(11)	50.40(11)	25.08(7)
Calc	49.79	50.31	25.16
Obs - Calc	0.00	0.09	-0.08

**Table 4.10.** *M*-sites scattering values discrepancies among the calculated and the observed ones. The calculated values are the final ones obtained at the end of the iterative process.

Table 4.11 shows how the site occupancies obtained for iron with the process described are in good agreement with the experimental results from Mössbauer spectroscopy. From Table 4.15 we know that the final total amount of iron in our sample is 4.63 apfu ( $1.84 + 0.94 + 0.25 + 1.57 + 0.03 = 4.63$ ), the relative amounts of either ferrous and ferric iron for each site in our refined model can be calculated as follows.

$$\text{Fe}^{2+} M(1) = 1.84 / 4.61 = 0.40$$

$$\text{Fe}^{2+} M(3) = 0.94 / 4.61 = 0.20$$

$$\text{Fe}^{2+} M(2) = 0.25 / 4.61 = 0.05$$

$$\text{Fe}^{3+} M(2) = 1.57 / 4.61 = 0.34$$

	% from Mössbauer	% from SREF
$\text{Fe}^{2+} M(1)$	39.0(10)	40
$\text{Fe}^{2+} M(3)$	20.4(10)	20
$\text{Fe}^{2+} M(2)$	7.3(10)	5
$\text{Fe}^{3+} M(2)$	31.9(10)	34

**Table 4.11.** Comparison between  $^{57}\text{Fe}$ -sites iron occupancies obtained via Mössbauer spectroscopy and structural refinement.

### T-sites occupancies

From chemical analysis (Table 4.2) we have a total of 0.13 apfu of Al, hence 0.05 apfu of  $\text{Al}^{3+}$  remained after assigning 0.08 apfu of  $\text{Al}^{3+}$  to  $M(2)$ -sites. Accordingly with Oberti *et al.* (2007), we can assign 0.05 apfu of  $\text{Al}^{3+}$  to  $T(1)$ -site (Table 4.15). The remaining 7.95 apfu are occupied by  $\text{Si}^{4+}$ .

### M(4)-sites occupancies

The proportions between  $\text{Fe}^{2+}$  and  $\text{Fe}^{3+}$  obtained by the iterative process described above were used to recalculate the chemical formula with respect to iron. This aim was pursued keeping constant the total amount of iron oxide initially obtained from EMPA. Very little changes in the site occupancies were necessary in order to obtain electroneutrality in the final crystal-chemical formula. This procedure yielded 1.57 apfu of  $\text{Fe}^{3+}$  and 3.06 apfu of total  $\text{Fe}^{2+}$ .  $\text{Fe}^{3+}$  was completely assigned to  $M(2)$ , while 1.84, 0.25 and 0.94 apfu of  $\text{Fe}^{2+}$  were assigned to  $M(1)$ ,  $M(2)$  and  $M(3)$  respectively. The remaining 0.03 apfu of  $\text{Fe}^{2+}$  were hence assigned to  $M(4)$ . 0.13 apfu of  $\text{Ca}^{2+}$  and 1.84 apfu of  $\text{Na}^{+}$  were necessary to complete the  $M(4)$  occupancy (Table 4.15). The obtained calculated site scattering factor is in good agreement with the observed one (Table 4.12). The relative amount of  $\text{Fe}^{2+}$  at  $M(4)$  normalized to the final total iron content can be calculated as follows.

$$\text{Fe}^{2+} M(4) = 0.03 / 4.61 = 0.01$$

The ferrous iron content obtained is in agreement with the results from Mössbauer spectroscopy as shown in Table 4.13.

Site scattering values:	<i>M</i> (4)
Obs	22.7(8)
Calc	23.6
Obs – Calc	-0.9

**Table 4.12.** *M*(4)-sites scattering values differences among the calculated and the observed ones for the final refined site occupancy.

	% from Mössbauer	% from refinement
$\text{Fe}^{2+} M(4)$	1.4(10)	1

**Table 4.13.** Comparison between *M*(4)-sites iron occupancy obtained via Mössbauer spectroscopy and structural refinement.

### A-site occupancy

From the prediction based on chemical analysis we know that *A*-site in our sample is almost completely vacant. The *A*-site population for the final refined site occupancy turned out to be 0.04 apfu of  $\text{K}^+$  and 0.04 apfu of  $\text{Na}^+$  (Table 4.15). In Hawthorne (1983) it was shown that K is always ordered at the *A*(*m*)-site. The very low amount of Na does not allow to determine if it is ordered either at *A*(*m*) or at *A*(2)-site, therefore the refinement was carried out assuming only the *A*(*m*)-site occupied. Calculated site scattering factor at the *A*(*m*)-site is compared with the observed one in Table 4.14. The discrepancy is within the standard deviation of the refined site scattering value, but it has to be noted that this deviation is remarkable. This

uncertainty is due to the relatively large dimensions of the A-site and to the very low occupancy in our sample.

Site scattering values:	<i>A(m)</i>
Obs	2(4)
Calc	1.2
Obs – Calc	+0.8

**Table 4.14.** A-sites scattering values discrepancies among the calculated and the observed ones for the final refined site occupancy.

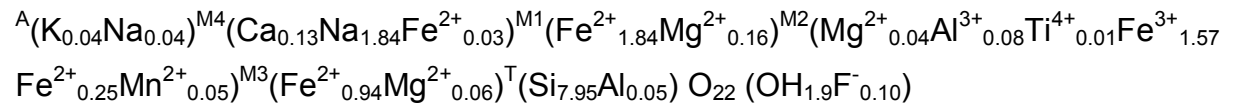
### Final site occupancies

The site occupancies of the final refined model for riebeckite from Malawi are shown in Table 4.15, along with the observed scattering values for each site. As can be seen, the sample turned out to be an almost pure end-member riebeckite ( $\square\text{Na}_2\text{Fe}^{2+}_3\text{Fe}^{3+}_2\text{Si}_8\text{O}_{22}(\text{OH})_2$ ).

Site	Site scattering (epfu)	Site population (apfu)
<i>T</i> (1)	56	4.00 Si <sup>4+</sup>
<i>T</i> (2)	56	3.95Si <sup>4+</sup> ; 0.05Al <sup>3+</sup>
<i>M</i> (1)	49.80(11)	1.84Fe <sup>2+</sup> ; 0.16Mg <sup>2+</sup>
<i>M</i> (2)	50.40(11)	0.04Mg <sup>2+</sup> ; 0.08Al <sup>3+</sup> ; 0.01Ti <sup>4+</sup> ; 1.57Fe <sup>3+</sup> ; 0.25Fe <sup>2+</sup> ; 0.05Mn <sup>2+</sup>
<i>M</i> (3)	25.07(7)	0.94Fe <sup>2+</sup> ; 0.06Mg <sup>2+</sup>
<i>M</i> (4)	22.7(8)	0.13Ca <sup>2+</sup> ; 1.84Na <sup>+</sup> ; 0.03Fe <sup>2+</sup>
<i>A(m)</i>	2(4)	0.04K <sup>+</sup> ; 0.04Na <sup>+</sup>

**Table 4.15.** Final assigned site populations (apfu) and refined scattering values (epfu) for riebeckite from Malawi.

The crystal-chemical formula obtained at the end of the described optimization process is the following:



#### 4.4. FTIR spectroscopy and Short Range Order (SRO)

Once the long range crystal-chemical formula was defined, the riebeckite from Malawi has been studied by means of infrared spectroscopy in order to study its short range order features.

First we will consider the nearest neighbor  $M(1)M(1)M(3)$  arrangements. From SREF analysis results (Table 4.15) we can see that in our sample these sites are exclusively occupied by  $Mg^{2+}$  and  $Fe^{2+}$ , thus the only possible local arrangements are of the  $MgMgMg$ ,  $MgMgFe^{2+}$ ,  $MgFe^{2+}Fe^{2+}$  and  $Fe^{2+}Fe^{2+}Fe^{2+}$  type. Concerning the next nearest neighbor arrangements, from Table 4.15 we can observe that the  $T$ -sites are virtually all occupied by Si, the  $A$ -site is almost totally empty, more than 90% of  $M(4)$ -sites are occupied by Na, and F at O(3) is 5%. Such weak amounts are unlikely to give observable features in the IR spectrum. Due to its better resolved profile, the IR powder spectrum (Figure 4.2a) was studied. In addition, it must be noted that all previous OH-stretching spectroscopy models for amphiboles have been established on powders (e.g. Burns and Strens, 1966 and Hawthorne and Della Ventura, 2007) where issues due to the polarization of the O-H dipole are minimized. As mentioned in Section 4.2, the principal OH-stretching region shows two main components at 3618 and 3635 and a minor one at 3650  $cm^{-1}$ . The OH-band region of the spectrum was decomposed using three Gaussian components (Figure 4.7), following the procedure described in Section 4.1.

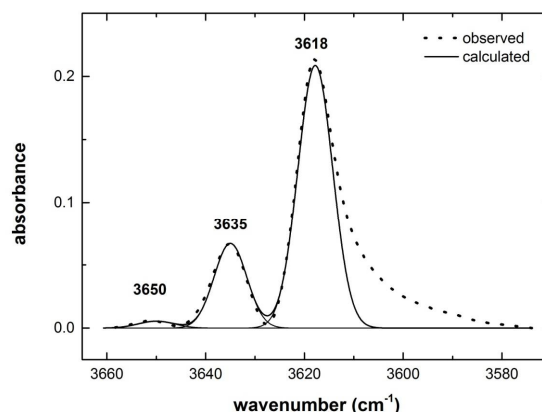


**Figure 4.7.** Fitting of the principal OH-stretching region in the IR spectrum of the studied sample.

According to the systematic work on the FTIR spectroscopy of Fe-amphiboles with different cation occupancies at the octahedral sites (e.g. Robert *et al.*, 1989; Della Ventura, 1992; Della Ventura *et al.*, 1996, 1997, 1998, 2005; Iezzi *et al.*, 2004, 2005), and considering the results of SREF analysis (Table 4.15), the main band at  $3618\text{ cm}^{-1}$  is assigned to the  $\text{Fe}^{2+}\text{Fe}^{2+}\text{Fe}^{2+}\text{-OH}$  local environment. Iezzi *et al.* (2005) reported a  $15 - 18\text{ cm}^{-1}$  shift for  $\text{Fe}^{2+}$  substituting  $\text{Mg}^{2+}$  in synthetic tremolite. Following this indication and considering the  $17$  to  $15\text{ cm}^{-1}$  shift between the three observed bands, we assign the  $3635\text{ cm}^{-1}$  band to  $\text{Fe}^{2+}\text{Fe}^{2+}\text{Mg-OH}$  and the  $3650\text{ cm}^{-1}$  band to  $\text{Fe}^{2+}\text{MgMg-OH}$  local configurations. In Table 4.16, for each component we list the position ( $\text{cm}^{-1}$ ), the Full Width Half Maximum (FWHM), the corresponding local arrangement, and the relative intensity expressed as % with respect to the total OH-stretching band area.

Wavenumber ( $\text{cm}^{-1}$ )	Local arrangement	FWHM	Relative area
3650	$\text{Fe}^{2+}\text{MgMg-OH-}\square$	7.9	2%
3635	$\text{Fe}^{2+}\text{Fe}^{2+}\text{Mg-OH-}\square$	7.3	23%
3618	$\text{Fe}^{2+}\text{Fe}^{2+}\text{Fe}^{2+}\text{-OH-}\square$	8.2	75%

**Table 4.16.** FTIR spectrum fitting interpretation.

Hawthorne *et al.* (1996) showed that binary site occupancies (where only  $\text{Mg}^{2+}$  and a generic  $\text{M}^{2+}$  are present) at the  $M(1)$  and  $M(2)$  can be related to the observed relative intensities of the four bands in the OH-spectrum. The Equations 4.5 suggested by Burns and Strens (1966) were applied to our sample, assuming that there is no variation in molar absorptivity with band frequency within a single sample.

(4.5)

$$\text{Mg}^{2+}_{M(1,3)} = 3I^{\circ}_A + 2I^{\circ}_B + I^{\circ}_C$$

$$\text{M}^{2+}_{M(1,3)} = I^{\circ}_B + 2I^{\circ}_C + 3I^{\circ}_D$$

Where  $I^{\circ}_A$ ,  $I^{\circ}_B$ ,  $I^{\circ}_C$  and  $I^{\circ}_D$ , are the observed relative intensities assigned respectively to  $\text{MgMgMg}$ ,  $\text{MgMgM}^{2+}$ ,  $\text{MgM}^{2+}\text{M}^{2+}$  and  $\text{M}^{2+}\text{M}^{2+}\text{M}^{2+}$  local configurations. Using the above equations the following results are obtained for Mg vs.  $\text{Fe}^{2+}$  at  $M(1)$  and  $M(3)$ .

$$\text{Mg}^{2+}_{M(1,3)} = 2 \times 0.02 + 0.23 = 0.27 \text{ apfu}$$

$$\text{Fe}^{2+}_{M(1,3)} = 0.02 + 2 \times 0.23 + 3 \times 0.75 = 2.73 \text{ apfu}$$

Considering inherent uncertainties associated with the estimation of the IR intensities both these values are in good agreement with the LRO results obtained from single crystal refinement analysis (Table 4.17):

$$\text{Mg}^{2+}_{M(1,3)} = 0.16 \text{ apfu} + 0.06 \text{ apfu} = 0.22 \text{ apfu}$$

$$\text{Fe}^{2+}_{M(1,3)} = 1.84 \text{ apfu} + 0.94 \text{ apfu} = 2.78 \text{ apfu}$$

	FTIR (apfu)	SREF (apfu)
<b>Mg</b> <sup>2+</sup> <sub>M(1,3)</sub>	0.27	0.22
<b>Fe</b> <sup>2+</sup> <sub>M(1,3)</sub>	2.73	2.78

**Table 4.17.** Comparison between populations of  $M(1,3)$ -sites obtained via SREF, with those derived by FTIR data applying the equation from Burns and Strens (1966).



Following Strens (1966, 1974) and Law (1976), we can calculate the relative band intensities  $I_{B,C,D}^C$ , assuming that Mg and  $Fe^{2+}$  are totally disordered through the  $M(1,3)$ -sites, using Equations 4.6:

(4.6)

$$I_B^C = x_{M(1)}^2 y_{M(3)} + 2x_{M(1)}y_{M(1)}x_{M(3)}$$

$$I_C^C = y_{M(1)}^2 x_{M(3)} + 2x_{M(1)}y_{M(1)}y_{M(3)}$$

$$I_D^C = y_{M(1)}^2 y_{M(3)}$$

where  $y_{M(1)} = Fe^{2+}$  for each one of the two  $M(1)$ -sites;  $y_{M(3)} = Fe^{2+}$  at  $M(3)$ -site;  $x_{M(1)} = Mg$  for each one of the two  $M(1)$ -sites; and  $x_{M(3)} = Mg$  at  $M(3)$ -site.

The site occupancies of our sample (Table 4.15) are:  $y_{M(1)} = 1.84 \text{ apfu} / 2 = 0.92 \text{ apfu}$ ;  $y_{M(3)} = 0.94 \text{ apfu}$ ;  $x_{M(1)} = 0.16 / 2 = 0.08 \text{ apfu}$ ;  $x_{M(3)} = 0.06 \text{ apfu}$ . Hence applying Equations 4.6 we have:

$$I_B^C = (0.08)^2 (0.94) + 2(0.08)(0.92)(0.06) = 0.02 = 2\%$$

$$I_C^C = (0.92)^2 (0.06) + 2(0.08)(0.92)(0.94) = 0.19 = 19\%$$

$$I_D^C = (0.92)^2 (0.94) = 0.079 = 79\%$$

Since there is a reasonable agreement between the observed relative intensities and the calculated ones (Table 4.18), we can conclude that in our sample  $Fe^{2+}$  and Mg are disordered over the  $M(1,3)$ -sites.

Component	Local arrangement	Calculated intensity	Observed intensity
<b>B</b>	$Fe^{2+}MgMg-OH-\square$	2	2
<b>C</b>	$Fe^{2+}Fe^{2+}Mg-OH-\square$	19	23
<b>D</b>	$Fe^{2+}Fe^{2+}Fe^{2+}-OH-\square$	79	75

**Table 4.18.** Comparison between the observed IR relative intensity and the ones estimated using Equations 4.6.

Riebeckite from Malawi.											
Site	x	y	z	s.o.f.	U11	U22	U33	U23	U13	U12	Ueq
<b>T(1)</b>	0.28135(4)	0.08585(2)	0.28993(7)	1.00000	0.00753(18)	0.00753(17)	0.00668(17)	-0.00018(11)	0.00166(13)	-0.00028(11)	0.00696(11)
<b>T(2)</b>	0.29082(4)	0.17032(2)	0.80147(7)	1.00000	0.00765(18)	0.00707(17)	0.00646(17)	-0.00037(11)	0.00188(13)	-0.00098(11)	0.00702(11)
<b>M(1)</b>	0.00000	0.09097(2)	0.50000	0.4787(11)	0.00985(17)	0.00754(17)	0.00668(16)	0.00000	0.00263(11)	0.00000	0.00791(12)
<b>M(2)</b>	0.00000	0.18344(2)	0.00000	0.4846(10)	0.00695(15)	0.00636(15)	0.00682(15)	0.00000	0.00191(10)	0.00000	0.00666(11)
<b>M(3)</b>	0.00000	0.00000	0.00000	0.2411(7)	0.0096(2)	0.0061(2)	0.0070(2)	0.00000	0.00173(14)	0.00000	0.00766(14)
<b>M(4)</b>	0.00000	0.27831(5)	0.50000	0.515(2)	0.0176(5)	0.0116(4)	0.0176(4)	0.00000	0.0119(3)	0.00000	0.0143(3)
<b>A(m)</b>	0.5435(2)	0.00000	0.100(4)	0.0232(17)	0.050(6)						
<b>O(1)</b>	0.11065(11)	0.09176(5)	0.2052(2)	1.00000	0.0081(4)	0.0095(5)	0.0089(4)	-0.0003(3)	0.0017(4)	-0.0003(3)	0.0089(2)
<b>O(2)</b>	0.11980(10)	0.17278(6)	0.73710(19)	1.00000	0.0081(4)	0.0106(4)	0.0095(4)	-0.0009(3)	0.0017(3)	-0.0005(3)	0.00944(19)
<b>O(3)</b>	0.11121(15)	0.00000	0.7085(3)	0.516(4)	0.0132(7)	0.0114(7)	0.0121(7)	0.00000	0.0033(5)	0.00000	0.0122(4)
<b>O(4)</b>	0.36663(10)	0.24867(6)	0.79973(19)	1.00000	0.0124(4)	0.0089(4)	0.0115(4)	-0.0009(4)	0.0032(4)	-0.0033(3)	0.0109(2)
<b>O(5)</b>	0.34921(10)	0.12935(6)	0.08134(18)	1.00000	0.0097(4)	0.0142(5)	0.0097(4)	0.0038(3)	0.0025(3)	-0.0001(3)	0.0112(2)
<b>O(6)</b>	0.33984(10)	0.12119(6)	0.57560(18)	1.00000	0.0107(4)	0.0124(5)	0.0090(4)	-0.0033(3)	0.0022(3)	-0.0002(3)	0.0107(2)
<b>O(7)</b>	0.32988(15)	0.00000	0.2985(3)	0.50000	0.0121(6)	0.0068(6)	0.0163(6)	0.00000	0.0028(5)	0.00000	0.0118(3)

**Appendix 4.1:** Atoms positions and anisotropic-displacement parameters ( $\text{\AA}^2$ ) for riebeckite from Malawi.

## **Chapter 5    HT-FTIR   experiments   on   riebeckite   from Malawi**

---

In the following chapters the HT study done on the riebeckite from Malawi, characterized in Chapter 4, will be described. Several heating procedures were used, both on powders and on single crystals. The experiments have been designed based on the experience previously accumulated on potassic-ferro-richterite, as described in Chapter 3. This work is intended to try addressing the points raised by all early works done during the 1970-1980's on Fe-amphiboles (see Chapter 2), and the results obtained on potassic-ferro-richterite. The work has been done by using extensively FTIR techniques, although the information from this technique has been extensively integrated with the data from different spectroscopic and X-ray techniques.

## 5.1. Experimental methods

Non-polarized single crystal HT-FTIR spectra were collected at INFN (Frascati) using a Linkam 1400XY heating stage fitted on a Bruker Hyperion 3000 FTIR microscope, equipped with a 15X Schwarzschild objective and a MCT N-cooled detector. The microscope was attached to a Vertex optical bench 70v equipped with a KBr beamsplitter and a globar IR source with a beam diameter of 100  $\mu\text{m}$ ; the nominal resolution was set at 4  $\text{cm}^{-1}$  and 256 spectra were co-added for both mineral and background.

A fragment of the same crystal was ground into a fine powder that was pressed, between two polished steel disks using a vise. Compact pure amphibole pellets with fairly homogeneous thicknesses were obtained, and these were used to collect HT-FTIR spectra using the same experimental set-up described for single crystal analysis.

Each sample was heated with a 10°C/min rate; every 50°C a spectrum was collected *in situ*, then it was rapidly quenched and a spectrum was collected at RT, the temperature was restored quickly (50°C/min) and the ramp was continued at the same 10°C/min rate. This process continued up to the temperature value, where no OH-absorption band remained in the IR spectrum.

## **5.2. Heating FTIR experiment on single crystal**

The results presented in this section were obtained on a crystal fragment doubly-polished to a thickness of 111  $\mu\text{m}$ . Considering that there was no need to obtain absolute concentrations, but only the relative variations of the OH-contents as a function of  $T$ , the data were collected with unpolarized radiation on a randomly oriented crystal.

### **FTIR spectra collected on quenched samples**

Selected spectra collected at  $RT$  after quenching from target temperatures up to  $650^\circ\text{C}$ , are shown in Figure 5.1. The IR spectrum of the untreated amphibole, obtained with powdered sample in a KBr pellet, has already been described in Chapter 4; it consists of three main components at about 3650, 3637, 3618  $\text{cm}^{-1}$ , with a minor component at about 3667  $\text{cm}^{-1}$ . Inspection of Figure 5.1 shows that for increasing  $T$  up to  $500^\circ\text{C}$  there are no major changes in both shapes and intensity of the peaks; a slight intensity decrease can be seen between 500 and  $550^\circ\text{C}$ , while an evident drop is observed between 550 and  $600^\circ\text{C}$ . The spectrum collected on the sample quenched after heating at  $650^\circ\text{C}$  does not show any absorption in the OH-stretching region.

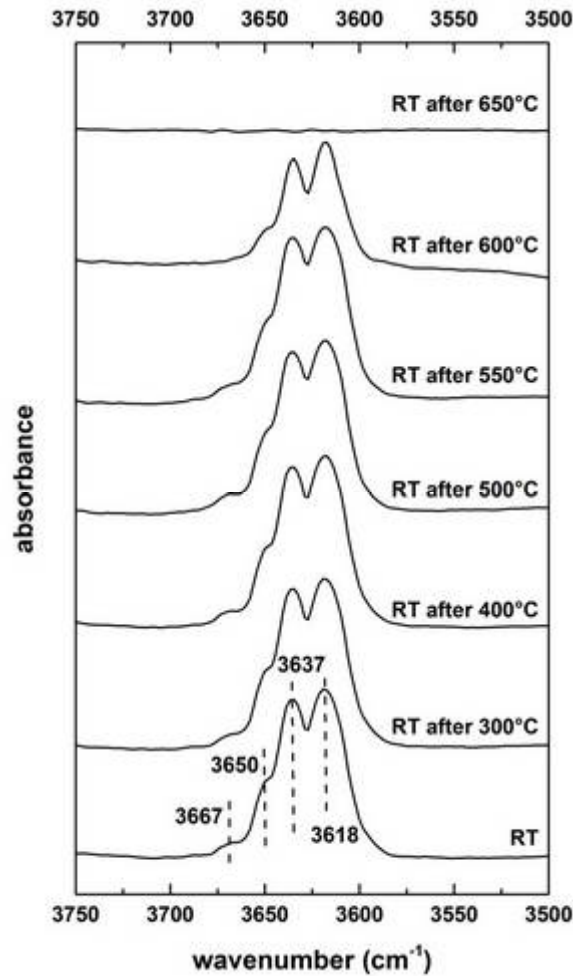


**Figure 5.1.** OH-stretching spectra measured at RT after quenching from any target  $T$ ; 111  $\mu\text{m}$ -thick doubly-polished section. Spectra plotted with the same absorbances scale.

Figure 5.2 displays the deconvolution, using Gaussian components, of the same spectra as in Figure 5.1. As discussed in Chapter 4, the fitted component bands are assigned respectively to the following  $M(1,3)$  local configurations:  $\text{MgMgFe}^{2+}$  ( $3650\text{ cm}^{-1}$ );  $\text{MgFe}^{2+}\text{Fe}^{2+}$  ( $3637\text{ cm}^{-1}$ ); and  $\text{Fe}^{2+}\text{Fe}^{2+}\text{Fe}^{2+}$  ( $3618\text{ cm}^{-1}$ ). Due to small compositional inhomogeneity, the sample used for HT experiments turned out to be slightly richer in Mg than the one described in Chapter 4. From Figure 5.2a it can be seen that the 3650 and 3637 components have slightly higher relative intensities if compared with the corresponding components in Figure 4.7. Furthermore, in the single crystal analyzed here a band at  $3667\text{ cm}^{-1}$  is present, even though its absorbance is barely detectable.

On the basis of the literature data (e.g. Hawthorne and Della Ventura, 2007) we can assign the  $3667\text{ cm}^{-1}$  band to the  $\text{MgMgMg}$  local configuration. All components present in the untreated sample, are also present in the spectra obtained after heat-treatment up to  $600^\circ\text{C}$ .

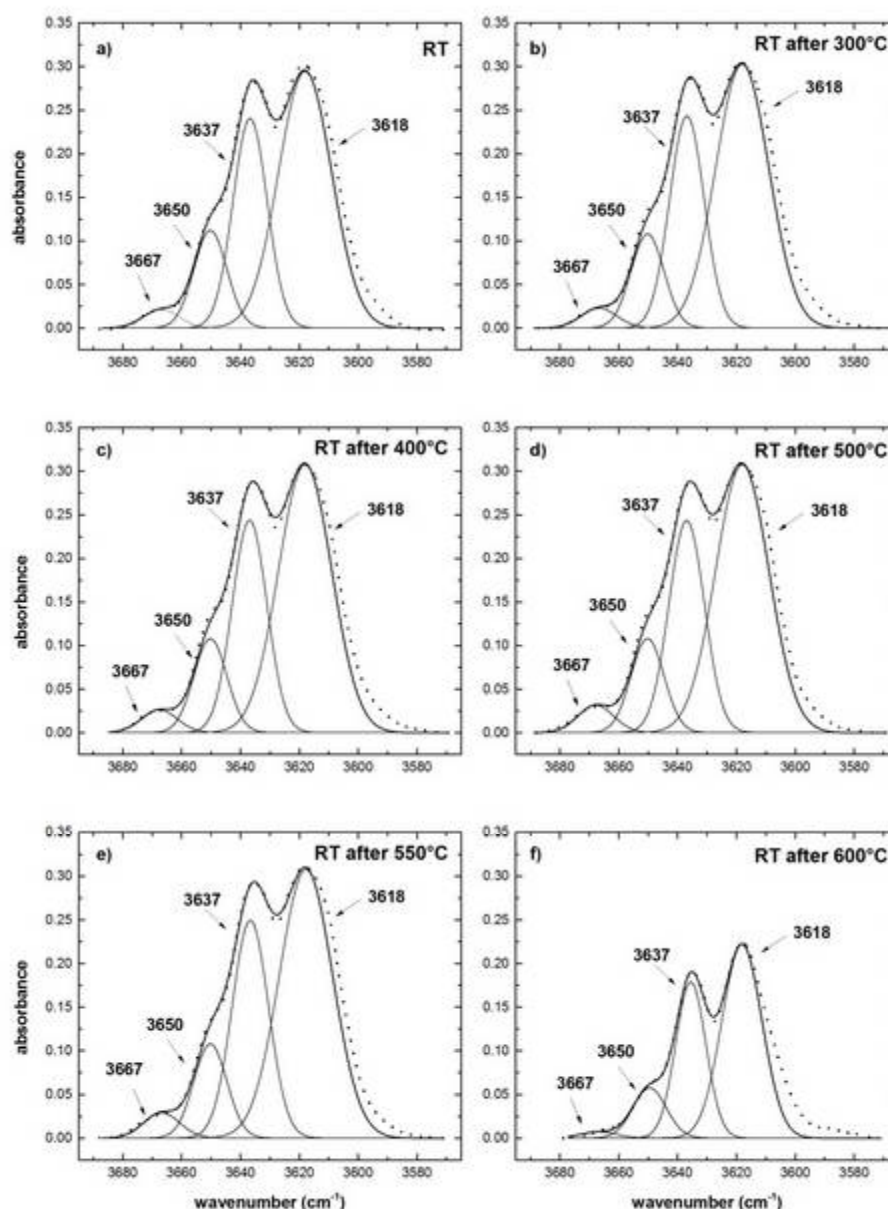


**Figure 5.2.** Decomposition of the spectra of Figure 5.1. The resolved absorption bands are respectively assigned to the following local configurations:  $\text{MgMgMg}$  ( $3667\text{ cm}^{-1}$ ),  $\text{MgMgFe}^{2+}$  ( $3650\text{ cm}^{-1}$ ),  $\text{MgFe}^{2+}\text{Fe}^{2+}$  ( $3637\text{ cm}^{-1}$ ) and  $\text{Fe}^{2+}\text{Fe}^{2+}\text{Fe}^{2+}$  ( $3618\text{ cm}^{-1}$ ).

Table 5.1 gives the numerical results of the fittings shown in Figure 5.2. The total absorbance, as well as the relative intensity of single components, virtually does not change up to 500°C. As can be seen from Figure 5.1, after heat-treatment at 600°C the overall OH-absorbance decreases considerably, but the relative absorbance of the single components, as well as their widths, remains virtually constant.

	MgMgMg-OH-□	Fe <sup>2+</sup> MgMg-OH-□	Fe <sup>2+</sup> Fe <sup>2+</sup> Mg-OH-□	Fe <sup>2+</sup> Fe <sup>2+</sup> Fe <sup>2+</sup> -OH-□
<b>RT</b>				
center (cm <sup>-1</sup> ):	3667	3650	3637	3618
FWHM:	14.13	12.95	13.42	21.19
area%:	3	13	29	55
<b>RT after 300°C</b>				
center (cm <sup>-1</sup> ):	3667	3650	3637	3618
FWHM:	14.13	12.95	13.62	21.19
area%:	3	12	29	56
<b>RT after 400°C</b>				
center (cm <sup>-1</sup> ):	3667	3650	3637	3618
FWHM:	14.13	12.95	13.69	21.19
area%:	3	12	29	56
<b>RT after 500°C</b>				
center (cm <sup>-1</sup> ):	3667	3650	3637	3618
FWHM:	14.13	12.95	13.99	21.19
area%:	4	12	29	55
<b>RT after 550°C</b>				
center (cm <sup>-1</sup> ):	3667	3650	3637	3618
FWHM:	14.13	12.95	14.33	21.19
area%:	3	11	30	55
<b>RT after 600°C</b>				
center (cm <sup>-1</sup> ):	3667	3650	3636	3618
FWHM:	14.12	13.15	11.77	15.86
area%:	2	11	33	54

**Table 5.1.** Refined peak parameters for the component bands resulting from the fittings shown in Figure 5.2.

Figure 5.3 shows how the relative absorbance of each band change slightly in the 500 - 600°C temperature range, even though the total absorbance decreases considerably (Figure 5.1).



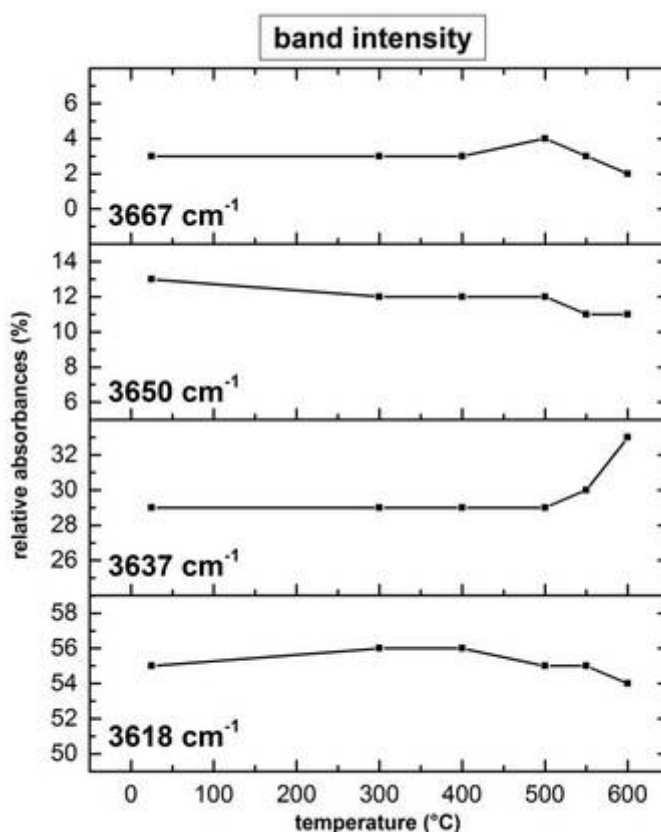


**Figure 5.3.** Evolution of the relative absorbances for the single components (spectra recorded after quenching) for increasing  $T$ .

### ***In situ* FTIR spectra**

IR spectra collected *in situ* (Figure 5.4) show that all bands progressively shift toward lower wavenumbers and broaden for increasing  $T$ . A significant and unexpected increase in linear intensity is also observed, giving a growth in total absorbance.

Because of the band broadening, the three main components, well resolved in the spectrum of the untreated sample, are still recognizable up to 500°C, even though they appear less sharp and progressively shifted toward lower frequencies. At 600°C three main peaks at about 3625, 3607, and 3597 cm<sup>-1</sup>, along with several additional less evident components, are visible. Considering their relative positions

and the shift induced by temperature, it seems reasonable to assign them to the  $\text{MgMgFe}^{2+}$ ;  $\text{MgFe}^{2+}\text{Fe}^{2+}$  and  $\text{Fe}^{2+}\text{Fe}^{2+}\text{Fe}^{2+}$  local configurations at  $M(1,3)$ .

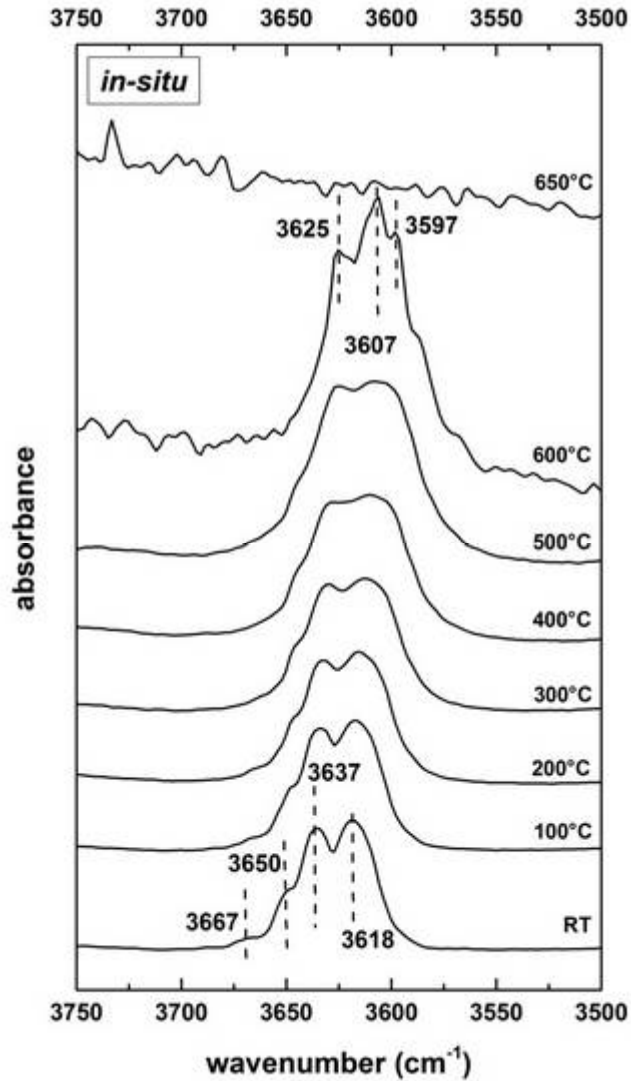


**Figure 5.4.** OH-stretching region of the IR spectra measured *in situ* for increasing  $T$ . To avoid overcrowding of the figure only one spectrum every 100°C is shown; doubly-polished 111  $\mu\text{m}$ -thick section. Spectra plotted with the same absorbance scale.

As mentioned above, band broadening and peak shift are the main effects observed for the FTIR spectra collected under varying  $T$ , thus the overall profile of the OH-bands is deeply modified. We tried to decompose the spectra collected *in situ* using the same procedure described for the spectra collected on quenched samples,

however no definitive and stable results could be obtained, thus only the integrated intensity variation in the OH-stretching region will be discussed in the following.

### The evolution of the OH-band intensity as a function of $T$

Figure 5.5 shows the evolution, as a function of  $T$ , of the integrated OH-absorbance (integration range  $3711\text{--}3560\text{ cm}^{-1}$ ) measured *in situ* and at RT after quenching the sample. Two very different trends are observed: the data collected *in situ* (red dots) show a significant increase, with a total absorbance that at  $550^\circ\text{C}$  is more than doubled with respect to the initial value measured on the untreated sample. For  $T > 550^\circ\text{C}$  the intensity drops to zero, and no OH-intensity is detected at  $650^\circ\text{C}$ . The absorbance measured after quenching the sample, on the contrary, is constant up to  $550^\circ\text{C}$ , and drops abruptly in the  $550\text{--}600^\circ\text{C}$  range.

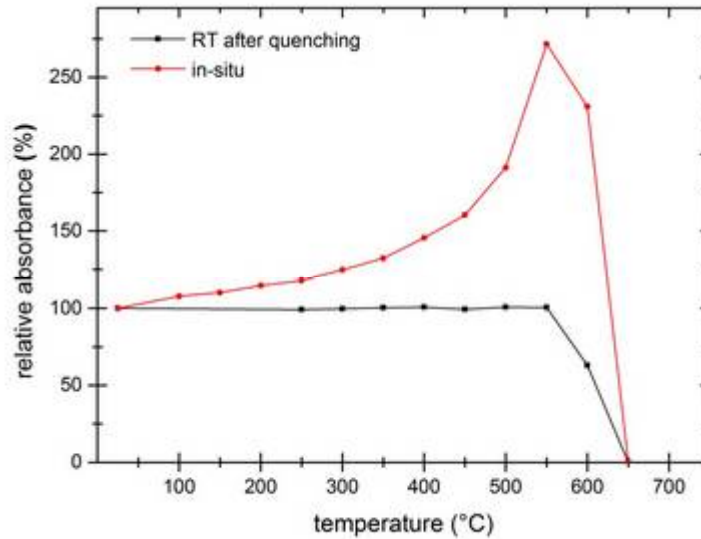


**Figure 5.5.** OH-stretching integrated absorbance (integration range is  $3711\text{--}3560\text{ cm}^{-1}$ ) as a function of  $T$ ,  $111\text{ }\mu\text{m}$  thick doubly-polished section.

The temperature dependence of the OH-band intensities measured *in situ* during HT-FTIR experiments has been described by several previous authors (e.g. Zhang *et al.*, 2007, 2010; Tokiwai and Nakashima, 2010) for different mineral species. This important topic in mineral spectroscopy has been explained based on the dependence with  $T$  of the constant of proportionality (the molar absorption coefficient,  $\varepsilon$ ) between absorbance and concentration in the Beer-Lambert equation (Tokiwai and Nakashima, 2010). In all previous studies, however, a decrease in the OH-intensity has been reported, while in this case a strong increase of the OH-band intensity is observed. Up to the present, such a feature has been reported only for synthetic potassic-ferro-richterite (Chapter 3).

### **5.3. HT-FTIR experiment on powders**

Following Addison *et al.* (1962a) who noted and enhanced iron oxidation when using smaller amphibole fibers, we studied a powdered riebeckite to characterize the role of grain size on the final results from HT experiments. FTIR data on powders were completed with HT X-ray powder diffraction and Mössbauer analysis, which will be discussed later in Chapter 6.

#### **FTIR spectra collected on quenched samples**

A selection of the IR spectra collected at RT after quenching from target temperatures up to 650°C is shown in Figure 5.6. As described in Chapter 4, the IR spectrum of the untreated amphibole consists of three components at 3650, 3635, 3618  $\text{cm}^{-1}$  respectively. Figure 5.6 shows that for increasing  $T$  there are no major changes in both shape and intensity of the peaks up to 400°C; a slight intensity decrease occurs between 400 and 500°C, while an evident drop is observed between 550 and 600°C. The spectrum collected on the sample quenched after heating at 600°C shows no absorption in the OH-stretching region.

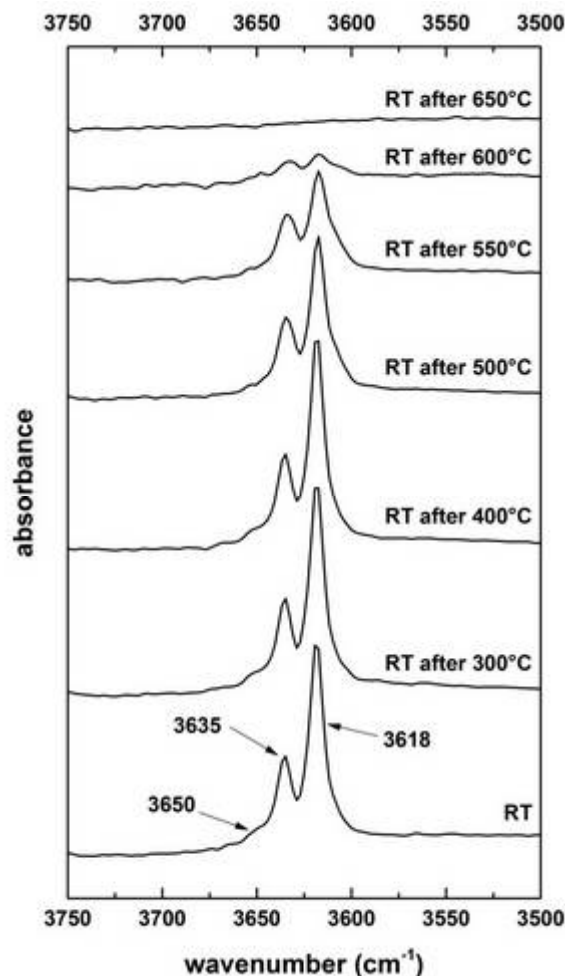


**Figure 5.6.** OH-stretching IR spectra at *RT* after fast quenching from target *T*. Experiments performed on a pure powder, not embedded in KBr pellet. Spectra plotted with the same absorbance scale.

Figure 5.7 displays the decomposition of the IR spectra shown in Figure 5.6. Concerning the unheated sample, as said in Chapter 4, the fitted bands are assigned respectively to the following local configurations at the *M*(1,3)-sites:  $\text{MgMgFe}^{2+}$  ( $3650\text{ cm}^{-1}$ );  $\text{MgFe}^{2+}\text{Fe}^{2+}$  ( $3635\text{ cm}^{-1}$ ); and  $\text{Fe}^{2+}\text{Fe}^{2+}\text{Fe}^{2+}$  ( $3618\text{ cm}^{-1}$ ). Note that all the components present in the untreated sample, are also present in the spectra obtained after heat-treatment up to  $550^\circ\text{C}$ . The spectrum collected after heat-treatment at  $600^\circ\text{C}$  shows no OH-bands.

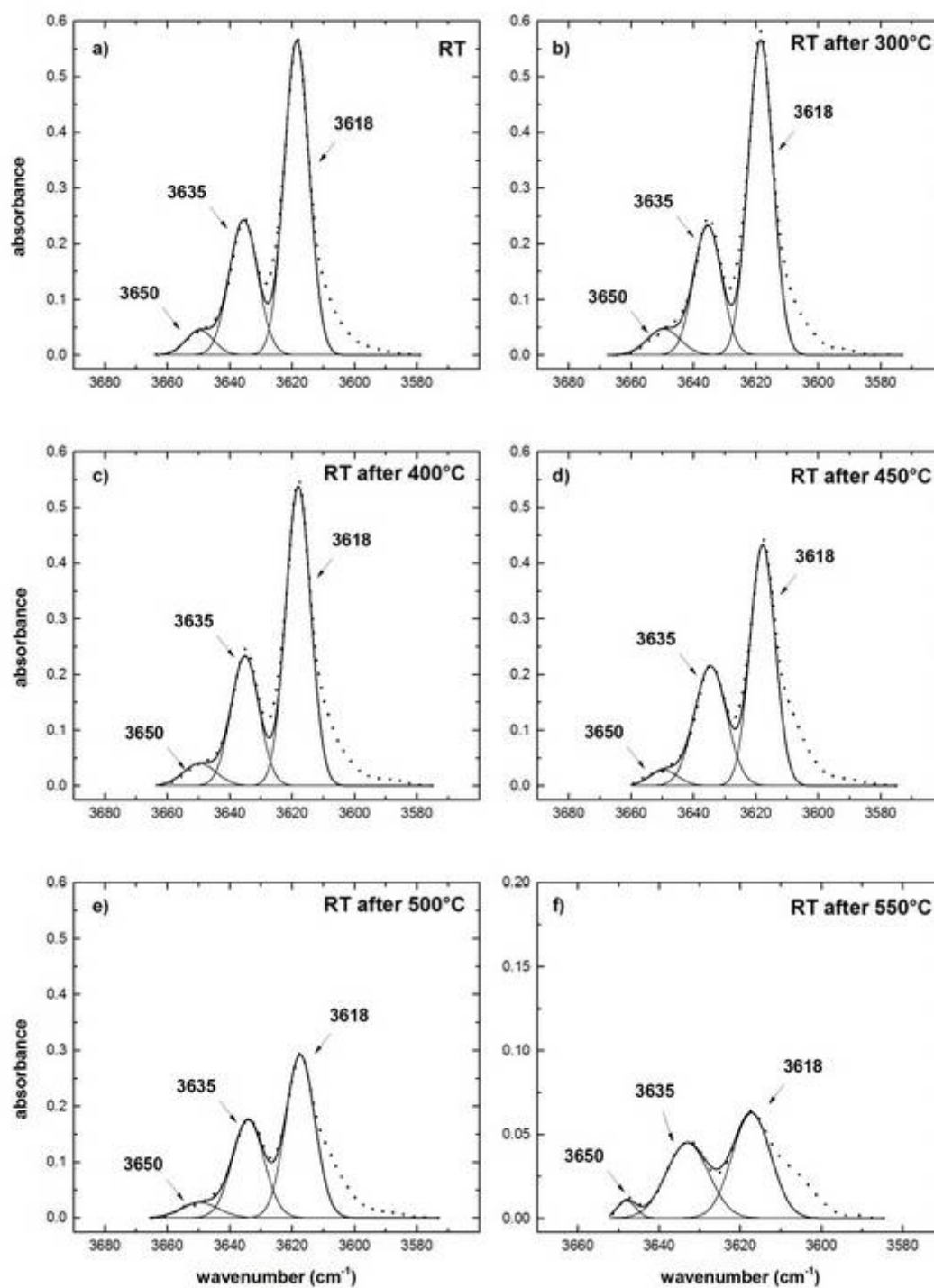


**Figure 5.7.** Decomposition of the IR spectra shown in Figure 5.6. The untreated sample is also shown for comparison.

Table 5.2 gives the numerical results of the fittings shown in Figure 5.7. The relative intensities of the single components virtually do not change up to 400°C.

	$\text{Fe}^{2+}\text{MgMg-OH-}\square$	$\text{Fe}^{2+}\text{Fe}^{2+}\text{Mg-OH-}\square$	$\text{Fe}^{2+}\text{Fe}^{2+}\text{Fe}^{2+}\text{-OH-}\square$
<b>RT</b>			
center ( $\text{cm}^{-1}$ ):	3650	3635	3618
FWHM:	10.17	10.36	8.95
area%:	6	31	63
<b>RT after 300°C</b>			
center ( $\text{cm}^{-1}$ ):	3650	3635	3618
FWHM:	12.11	10.13	8.95
area%:	7	29	64
<b>RT after 400°C</b>			
center ( $\text{cm}^{-1}$ ):	3650	3635	3618
FWHM:	12.13	10.13	8.95
area%:	6	31	63
<b>RT after 450°C</b>			
center ( $\text{cm}^{-1}$ ):	3650	3635	3618
FWHM:	10.37	11.77	8.95
area%:	4	38	58
<b>RT after 500°C</b>			
center ( $\text{cm}^{-1}$ ):	3650	3635	3618
FWHM:	13.71	11.54	10.60
area%:	7	37	56
<b>RT after 550°C</b>			
center ( $\text{cm}^{-1}$ ):	3649	3634	3618
FWHM:	4.71	12.01	10.83
area%:	4	42	54

**Table 5.2.** Results from the fittings of the IR spectra shown in Figure 5.7.

In Figure 5.8a the relative intensities of the single components are plotted against temperature. The component at  $3618\text{ cm}^{-1}$  ( $\text{Fe}^{2+}\text{Fe}^{2+}\text{Fe}^{2+}$  arrangement) shows a decrease in absorbance above 400°C, and as a consequence the relative intensity of the band at  $3635\text{ cm}^{-1}$  ( $\text{Fe}^{2+}\text{Fe}^{2+}\text{Mg}$  arrangement) increases. The intensity of the minor band at  $3650\text{ cm}^{-1}$  is constant. These trends suggest that deprotonation is preferentially associated with  $\text{Fe}^{2+}\text{Fe}^{2+}\text{Fe}^{2+}$  local configuration. In Figure 5.8b it can be seen how the absolute intensities of all the single components decrease with temperature.



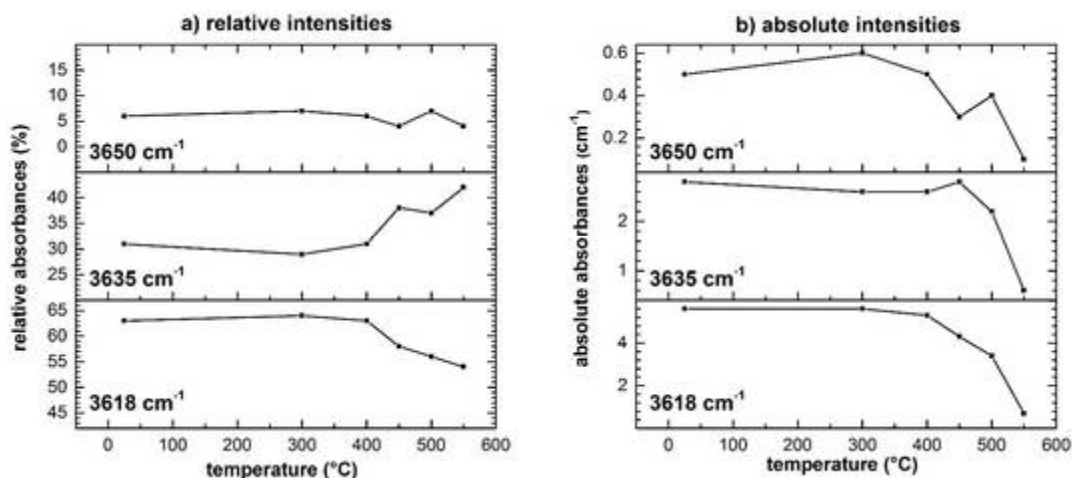


**Figure 5.8.** Evolution of absorbance for the single components in the same spectra of Fig. 5.7. a) Relative absorbances; b) absolute absorbances. Spectra collected after quenching.

### FTIR spectra collected *in situ*

The IR spectra collected *in situ* (Figure 5.9) show a general broadening of all peaks, which, coupled with their increase in height, produces a general increase of the total absorbance. Because of the above mentioned general band broadening, the three main components, well resolved in the spectrum of the untreated sample, are still recognizable up to 350°C, even though they appear less sharp and progressively shifted toward lower frequencies. At 500°C two main peaks at about 3625, and 3609 cm⁻¹, are visible. At 550°C the OH-stretching absorbance disappears.

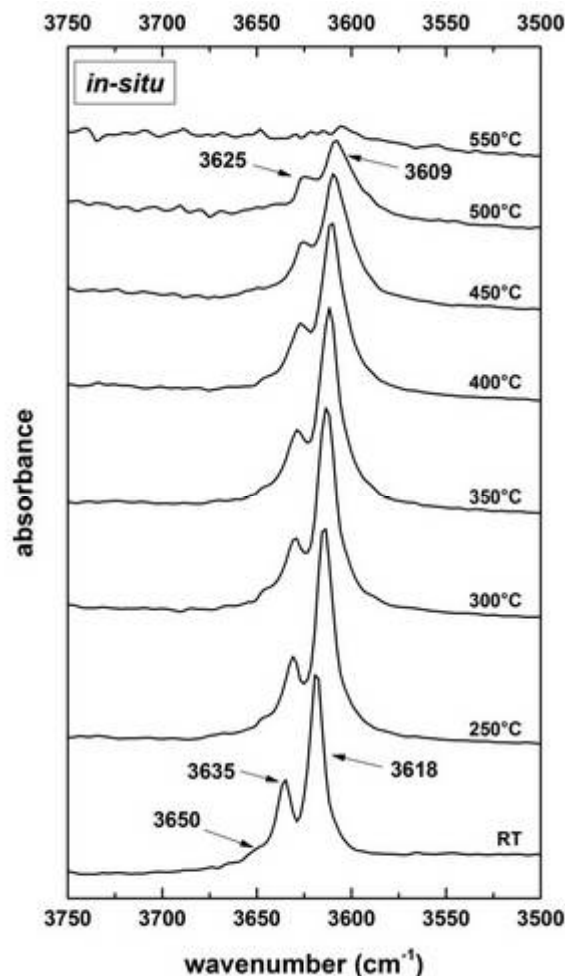


**Figure 5.9.** OH-stretching IR spectra measured *in situ* for increasing  $T$ . The experiments were performed on a pure powders. Spectra plotted with the same absorbance scale.

### The evolution of the OH-band intensity as a function of $T$

Figure 5.10 shows the evolution, as a function of temperature, of the OH-absorbance (integration range 3711-3560  $\text{cm}^{-1}$ ) measured *in situ* and at RT after quenching the pure powdered sample. Two different trends are observed: the data collected *in situ* (red dots) define a positive trend, with a total absorbance that at 350°C is about 40% more than the initial value measured on the untreated sample. For  $T > 550^\circ\text{C}$  the intensity drops to zero, and no OH-absorption is detected at 600°C. The absorbance collected after quenching on the other hand, is constant up to 400°C, and quickly decreases in the 400-600°C range (black dots).

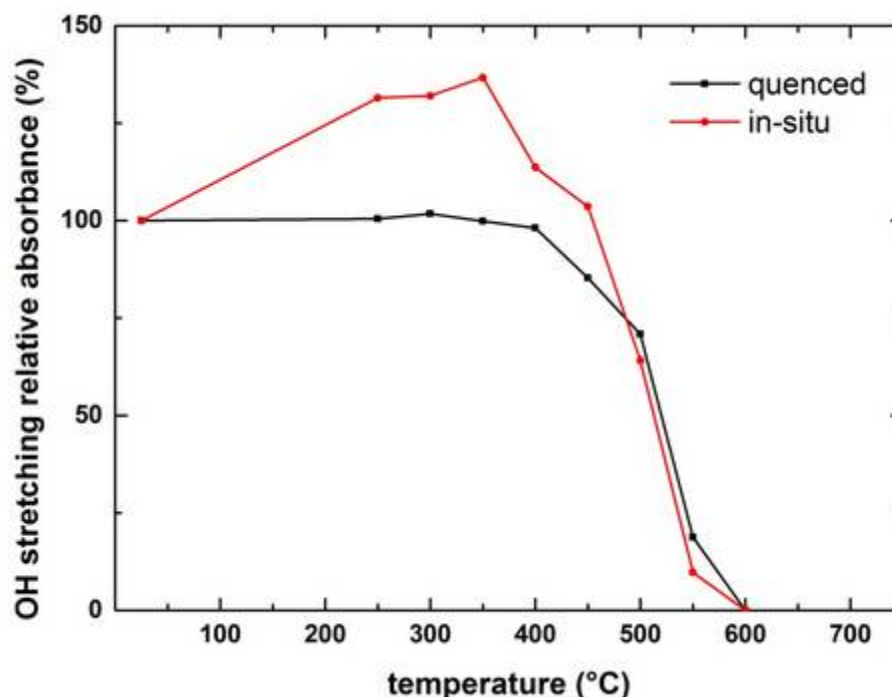


**Figure 5.10.** Comparison of the relative absorbance of the OH-stretching band measured in situ versus quenched samples as a function of  $T$ . Spectra collected on pure powdered samples; integration range  $3711\text{--}3560\text{ cm}^{-1}$ .

In this experiment an increase of the OH-band intensity for increasing temperatures is observed. As mentioned in Section 5.2, in all previous studies on several types of minerals, a decrease in the OH-intensity has been reported. Since the same heating rates were used for the single crystal, a comparison between these trends and the ones shown in Figure 5.5 can be done. With powders the increase of the absorbance measured *in situ* is less marked than with single crystal. In addition the decrease in intensity at higher temperatures is less abrupt. The important point here is that the drop in intensity occurs at  $550^{\circ}\text{C}$  for single crystals and just above  $400^{\circ}\text{C}$  for powders.

As a general comment, this observation can be in part explained with a larger external surface of the powdered sample exposed to atmospheric oxygen with respect to single crystals, which favors to the oxidation/deprotonation process. Furthermore, due to the small dimension of the grains, migration of

protons toward the external surface is much easier in powders, therefore a smaller amount of energy is necessary during deprotonation.

## **Chapter 6 HT-experiments on riebeckite from Malawi: X-ray diffraction and Mössbauer spectroscopy**

---

The HT-FTIR experiments on riebeckite from Malawi were completed with data obtained via other complementary analytical techniques. Single crystal X-ray refinements were performed at RT on heat-treated samples for studying any possible structural modification associated with deprotonation/oxidation. *In situ* HT X-ray powder diffraction data were collected to follow the evolution of unit cell parameters during deprotonation, while Mössbauer analysis was done on quenched powders for having a direct information on the Fe oxidation as a function of increasing temperature.

## **6.1. X-ray diffraction on heat-treated single crystals**

Two doubly-polished samples of riebeckite were heated and kept at 490°C for 145 minutes, and at 530°C for 45 minutes respectively. These  $T$  values and heating times were selected on the basis of the results from continuous ramp experiments (Chapter 5); 490°C is in fact just before, while 530°C is very close to the verge of the dehydration process. These measurements were intended to verify the role of the heating time on the oxidation process at critical  $T$  values. The residual OH-contents in the sample before and after the heat-treatment were determined by FTIR spectroscopy on the same fragments studied by single crystal X-ray Structure REFinement (SREF).

### **Experimental methods**

A fragment of riebeckite was doubly-polished down to a thickness of 157  $\mu\text{m}$  and then split into two chips. Non-polarized single crystal HT-FTIR spectra were collected at INFN (Frascati) using the same experimental set-up described in Section 5.1.

After the heating cycles and the FTIR data collection, the two sections were mounted on a Bruker-AXS CCD diffractometer at the Istituto di Geoscienze e Georisorse of CNR in Pavia and diffraction data were collected with graphite monochromatized  $\text{MoK}\alpha$  X-radiation ( $\lambda = 0.7107 \text{ \AA}$ ). Omega rotation frames (scan width  $0.3^\circ$ , scan time 20s, sample-to-detector distance 50 mm) were processed with the SAINT software (Bruker, 2003) and intensities were corrected for Lorentz and polarization effects; absorption effects were empirically evaluated by the SADABS software (Sheldrick, 1996) and an absorption correction was applied to the data. The collected reflections were reduced to unique reflections, and accurate unit cell dimensions were calculated by least-squares refinement of the positions of the independent reflections with  $I_o > 10 \sigma(I_o)$  in the  $\theta$  range  $2\text{-}30^\circ$ .

Only reflections with  $I_o > 3 \sigma(I_o)$  were considered as observed during unweighted full-matrix least-squares refinement on  $F$  done with a program written based on the ORFLS code to deal with complex solid-solutions (Cannillo *et al.*, 1983). Scattering curves for fully ionised chemical species were used at sites where chemical substitutions occur; neutral vs. ionised scattering curves were used at the  $T$  and anion sites. Details of this procedure are reported in Oberti *et al.* (1992) and in Hawthorne *et al.* (1995). The absence of residual electron density along the  $b$  direction at  $\sim 0.40$  Å from the  $M(4)$ -site (i.e., at the  $M(4')$ -site) testifies the absence of significant amounts of the smaller  $B$ -cations (e.g.,  $\text{Li}^+$ ,  $\text{Fe}^{2+}$ ,  $\text{Mg}^{2+}$ ).

Experimental details on the data collection and refinement parameters are given in Table 6.1, together with the crystal-chemical results useful for the discussion.

## Results

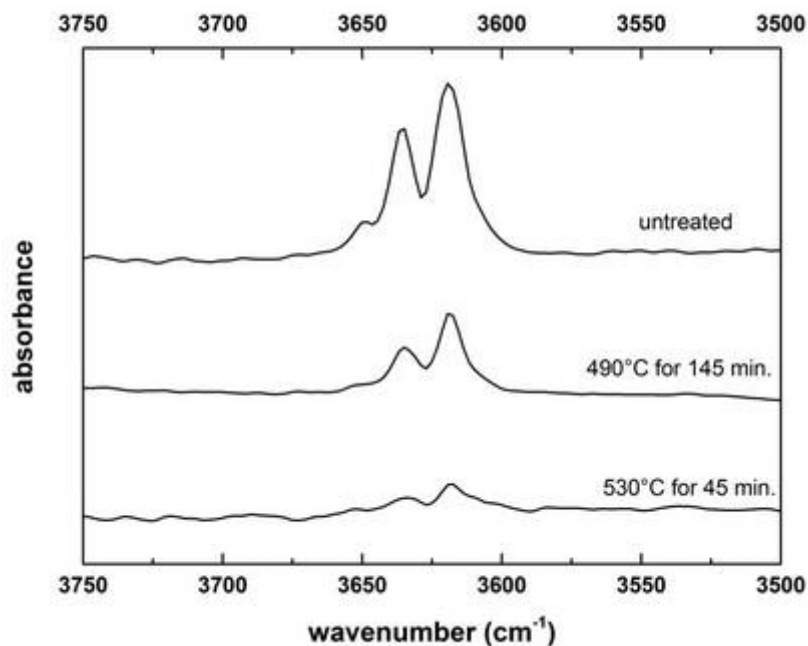
The SREF results for the two doubly-polished sections heated at 490°C for 145 minutes and at 530°C for 45 minutes are given in Table 6.1. The unit cell parameters, refined site scatterings, and selected geometric parameters, are shown for the unheated and for the partially deprotonated “oxo-amphiboles”.

Figure 6.1 shows the IR spectra collected at  $RT$  before and after the heat-treatment. The OH-stretching intensities integrated in the  $3680\text{--}3540\text{ cm}^{-1}$  range, are listed in Table 6.2.

Sample	RT	490°C for 145 min.	530°C for 45 min.
<i>a</i> (Å)	9.7464(3)	9.6567(7)	9.6448(5)
<i>b</i> (Å)	18.0463(6)	17.9653(12)	17.9424(9)
<i>c</i> (Å)	5.3328(2)	5.2987(5)	5.2937(3)
$\beta$ (°)	103.544(1)	103.493(1)	103.477(1)
<i>V</i> (Å <sup>3</sup> )	911.9	893.9	890.9
$\theta$ range (°)	2-35	2-30	2-30
# refl <sub>col</sub>	6820	5079	5067
# refl <sub>unique</sub>	2064	1354	1354
# refl <sub>obs</sub> ( $I > 3\sigma_I$ )	1878	1295	1257
$R_{int}$ %	1.8	1.4	1.4
$R_{obs}$ %	2.2	3.2	2.5
$R_{all}$ %	2.4	3.3	2.7
s.s. A (epfu)	1.10	5.80	7.00
s.s. B (epfu)	22.78	18.21	16.64
s.s. C (epfu)	127.65	127.39	127.62
s.s. Total (epfu)	151.53	151.40	151.26
< <i>T</i> (1)-O> (Å)	1.622	1.622	1.620
< <i>T</i> (2)-O> (Å)	1.630	1.626	1.629
< <i>M</i> (1)-O> (Å)	2.113	2.052	2.041
< <i>M</i> (2)-O> (Å)	2.028	2.037	2.039
< <i>M</i> (3)-O> (Å)	2.121	2.117	2.116
< <i>M</i> (4)-O> (Å)	2.536	2.550	2.556
< <i>A</i> -O> (Å)	-	2.899	2.887
< <i>A</i> ( <i>m</i> )-O> (Å)	2.862	2.798	2.785
<i>M</i> (1)- <i>M</i> (2) (Å)	3.146	3.215	3.223

**Table 6.1.** Unit cell parameters, refined site scatterings and selected geometric parameters for riebeckite (RT) and "oxo-riebekite" after isothermal heat-treatments at two different *T*. Cation-oxygen bond distances measured for the heat-treated samples have been corrected for riding motion (Busing and Levy, 1964).





**Figure 6.1.** IR spectra collected at RT before and after the heat-treatment. The X-ray refinement results on the same samples are given in Table 6.1.

Sample	Absolute absorbance before heat-treatment	Absolute absorbance after heat-treatment	Residual absorbance (%) after the heat- treatment
490°C-145 min.	5.3	2.9	55
530°C-45 min.	8.6	2.1	24

**Table 6.2.** Integrated absorbance in the 3680-3540  $\text{cm}^{-1}$  range, from the spectra collected before and after the heat-treatment.

## Discussion

Inspection of Table 6.1 shows that the unit cell parameters and the unit cell volume decrease for increasing  $T$ . The shortening of the unit cell parameter  $b$  can be explained considering the oxidation of  $\text{Fe}^{2+}$  into  $\text{Fe}^{3+}$  at the octahedral  $M(1,3)$ -sites, while a major contraction along the  $a^*$  direction is compatible with a loss of  $\text{H}^+$ . The slight shortening along the  $c$  dimension is congruent with an adjustment of the tetrahedral chain, due to the smaller ionic radius of  $\text{Fe}^{3+}$  (0.645 Å) in comparison with  $\text{Fe}^{2+}$  (0.78 Å). The observed bond distance  $\langle M(1)\text{-O} \rangle$  is 2.113 Å for the unheated sample, while being 2.052 and 2.041 Å for the samples treated at 490 and 530°C respectively. The observed  $\langle M(3)\text{-O} \rangle$  is 2.121 Å for the unheated sample, and decreases slightly to 2.117 and 2.116 Å for the samples treated at 490 and 530°C respectively. Considering that  $\text{Fe}^{2+}$  is equally distributed among the  $M(1)$  and  $M(3)$ -sites (Chapter 4), the significant decrease of the  $\langle M(1)\text{-O} \rangle$  distance indicates that the  $\text{Fe}^{2+}$  to  $\text{Fe}^{3+}$  oxidation occurs almost entirely at the  $M(1)$ -site.

Oberti *et al.* (2007), showed that the  $\langle M(1)\text{-}M(2) \rangle$  distance is linearly correlated to the amount of deprotonated O(3)-sites (“oxo-component”) within the amphibole structure. In our experiments, the  $\langle M(1)\text{-}M(2) \rangle$  distance increases from 3.146 Å for the unheated sample, to 3.215 and 3.223 Å for the samples treated at 490 and 530°C respectively. Based on the regression equation calibrated on pargasite (Oberti *et al.*, 2007), the  $\langle M(1)\text{-}M(2) \rangle$  distances measured for the studied riebeckites imply oxo-components of 1.28 and 1.43, for the samples heated at 490 and 530°C, respectively, in agreement with the IR data given in Table 6.2.

Site scattering values at A-site increase from 1.10 epfu for the untreated crystal to 5.80 and 7.00 epfu for the samples heated at 490 and 530°C respectively, while site scattering at B-sites decrease from 22.78 to 18.21 and 16.64 epfu respectively. The total site scattering values, as well as those at the C-sites, remain virtually constant. This observations thus suggests a migration of cations from  $M(4)$  to A. Similar results were obtained from an heat-treated metamorphic riebeckite, where structure refinements showed an evident loss in hydrogen, a consequent  $\text{Fe}^{2+}$  oxidation within the octahedral sites, and a migration of Na from  $M(4)$ -sites toward the previously empty A-site (Ungaretti *et al.*, 1978 and Ungaretti, 1980).

According to these studies, the oxidation of ferrous iron determined an excess of positive charge on some of the oxygens belonging to the  $M(1)$  and  $M(3)$  octahedra. The cation migration towards the previously empty  $A$ -site, along with significant variations of some bond distances within the octahedra, were hence explained as a processes dictated by bond-valence requirements (Ungaretti, 1980).

According to a vast literature (e.g. Hawthorne and Della Ventura, 2007) an increasing occupancy of the  $A$ -site, should be translated into the appearance of additional bands in the IR spectra collected on the heat-treated samples, but this is not the case (Figure 6.1). The lack of such new bands can however be explained by considering that from bond-valence considerations the occupied  $A$ -sites must be locally associated with the deprotonated O3 sites, making the configuration invisible to O-H stretching spectroscopy. For a similar reason, also the new configurations with  $\text{Fe}^{3+}$  at  $M(1)$  and  $M(3)$ , which develop locally associated with H-loss, are not detected by IR.

The decrease of  $\beta$  from  $103.544^\circ$  to  $103.493^\circ$  (Table 6.1) is also compatible with a migration of cations from  $B$  to  $A$ . Finally, the decrease of the observed  $\langle A-O \rangle$  bond distance from 2.899 for the crystal heated at  $490^\circ\text{C}$ , to 2.887 Å for the one treated at  $530^\circ\text{C}$ , suggests a cation disordering within the  $A$ -site cavity as a function of heating.

## 6.2. *In situ* powder diffraction

### Experimental methods

High-temperature X-ray powder diffraction (XPRD) patterns were collected at the Geology Department of the University of Bari, with an Empyrean PANalytical diffractometer operating in Bragg-Brentano geometry, and equipped with a high temperature (HT) cell (model HTK 1200N, Anton Paar) using Ni filter and a PIXcel linear detector (CuK $\alpha$  radiation). The data were collected in the angular range 8-75° (2 $\theta$ ) with steps of 0.013°. The sample was heated from RT to 800°C and then cooled back to RT always using a 10°C/min rate. A spectrum was collected at RT, 100, 200°C, every 25°C from 250 to 500°C, at 550, 600, 700 and 800°C. A spectrum was also collected every 100°C during cooling. The entire data collection lasted ~ 35 hours.

### Results

This experiment was carried out with the aim of measuring the evolution *in situ* of cell parameters with temperature. Figure 6.2 displays the X-ray patterns as a function of increasing  $T$ . In the  $T$  range RT to 400°C the positions of the diffraction peaks change gradually as a consequence of heating. Between 425 and 450°C there is an abrupt change in the patterns: the (201) and (310) diffraction peaks are in fact suddenly displaced toward higher  $2\theta$  values. Such shift is compatible with a contraction of the unit cell parameters within the 425-450°C temperature range.

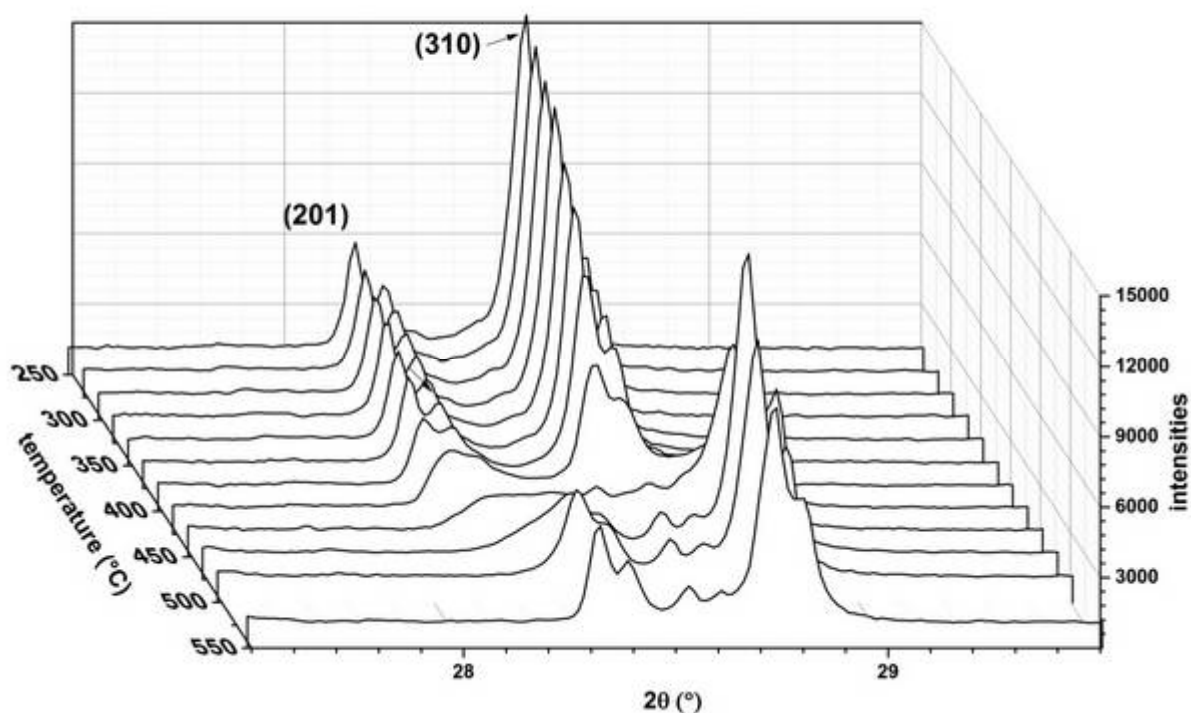


**Figure 6.2.** X-ray powder diffraction patterns for increasing  $T$ .

The unit cell dimensions of riebeckite as a function of increasing  $T$  were refined (Le Bail method), using a General Structure Analysis System (Larson *et al.*, 2000) software; final data are given in Figure 6.3. During the heating cycle (red points) the gradual increase in all the cell dimensions up to 425°C can be explained with the thermal expansion of the structure. From 425 to 450°C, there is a significant contraction with a drop for all parameters. Above 450°C the structure keep expanding, with the same slope observed in the first part of the experiment. During the cooling cycle (blue points in Figure 6.3) the structure linearly shrinks.

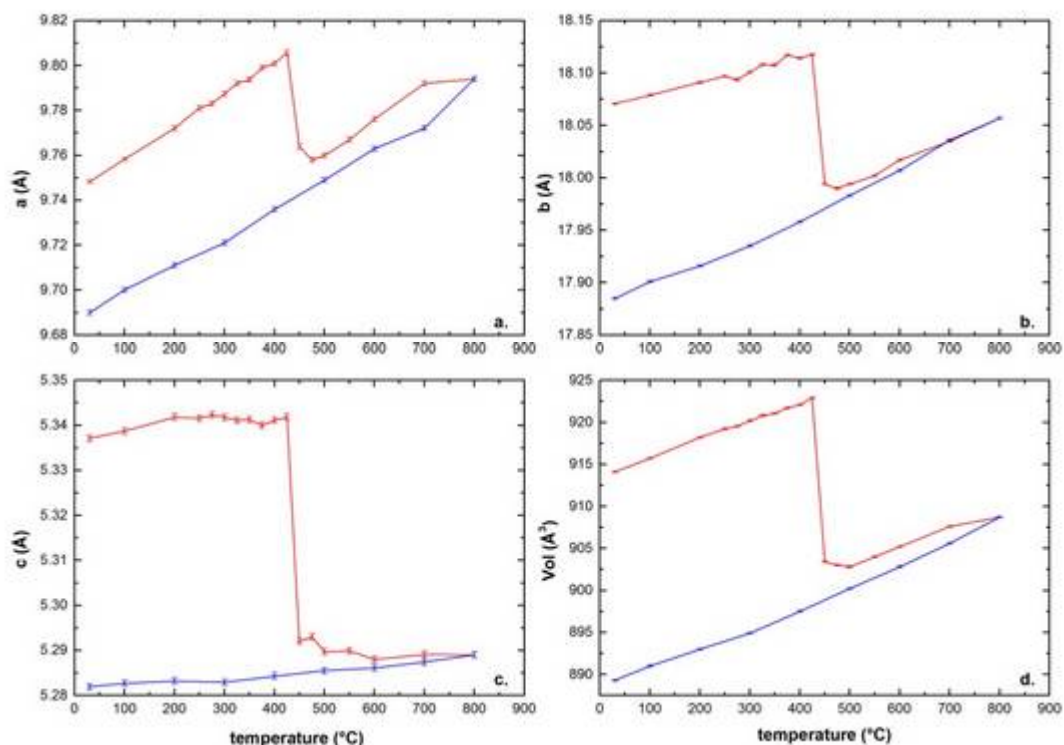


**Figure 6.3.** Variation of the unit cell dimensions as a function of temperature. Red points: heating cycle; blue points: cooling cycle. The standard deviation associated to each point is shown.

## Discussion

Figure 6.4 displays a comparison between the powder HT-FTIR and the HT-XRPD results obtained for the studied riebeckite. Both techniques yield data evolutions characterized by substantial changes above 425-450 °C. The slower decrease of the OH-stretching signal in comparison to the sharp drop in unit cell volume, is not completely clear. One reason could be connected with the difference in the duration of the experiments; each IR measurement is in fact completed in less than one minute, whereas the diffraction experiments required more than half an hour for each step, however other factors could be taken into account, i.e. a different rate in the structure adjustments sampled by the two different techniques.

Combination of the IR and X-ray results point to a loss of protons accompanied by the oxidation of Fe resulting into a sudden contraction of the unit cell. This scenario is in agreement with the data given in Chapter 4 describing the HT behavior of a synthetic potassic-ferro-richterite and with the results of several previous works (e.g. Addison *et al.*, 1962a; Ungaretti, 1980), where X-ray powder patterns of oxidized Fe-bearing amphiboles showed a contraction in unit cell dimensions.

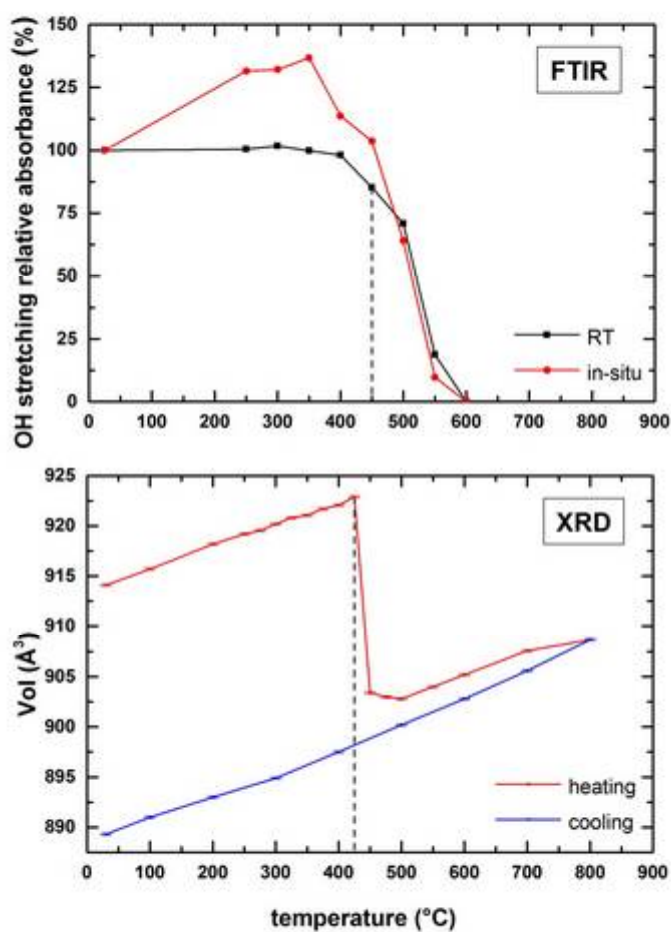


**Figure 6.4.** Comparison between HT X-ray diffraction and HT-FTIR OH results for the studied riebeckite.

### 6.3. Mössbauer spectroscopy on quenched powders

A direct measure of the changes in the oxidation state of iron induced by temperature is crucial in the understanding of the deprotonation/oxidation mechanisms. This information can be provided by Mössbauer spectra that are sensitive to the oxidation state, electronic configuration, coordination number and site symmetry around Fe (Bancroft, Burns and Maddock, 1967; Bancroft and Burns, 1969). In addition, assuming that the recoil-free fractions are the same for  $\text{Fe}^{2+}$  and  $\text{Fe}^{3+}$ , the areas under the peaks in the spectra can be used to extract quantitative information regarding not only the  $\text{Fe}^{2+}/\text{Fe}^{3+}$  ratio, but also the distribution of these two nuclei among the different structural sites.

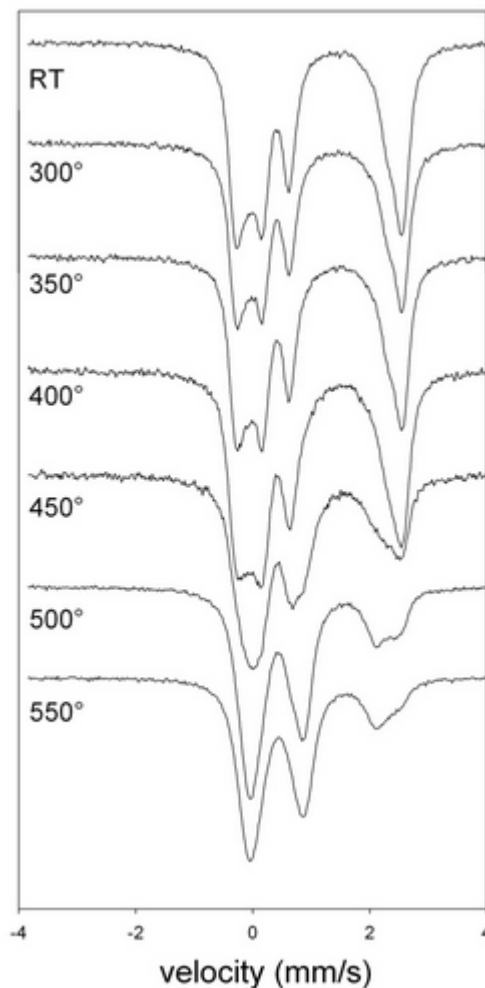
#### Experimental methods

A crystal of riebeckite was ground into a fine and homogeneous powder that was used for seven distinct experiments. The first one consisted in collecting a Mössbauer spectrum of the untreated sample, and the results were discussed in Section 4.1. The remaining powder was used for six different heating experiments. In each of these, about 5 mg of sample were kept, for three hours, at 300, 350, 400, 450, 500 and 550°C respectively. The aim was to study the effect of increasing temperature on the powder, and hence to analyze more and more intensely oxidized samples. After the heat-treatment, the powder was quenched and the Mössbauer spectrum was collected at room  $T$ . The set-up used is the same as that described in Section 4.1. The data evaluation of the spectra was done (see Section 4.1) with the program RECOIL (Rancourt & Ping 1991; Rancourt *et al.*, 1993; Rancourt *et al.* 1996), using classical full static Hamiltonian approach with Lorentzian shaped doublets.



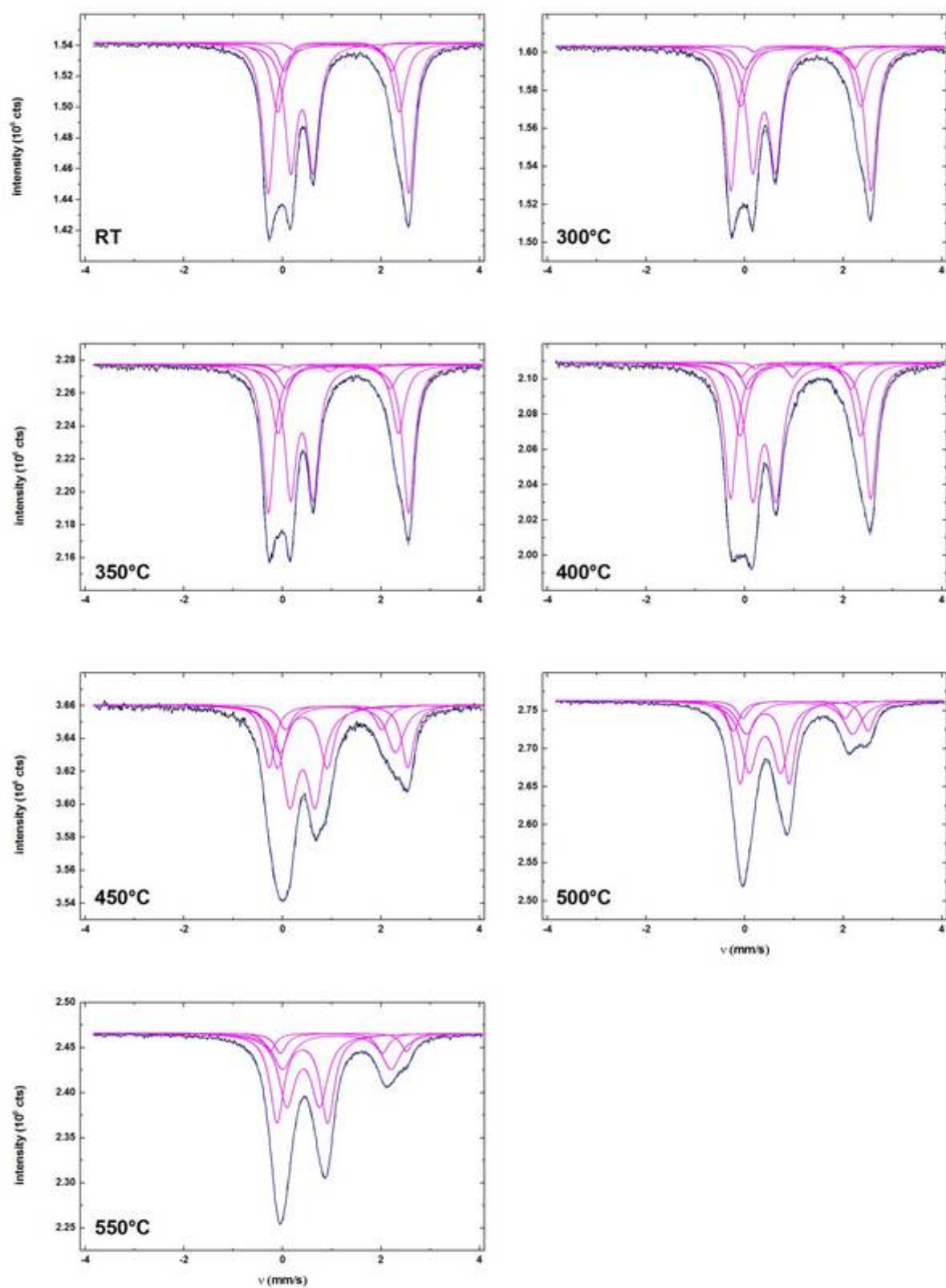
## Results

Figure 6.5 shows that there is a significant evolution of the Mössbauer spectra as a function of  $T$ .



**Figure 6.5.** Mössbauer spectra collected at RT on the untreated powder and on samples quenched after heat-treatments at the indicated temperatures for three hours.

The data were interpreted based on the model derived from the untreated sample and checked against the X-ray diffraction data. The fitted spectra are shown in Figure 6.6.



**Figure 6.6.** Fitted Mössbauer spectra collected on the untreated sample, and on the heat-treated samples. The treated samples were heated at: 300, 350, 400, 450, 500 and 550°C.

From Figure 6.6 it is evident, that up to 300°C there are no significant changes in the spectra. At 350°C a second  $\text{Fe}^{3+}$  component with a larger quadrupole splitting appears, indicating the initial stage of some oxidation process. In order to avoid large correlation of parameters, the area fraction of  $\text{Fe}^{3+}$  at  $M(2)$  was fixed, in preliminary stages of refinement, to the value obtained at RT, and was kept fixed during the model building. In the final cycles, also the area fraction of  $\text{Fe}^{3+}$  at  $M(2)$  was allowed to vary freely, so at convergence that there were no parameter constrained. Careful inspection of Figure 6.6. shows that the new  $\text{Fe}^{3+}$  doublet gains in intensity with increasing temperature, while the intensity of the  $\text{Fe}^{2+}$  at  $M(1)$  doublet distinctly decreases. Interestingly the content of  $\text{Fe}^{2+}$  at the  $M(3)$  and  $M(2)$ -sites remains constant, within experimental resolution. The site population of  $\text{Fe}^{3+}$  at  $M(2)$  also remains constant.

Significant changes occur in the hyperfine parameters as oxidation proceeds, both for the isomer shift as well as for the quadrupole splitting, in all fitted components. The isomer shifts of the  $\text{Fe}^{2+}$ - $M(1)$  and  $M(3)$  components decrease with increasing annealing temperature (Figure 6.7), and hence with increasing amount of oxidation. The quadrupole splitting values associated to the same components also decrease, especially above 400°C. It is known (e.g. Hawthorne, 1983) that the QS of  $\text{Fe}^{2+}$  is inversely correlated with the geometric/electronic distortion of the octahedral sites. Thus the decrease observed in Figure 6.7 is consistent with an increasing electronic/geometric distortion of the local environment around the  $\text{Fe}^{2+}$  probe nucleus as a function of  $T$ .

For the  $\text{Fe}^{3+}$ - $M(2)$  component both the isomer shift and the quadrupole splitting values increase with increasing oxidation (Figure 6.8). Because  $\text{Fe}^{3+}$  quadrupole splitting and geometric/electronic distortions from ideal octahedral symmetry are known to be positively correlated, the plots of Figure 6.8 again suggest an increase of the local distortion around the  $M(2)$ - $\text{Fe}^{3+}$  probe nucleus for increasing  $T$ .

The second additional  $\text{Fe}^{3+}$  component has a larger QS with respect the  $M(2)$ - $\text{Fe}^{3+}$  doublet, and this suggests an even more distorted local oxygen coordination. Since the significant decrease of the  $\langle M(1)\text{-O} \rangle$  bond distances (Table 6.1) yielded by the structural data were interpreted with an  $\text{Fe}^{2+}$  to  $\text{Fe}^{3+}$  oxidation occurring almost entirely at the  $M(1)$ -site, the additional Mössbauer component is assigned to  $\text{Fe}^{3+}$  at  $M(1)$ .

The site distribution parameters along with the final assignment derived from the fitting are listed in Table 6.3.

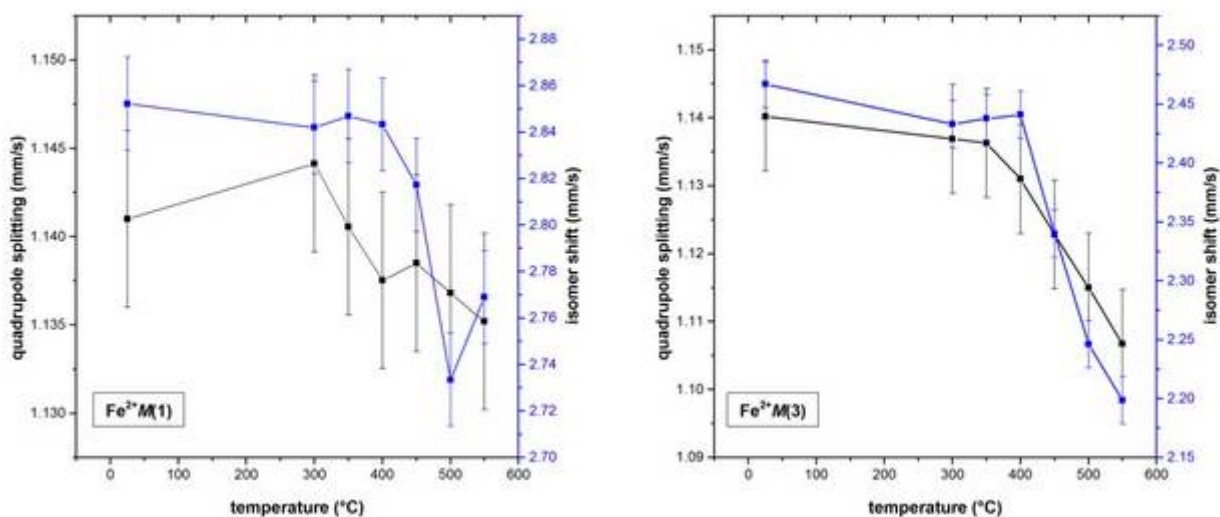


**Figure 6.7.** Evolution of the quadrupole splitting (black) and isomer shift (blue) as a function of temperature for the  $\text{Fe}^{2+}$  at  $M(1)$  (left) and  $\text{Fe}^{2+}$  at  $M(3)$  (right) components.

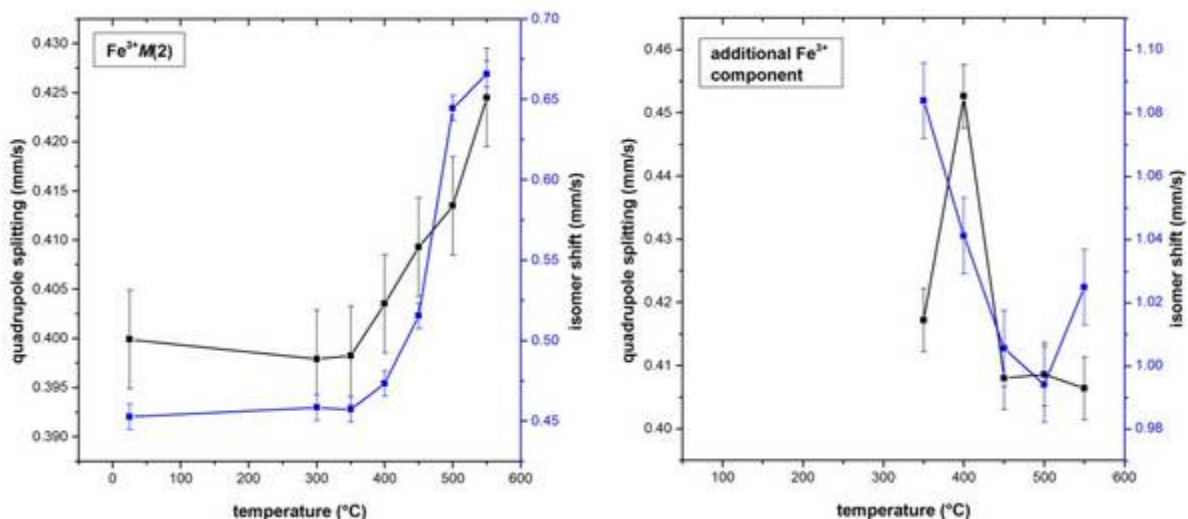


**Figure 6.8.** Evolution of the quadrupole splitting (black) and isomer shift (blue) as a function of temperature for the  $\text{Fe}^{3+}$  at  $M(2)$  component (left) and for the additional  $\text{Fe}^{3+}$  component (right).

	$\text{Fe}^{2+} M(1)$			$\text{Fe}^{2+} M(3)$			$\text{Fe}^{2+} M(2)$		
Temperature (°C)	IS (mm/s)	QS (mm/s)	HWHM (mm/s)	IS (mm/s)	QS (mm/s)	HWHM (mm/s)	IS (mm/s)	QS (mm/s)	HWHM (mm/s)
25	1.141	2.852	0.137	1.140	2.467	0.156	1.129	2.180	0.138
300	1.144	2.842	0.140	1.137	2.433	0.171	1.114	2.213	0.165
350	1.141	2.847	0.141	1.136	2.438	0.152	1.129	2.114	0.162
400	1.138	2.843	0.146	1.131	2.441	0.166	1.110	2.092	0.158
450	1.139	2.817	0.147	1.123	2.340	0.204	1.042	1.950	0.160
500	1.137	2.734	0.150	1.115	2.246	0.224	1.000	2.075	0.146
550	1.135	2.769	0.129	1.107	2.199	0.231	0.996	2.069	0.149
St. Dev.	0.005	0.020	0.005	0.008	0.020	0.005	0.005	0.020	0.005
	$\text{Fe}^{3+} M(2)$			$\text{Fe}^{2+} M(4)$			$\text{Fe}^{3+} M(1)$		
Temperature (°C)	IS (mm/s)	QS (mm/s)	HWHM (mm/s)	IS (mm/s)	QS (mm/s)	HWHM (mm/s)	IS (mm/s)	QS (mm/s)	HWHM (mm/s)
25	0.400	0.453	0.139	1.074	1.737	0.106			
300	0.398	0.458	0.143	1.058	1.732	0.099			
350	0.398	0.457	0.139	1.055	1.697	0.100	0.417	1.084	0.144
400	0.404	0.473	0.163				0.453	1.041	0.126
450	0.409	0.516	0.189				0.408	1.006	0.170
500	0.414	0.645	0.193				0.409	0.994	0.148
550	0.425	0.666	0.198				0.406	1.025	0.168
Mean									
St. Dev.	0.005	0.008	0.005	0.005	0.020	0.005	0.005	0.012	0.005

**Table 6.3.** Spectral parameters resulting from the fitting of the Mössbauer spectra shown in Figures 6.6.

## Discussion

The  $\text{Fe}^{2+}$  and  $\text{Fe}^{3+}$  site distributions obtained via Mössbauer spectroscopy for increasing temperatures are listed in Table 6.4.

Temperature (°C)	$\text{Fe}^{2+}$ <i>M</i> (1) (%)	$\text{Fe}^{2+}$ <i>M</i> (3) (%)	$\text{Fe}^{2+}$ <i>M</i> (2) (%)	$\text{Fe}^{3+}$ <i>M</i> (2) (%)	$\text{Fe}^{2+}$ <i>M</i> (4) (%)	$\text{Fe}^{3+}$ <i>M</i> (1) (%)
25	39.0	20.4	7.3	31.9	1.4	0.0
300	39.1	19.9	7.2	32.6	1.2	0.0
350	37.5	19.8	7.2	32.6	1.0	1.9
400	33.4	20.5	7.0	34.8	1.1	3.1
450	18.1	19.0	7.8	34.4	0.0	20.7
500	11.5	18.8	6.5	32.8	0.0	30.4
550	5.6	19.7	7.1	32.5	0.0	35.2
Mean St. Dev	1	1	1	1	1	1

**Table 6.4.** Mössbauer site distributions, expressed in % with respect to the total iron, derived from the fittings shown in Figure 6.6.

A graphic representation of the data listed in Table 6.4 for the  $\text{Fe}^{2+}$  at *M*(1,2,3)-sites and for the  $\text{Fe}^{3+}$  at *M*(1)-sites, is shown in Figure 6.9. According to these results, in this experimental condition, the oxidation of  $\text{Fe}^{2+}$  into  $\text{Fe}^{3+}$  is mainly localized at the *M*(1)-sites. Noticeably the decrease in  $\text{Fe}^{2+}$  corresponds to the increase of  $\text{Fe}^{3+}$  at the *M*(1)-sites. An iron oxidation mainly localized at the *M*(1)-sites is in agreement with the results yielded by SREF performed on heat-treated crystals and discussed in Section 6.1. As can be seen from Figure 6.9,  $\text{Fe}^{2+}$  at *M*(2,3)-sites seems not to be involved in the oxidation process even after three hours at 550°C.

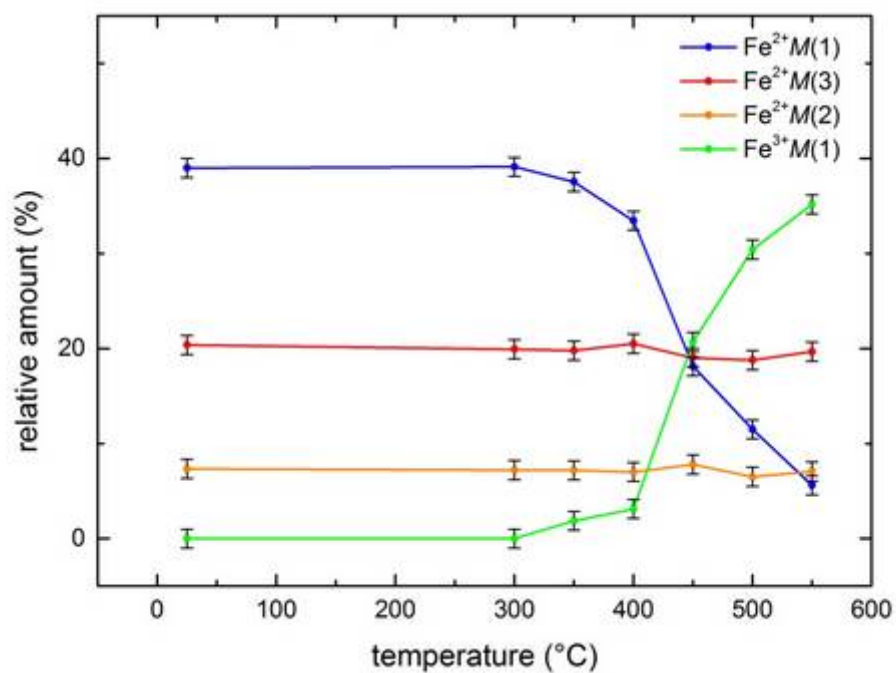


**Figure 6.9.** Evolution of the relative amounts of Fe<sup>2+</sup> at *M*(1,2,3)-sites and of Fe<sup>3+</sup> at *M*(1)-sites as a function of temperature obtained from Mössbauer spectroscopy.

## **Chapter 7    HT-FTIR isothermal experiments and kinetics of deprotonation on riebeckite**

---

The heating ramp experiments described in Chapter 5 had the purpose of characterizing the behavior of the amphibole, in this case the dehydration behavior, as a function of increasing  $T$ , and determine the transition temperature above which the protons are lost by the crystal. However, the continuous ramps do not provide information on the kinetics of the dehydration process. To this purpose, isothermal experiments were carried out, heating the sample at a target  $T$  and collecting the spectra as a function of time, for constant temperature. The  $T$  values were chosen on the verge of the transition, determined on the basis of the results of the heating ramp experiments.



## 7.1. Isothermal FTIR experiments on single crystals

The results presented in this section were obtained using several fragments of riebeckite from the same doubly-polished crystal. The room- $T$  features (crystal structure, crystal-chemistry and spectroscopy) of this sample are widely described in Chapter 4.

Non-polarized single crystal *HT*-FTIR spectra were collected at INFN (Frascati) using the same experimental set-up described in Section 5.1.

### Evolution of the OH-band intensity as a function of time

Three fragments obtained from the same 111  $\mu\text{m}$ -thick chip were used to perform three distinct isothermal experiments at 500, 520, 540°C respectively. In each case the target temperature was reached as quickly as possible, with a rate of 90°C/min, and then held constant. An IR spectrum was collected every 5 minutes until the OH-stretching band was visible, or, alternatively, the signal-to-noise ratio was still reasonable. It is worth mentioning that because the three fragments were obtained by breaking up the same doubly-polished chip, the studied sections share, within experimental errors, the same thickness and crystallographic orientation. This point is extremely important to consider for the interpretation of the results. It was impossible, anyway, to get three samples with the same lateral dimension, because of the strong tendency of the amphibole chip to split along prismatic cleavage planes. The studied fragments have however a width spanning from 500 to 300  $\mu\text{m}$  thus their lateral dimension can be considered relatively large compared to the thickness.

Figure 7.1 displays the spectra collected after 1, 25, 50 and 100 minutes at 540°C, respectively. As already discussed (Chapter 5), the spectra *in situ* at *HT* show a shift in the positions of the OH-stretching bands; this shift is already visible after one minute at 540°C and for longer durations all peaks keep the same frequency throughout the entire isothermal experiment (Fig. 7.1). The spectrum collected after one minute at 540°C features a considerable broadening in the OH-stretching band if compared with the untreated sample, the three components previously described at *RT* are no longer resolved, and the overall band shows a rounded profile.

After 25 minutes at 540°C the band clearly increases in (linear) intensity, while maintaining the same profile. After 50 minutes, an overall reduction in intensity is observed together with a change in its profile; at least two components, at around 3627 and 3610  $\text{cm}^{-1}$  respectively, can be now resolved. The 50 minutes spectrum is indeed similar in shape to the RT spectrum, even though all peaks are shifted toward lower frequencies by 7-8  $\text{cm}^{-1}$ . From 50 to 100 minutes at 540°C there is a strong decrease in intensity of the OH-absorption (Figure 7.1); the higher-frequency component at 3627  $\text{cm}^{-1}$  disappears while the 3610  $\text{cm}^{-1}$  components is still present.

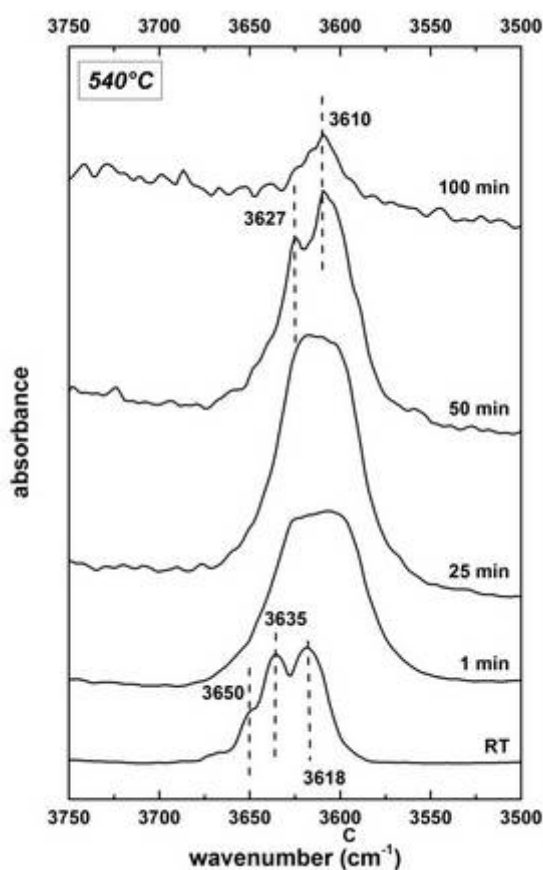


**Figure 7.1.** *In situ* OH-stretching spectra collected at 540°C after different heating time (indicated). Doubly-polished 111  $\mu\text{m}$ -thick section. The spectrum at RT is shown for comparison. Spectra plotted with the same absorbance scale.

Figure 7.2 shows the evolution of the integrated OH-stretching absorbance (total area, integration range  $3711\text{--}3560\text{ cm}^{-1}$ ) as a function of time, for the three isothermal experiments described above. It can be noticed how all patterns are characterized by an initial increase in absorbance of the OH-stretching intensity, and how this trend is inverted for increasing heating time. At  $T = 540^\circ\text{C}$  the maximum intensity is reached after 25 minutes, and a 35% gain of absorbance is observed compared to the value measured after one minute. It is important to note that a significant absorbance increase had already been observed in the spectra collected *in situ* during the heating ramps (Chapter 5), however the increase observed here is considerably lower (35% against almost 200% of gain) than that at  $550^\circ\text{C}$  during the heating ramp (see Figure 5.5). The intriguing point in the spectra of Figure 7.2 is that if the increase in absorbance at high temperature in the heating ramp experiments could be explained by a change in the molar absorptivity ( $\epsilon$ ) with  $T$ , the same cannot be said for the increase observed in Figure 7.2 because the temperature is constant in these experiments.

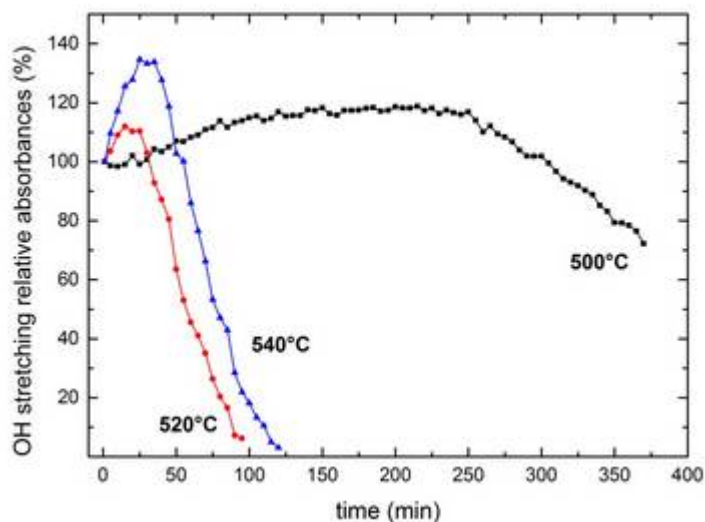


**Figure 7.2.** OH-stretching band absorbance as a function of time, for constant  $T$ ;  $111\text{ }\mu\text{m}$ -thick doubly-polished sections. Intensity determined by integrating the  $3711\text{--}3560\text{ cm}^{-1}$  range.

The experiment at 500°C, had to be stopped beyond 350 minutes because of a marked deterioration in the signal to noise ratio; thus in this case it was impossible to follow the deprotonation to its completion.

It is worth noting that apparently, looking at the trends in Figure 7.2, deprotonation seems to be quicker at 520 than at 540°C. This inconsistency can be explained considering that the fragments used for the 520°C data collection probably fractured during the preparation, thus slightly speeding up the process.

### Isothermal HT-FTIR experiments in controlled atmosphere

Figure 7.3 shows the evolution of the OH-stretching absorbance as a function of time for three isothermal experiments done at 520°C under different atmosphere. Three fragments of the same randomly oriented and doubly-polished, 133  $\mu\text{m}$  thick chip, were analyzed. The three sections were treated with different conditions within the heating stage. In one case (black triangles in Figure 7.3) a flux of 5 l/min  $\text{N}_2$  was pumped within the stage during the data collection. As it can be seen, the absorbance initially increases by about 40%, then it starts to decrease after 100 minutes. After 230 minutes, the loss in OH-absorbance is less than 25%, suggesting that a reducing atmosphere strongly inhibits the deprotonation process, in agreement with the studies of Addison *et al.* (1962a). In a second experiment (blue squares in Figure 7.3) no flux was used, and in fact the pattern is similar to the one shown at the same temperature in Figure 7.2. The red data are relative to the third experiment done by using a 5 l/m air flux; the trend is very similar to the one obtained without any air flux. After 40 minutes, however, it was no more possible to measure any OH-stretching absorbance, because of a decrease in the intensity of the signal transmitted by the sample.

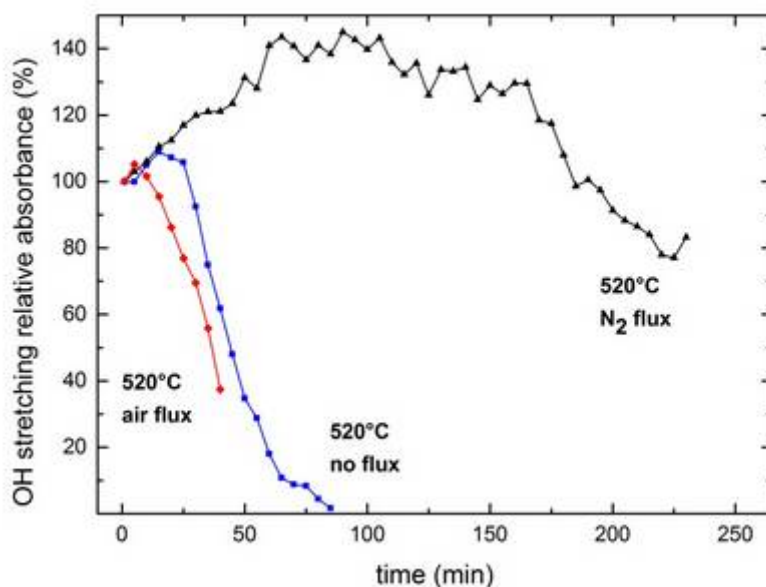


**Figure 7.3.** Evolution of the OH-stretching absorbance as a function of time at the constant  $T = 520^\circ\text{C}$  for different atmosphere conditions within the heating stage. Experiments performed on three fragments of the same doubly-polished 133  $\mu\text{m}$ -thick section.

## **7.2. FTIR-FPA imaging on quenched single crystal**

To try getting a further insight into the deprotonation mechanism, we collected FPA (Focal Planar Array) bi-dimensional IR images of the studied crystal during the isothermal experiment at 520°C. A focal-planar-array of detectors is similar to a CCD detector, and is constituted by a large number of small detectors (pixels) that collect simultaneously a large number (in our case 64 x 64) of IR spectra. By integrating the signal of the target absorber (in our case the O-H group) it is possible to obtain its distribution over the scanned area. According to our knowledge, this kind of detectors has never been used previously in heating experiments of amphiboles, thus our goal was to see if using this technique we could detect any spatial change in the local behavior of the OH-stretching signal during heating as a function of time. The obtained results are described below.

FTIR images were collected using a Linkam 1400XY heating stage fitted on a Bruker Hyperion 3000 FTIR microscope, equipped with a 20x Schwarzschild objective and a 64 x 64 pixel FPA. The microscope was attached to a Vertex optical bench with a KBr beamsplitter and a globar IR source. The nominal resolution was set at 4 cm<sup>-1</sup> and 16 scans were averaged for each spectrum. A 4 x 4 binning was used to reduce the acquisition time and obtain a better signal-to-noise ratio. With this set-up each frame covers an area of 128 µm x 128 µm with a nominal spatial resolution of ~8 µm; the entire image is made up of a 2 x 9 array of frames. The absorbances were calculated by integrating the 3693-3560 cm<sup>-1</sup> wavenumber range.

## IR-FPA imaging of the OH-band intensity on heat-treated crystal

For this experiments, a doubly-polished 136  $\mu\text{m}$ -thick section of riebeckite was prepared. The studied crystal (see optical image on the left) was prismatic and strongly unequant, almost one mm long and 100  $\mu\text{m}$  wide; it has been selected to study the dehydration behavior of a strongly anisotropic shape, and check if there was any preferential direction for the dehydration speed along, or perpendicular, the crystal elongation parallel to the *c* crystallographic direction. The images obtained during the isothermal experiment are shown in Fig 7.4; the chromatic scale representing the absorbance scale is given on the right. The sample was heated quickly (90°C/min rate) at 520°C and kept at this temperature for the amount of time indicated on each image, than was quenched quickly and the image was collected. The procedure was repeated again with the same conditions; the cumulative time of heating is indicated on each image. The results show that there is a regular decrease in OH-absorbance with time, without, apparently, any definitive preference for the OH diffusion in any direction.

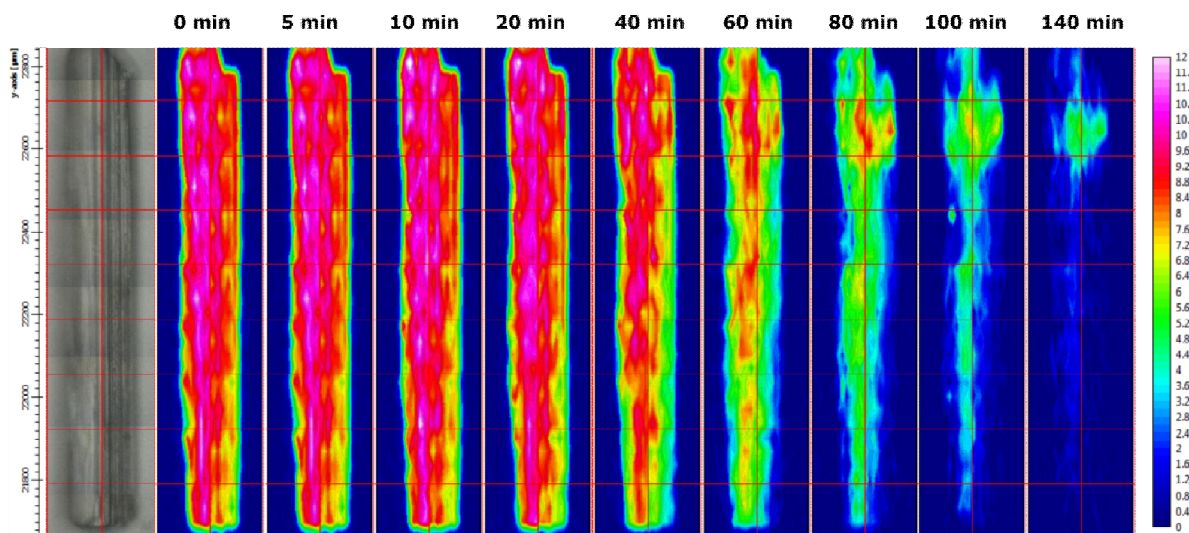


**Figure 7.4.** Infrared images collected with an FPA detector at RT after quenching the sample heated at 520°C for the indicated cumulative time. Doubly-polished prismatic crystal, 136  $\mu\text{m}$  thick. Left: optical image of the studied crystal; right: OH-absorbance scale. Absorbance values calculated by integrating the 3693-3560  $\text{cm}^{-1}$  wavenumber range.

A quantitative estimation of the evolution of the spatial distribution of the OH-absorbance as a function of time, was attempted by selecting sets of pixels from the FPA images of Figure 7.4, along both a longitudinal and a transverse profile across the crystal.

The longitudinal profile (Figure 7.5) features a generalized regular decrease in the OH-absorbance with time, as can be seen from the black trend which was calculated summing up the absorbance values of all of the selected points. The loss of hydrogen seems to be less efficient at the points A, and B than in C, D, and E. This effect may be due to some irregularity in the shape of the crystal, which as mentioned, has a strong tendency for cleavage and for this reason has uneven contours. Indeed, the positions A, B, and C, which are situated in an area where the sample has a more even and flat morphology, yielded flat trends in the first part of the experiment, followed by a regular absorbance decrease.

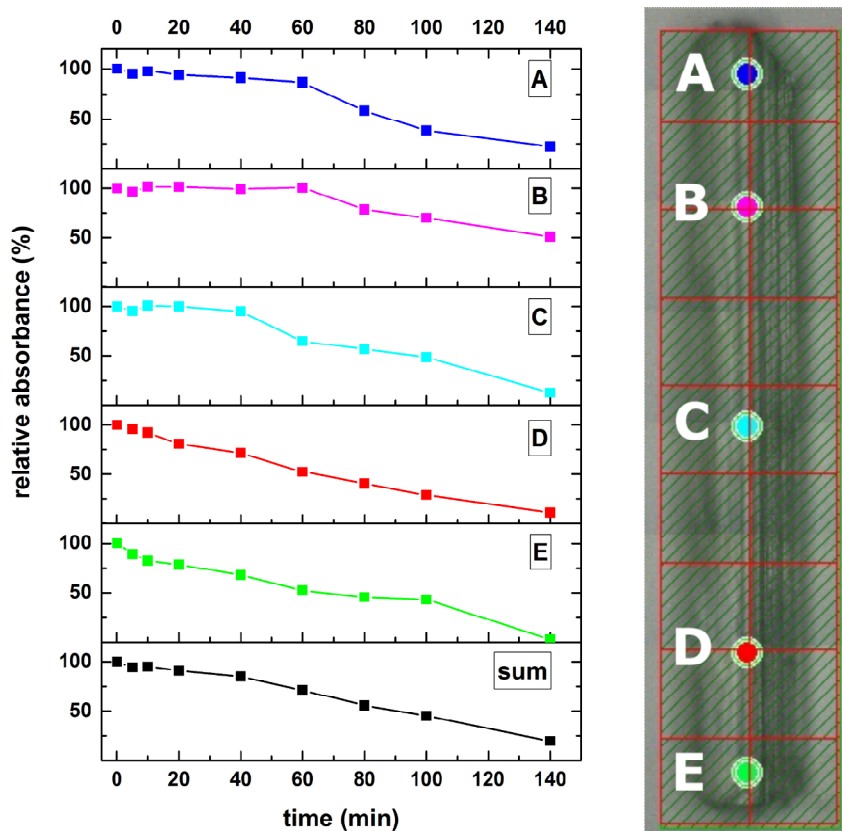


**Figure 7.5.** Absorbance trends as a function of time for a set of FPA pixels chosen along a longitudinal profile. The pixels were selected from the FPA images shown in Figure 7.4.



Also the longitudinal profile (Figure 7.6) features a generalized regular decrease in OH-absorbance with time, as can be seen from the black trend which was calculated summing up the absorbance values of all of the selected points. The hydrogen loss in this case seems to be less efficient at the central point than in the external ones. The central point, situated in an area where the sample has a more even and flat morphology, yielded a flat trend in the first part of the experiment, followed by a regular absorbance decrease. Also in this case, the irregularity of the sample toward the edges could play a role, facilitating the oxidation/deprotonation process through fractures or thinner parts.

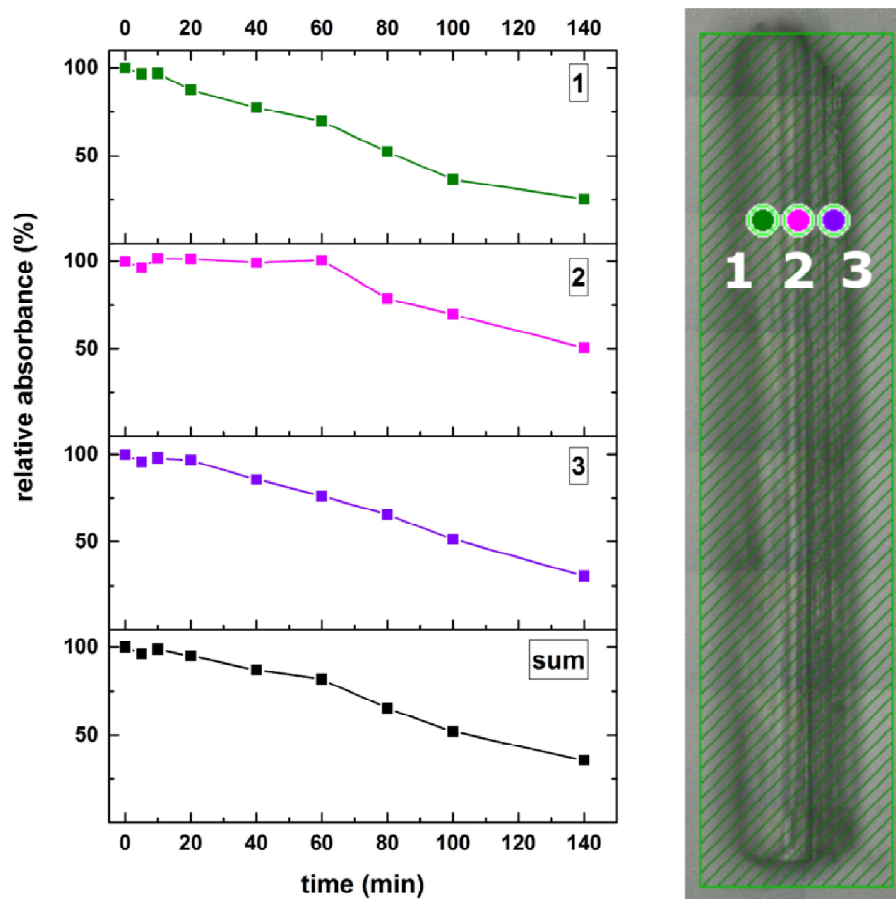


**Figure 7.6.** Absorbance trends as a function of time for a set of FPA pixels chosen along a transverse profile. The pixels were selected from the FPA images shown in Figure 7.4. The absorbance values calculated by integrating the  $3693\text{--}3560\text{ cm}^{-1}$  range.

### **7.3. *In situ* HT-IR on single crystal**

Additional FTIR data collection during isothermal experiments was performed *in situ*, at 520°C, on single spots arranged in transepts both parallel and normal to the elongation of the studied crystals. Compared to FPA imaging, single spot data have the advantage of being collected quickly while the process is running, minimizing the lapse of time between the beginning and the end of each measurement.

In order to collect spectra from a very small sample area, a synchrotron beam was used at Diamond Light Source. A Linkam 1400XY heating stage fitted on a Bruker Hyperion 3000 FTIR microscope equipped with a 36X Schwarzschild objective and a MCT N-cooled detector was used. The beam diameter was set at 15  $\mu\text{m}$ , the nominal resolution at 4  $\text{cm}^{-1}$ , 32 spectra were co-added for the sample and 128 for the background.

A 147  $\mu\text{m}$ -thick doubly-polished sample of riebeckite from Malawi was used for these experiment. The sample was heated up to 520°C with a rate of 90°C/min, then temperature was kept constant and a spectrum was collected at five different positions every 5 minutes. Note that the sample stage was programmed such as to return consecutively exactly on the same point during the data collection.

#### **Evolution of the OH-band intensity at HT at different positions on a single crystal**

The evolution with time of the OH-absorbance measured *in situ* at 4 points aligned on the elongation axis of a doubly-polished single crystal, is shown in Figure 7.7. Notably, all points in the central area of the crystal show an increase in absorbance in the initial stage of the isothermal experiment followed by a decrease. The sum of the absorbance values collected at the four points along the longitudinal transept reflects this generalized trend (black line).

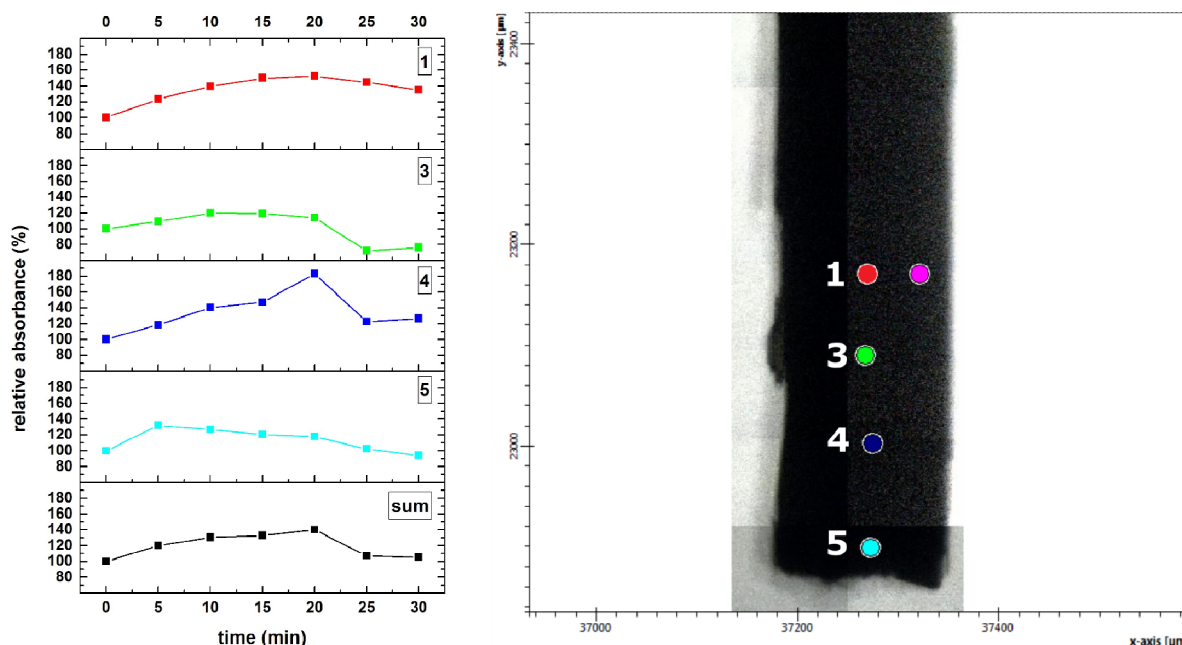


**Figure 7.7.** *In situ* absorbance trends as a function of time for a set of points chosen along the longitudinal direction of a 147  $\mu\text{m}$ -thick doubly-polished crystal. A synchrotron beam was used for a 15 x 15  $\mu\text{m}$  single spots. Absorbance values calculated by integrating the 3693-3560  $\text{cm}^{-1}$  wavenumber range.

The evolution with time of the OH-absorbance measured at two points along a direction normal to the elongation axis of the same sample is shown in Figure 7.8. It is noteworthy that the point located in the center of the crystal shows a significant first increase in absorbance, followed by a decrease, while the point on the crystal rim shows a monotonic decreasing absorbance as a function of time (pink points). The sum obtained mediating the values over the two points is however constant (black line).

Inspection of Figures 7.7 and 7.8 thus shows that the increase in absorbance at HT discussed in Chapter 5 seems to be maximized in the internal part of the crystal, along its elongation axis, while the rim displays a regular decrease in OH. However, the actual reason for the increase in absorbance observed in the early stages of the heating experiments is still unclear; further studies are needed to understand whether it is related to the proton migrating through the structure (Addison *et al.*, 1962a), or is just a thermal effect. This point is of paramount importance in this context, because it

could provide the key to model the whole process of Fe-oxydation and proton migration in these amphiboles as well as in Fe-bearing silicates in general.

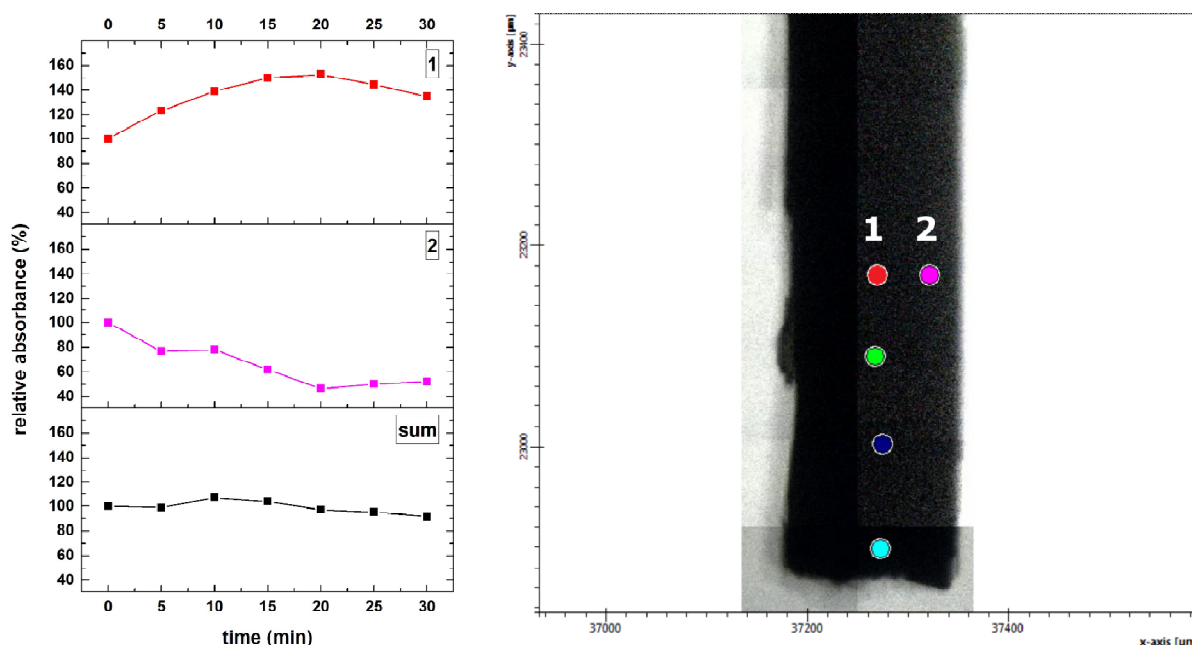


**Figure 7.8.** Absorbance trends as a function of time for a set of points chosen along a transversal direction of a 147  $\mu\text{m}$ -thick doubly-polished crystal. A synchrotron beam was used in order to obtain 15 x 15  $\mu\text{m}$  single spots. The absorbance values were calculated by integrating the 3693-3560  $\text{cm}^{-1}$  interval.

## 7.4. Isothermal measurements on powders

### Experiment on KBr pellets

During the first experiments on powders, the conventional KBr-pellet method was used for FTIR data collection. 5 mg of finely powdered riebeckite were mixed with 145 mg of KBr powder, and the mixture was pressed within a 13 mm die at 9 ton/cm<sup>2</sup> to obtain the pellet. A fragment of the pellet was heated up to 520°C using a Linkam 1400XY heating stage with a 90°C/min rate, then the temperature was held constant, and IR spectra were collected every 5 minutes using the same procedure described for single crystals (Section 5.1). Figure 7.9 shows that, in these conditions, no OH loss occurred after about three hours. This unexpected result suggested that the KBr matrix, by enveloping the powder prevented any contact between the amphibole grains and the atmospheric oxygen, thus inhibiting the Fe-oxidation. In turns, this observation clearly demonstrates that the hydrogen loss, depending from Fe-oxidation, is a basically surface phenomenon, as already suggested by earlier works (e.g. Addison *et al.*, 1962a; Addison and Sharp, 1962a, 1962b; and Hodgson *et al.* 1965). The strong dependence of the hydrogen loss from external oxygen availability also demonstrates that the amphibole deprotonation requires the Fe-oxidation to occur.

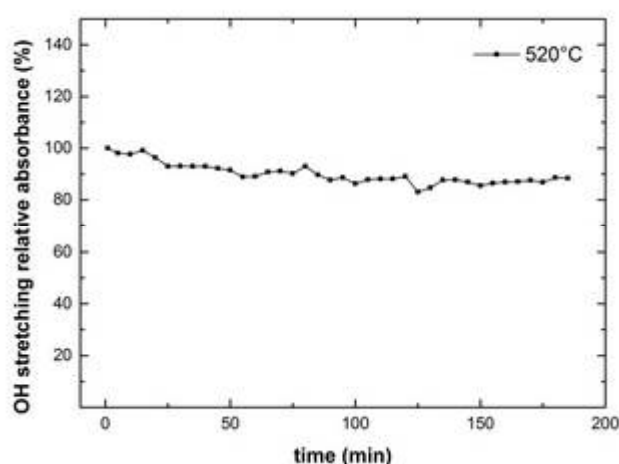
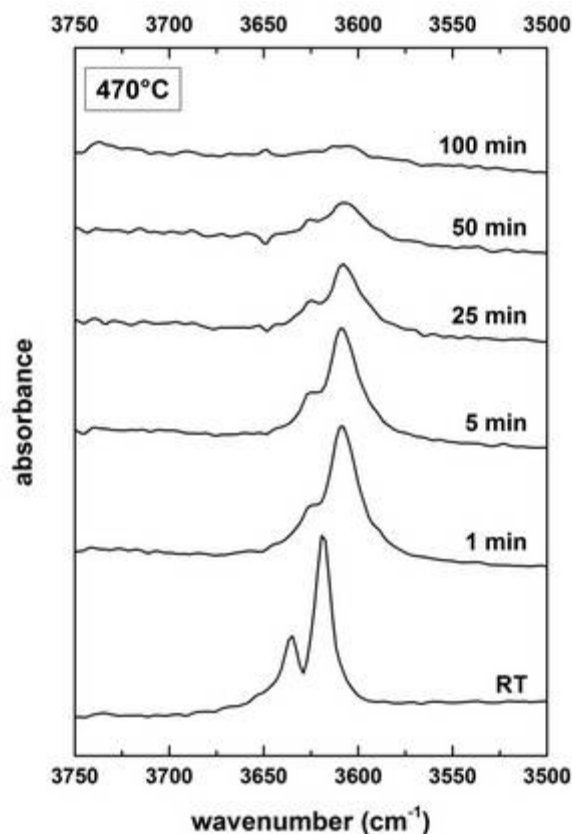


**Figure 7.9.** Absorbance values (integration range 3711-3560 cm<sup>-1</sup> range) in the OH-stretching region as a function of time collected at 520°C on a KBr pellet. *In situ* spectra collected every 5 minutes.

## Isothermal experiments on pure powders

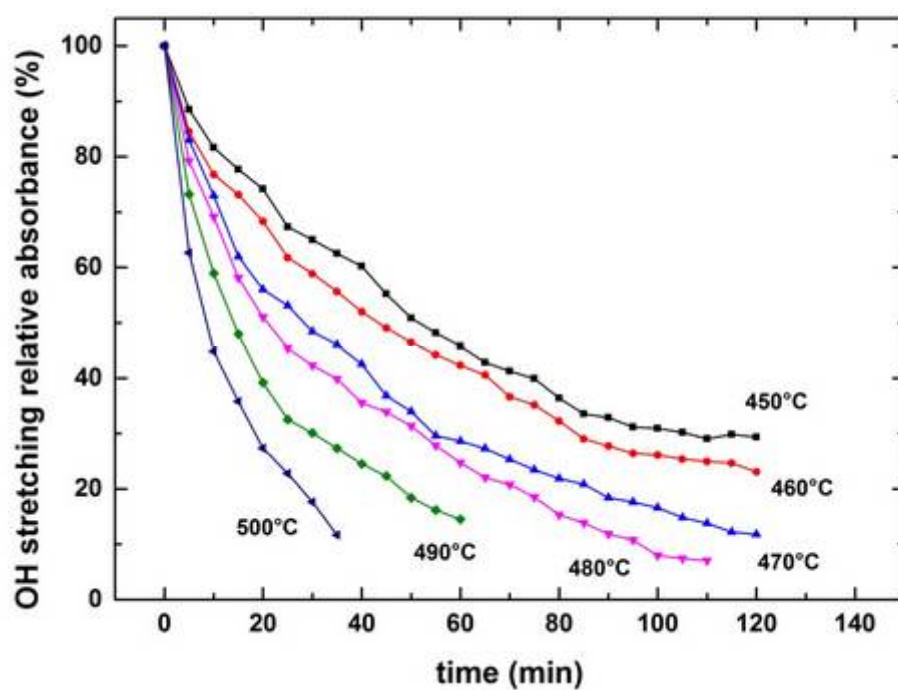
Based on the previous results with KBr pellets, we decided to use pure powdered samples for further heating experiments. A fragment of riebeckite was finely powdered, and six pellets of pure powder were obtained following the procedure described in Section 5.3 for the heating ramps. Non-polarized HT-FTIR spectra were collected at INFN (Frascati) with the same experimental set-up used for isothermal experiments performed on single crystals (Section 7.1). Six distinct isothermal data collections were carried out at 450, 460, 470, 480, 490, and 500°C, respectively. In each case the target temperature was reached as quickly as possible, with a rate of 90°C/min, and then held constant. A spectrum was collected every 5 minutes until either some OH-stretching band was visible, or the signal to noise ratio was still reasonable.

Figure 7.10 displays the spectra collected *in situ* after 1, 5, 25, 50 and 100 minutes, at 470°C. As already pointed out, at HT there is a shift in the position of the OH-stretching band compared to RT. This shift is already visible after one minute at 470°C; the same position in terms of frequency is maintained throughout the duration of the entire isothermal experiment. All spectra collected at 470°C feature a considerable broadening in the OH-stretching band if compared with the untreated sample, the three components previously described at RT are barely observable after 50 minutes at HT, and the overall band shows a rounded profile. Starting from the first minute at HT the OH-band decreases in intensity and, after 100 minutes, disappears.



**Figure 7.10.** OH-stretching spectra measured *in situ* after 1, 5, 25, 50, and 100 minutes at 470°C, respectively on pure powders. The spectrum collected at RT is also shown for comparison. Spectra plotted with the same absorbance scale.

Inspection of Figure 7.11, where the evolution of the intensity of the OH-stretching band for all isothermal experiments are plotted as a function of time, shows that pure powders are characterized by a defined decrease in absorbance. In addition, the loss of hydrogen occurs at lower temperatures when compared to what observed for single crystals.



**Figure 7.11.** OH-stretching absorbance as a function of time, collected during isothermal experiments done on pure powders. Intensities measured by integrating the  $3711\text{-}3560\text{ cm}^{-1}$  range.



## 7.5. Kinetics of H diffusion in amphiboles

At present, no experimental work has been done to study the kinetics of expulsion of protons from the amphibole structure. As it has been discussed above, this process is coupled to the  $\text{Fe}^{2+}$  oxidation at specific octahedral sites, as also shown by Oberti *et al.* (2016) for synthetic potassic-ferro-richterite, and further discussed in Chapter 3.

The curves of residual OH obtained from the FTIR isothermal experiments on pure powders were studied in order to evaluate the kinetics of the deprotonation process for the studied riebeckite. An attempt to determine the activation energy ( $E_a$ ) of the process, using the Avrami equation, is described.

### The activation energy of the deprotonation process in riebeckite

The mechanisms involved in the deprotonation/oxidation process at HT in Fe-rich amphiboles are still not clearly understood. Following the work previously done on different materials (Hancock and Sharp, 1972; Giampaolo and Putnis, 1989), this process can be tentatively modeled using the formalism suitable for first order reactions.

A first order reaction follows the general Avrami formula (Avrami, 1939, 1940, 1941) of exponential decay:

$$y = 1 - \exp(-ky^m) \text{ or } y_y = y_0 \cdot \exp(-ky^m) \quad (7.1)$$

where  $y = 1 - A_t / A_0$  is the fraction of  $\text{H}^+$  lost at time =  $t$  (min),  $A_t$  is the integrated absorbance ( $A_i$ ) at time =  $t$ ,  $A_0$  is  $A_i$  at time = 0 and  $f(t)$  is a time dependent exponential function.  $f(t)$  is usually described by two parameters  $k$  and  $m$ . The coefficient  $k$ , also called the rate constant, describes the way the decrease depends on the concentration of the reactant. The exponential factor  $m$  is an empirical factor

used to model the reaction mechanism. Curves with the same value of  $m$  are isokinetic and indicate that the reaction mechanism does not change within the examined range of temperature or fraction loss. The kinetic parameter  $k$  may be used, *via* the Arrhenius equation, to calculate the activation energy  $E_a$  (kJ/mol) of the process leading to  $H^+$  loss from the amphibole structure:

$$y = y_0 \cdot \exp \left( -\frac{y_0}{y} \right) \quad (7.2a)$$

Linearized:

$$\ln y = \ln y_0 - y_0 / y \quad (7.2b)$$

where  $R$  is the universal gas constant (kJ/mol K),  $T$  is the temperature in K and  $\alpha$  is the frequency factor.

An arrangement of Avrami equation (Giampaolo and Putnis; 1989, Putnis *et al.*, 1990; Putnis, 1992) is:

$$y = y_0 \cdot \exp \left[ -(y \cdot y_0)^y \right] \quad (7.3)$$

It is important to note that in the latter formula the rate constant  $k$  has always the dimension of  $t^{-1}$ . A slightly different form of the Avrami equation used in literature to describe deprotonation in minerals is proposed by Hancock and Sharp (1972) and Carbone *et al.* (2008). The former type was preferred to the latter, since this proved to be dependent on the thickness of the sample (Radica, 2015), a parameter that is impossible to take into account when dealing with powders.

Figure 7.12 shows the results of fitting the Avrami equation to the experimental data for the IR OH-stretching band intensity as a function of time, collected on powders during the isothermal experiments. The fitted parameters are listed in Table 7.1 for each isothermal experiment.

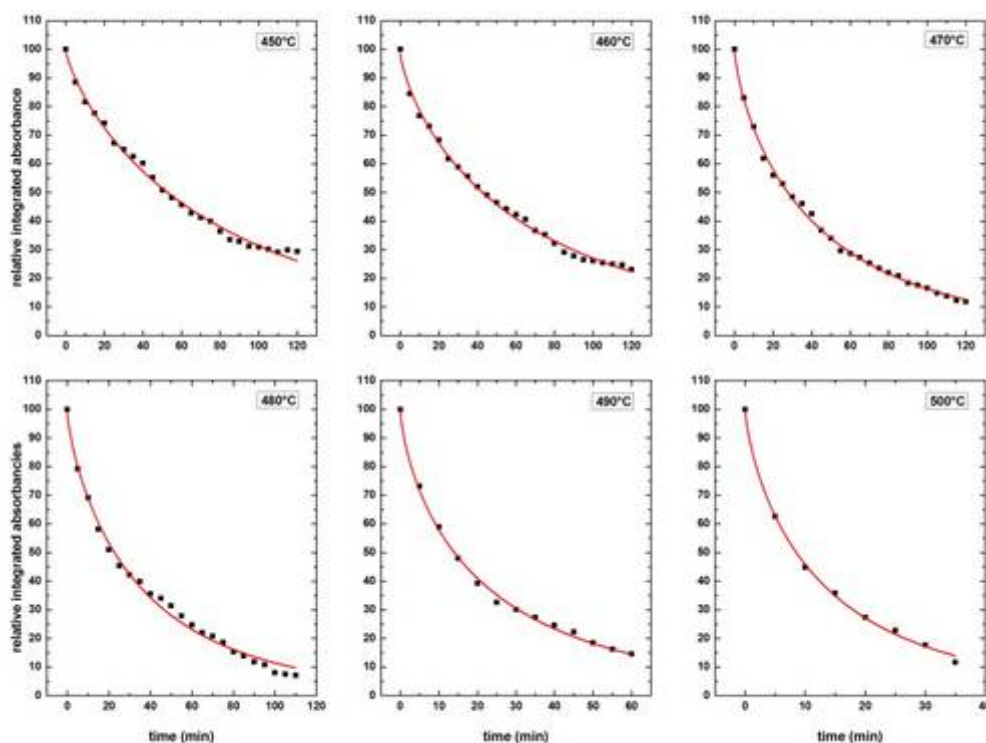


**Figure 7.12.** Evolution of the absorbance integrated in the principal OH-stretching region as a function of time, for the experimental data set collected for the pure powdered sample. Curves are fitted by Avrami equation.

Model	Avrami Putnis							
Equation	$A = A_0 \cdot \exp(-(K \cdot t)^m)$							
Temp(°C)	$A_0$	Std.Error	k	Std.Error	m	Std.Error	Red.Chi-Sq	Adj.R-Sq
450	99.44007	1.37231	0.01194	2.59939E-4	0.8084	0.02834	2.47437	0.99434
460	98.73172	1.15347	0.0141	2.79292E-4	0.75682	0.02051	1.63075	0.99638
470	99.83103	1.08868	0.02207	4.40188E-4	0.75005	0.01604	1.36804	0.99753
480	98.77183	1.97375	0.02687	9.79577E-4	0.77856	0.03007	4.415	0.99271
490	100.46885	1.36679	0.04274	0.00121	0.70459	0.02268	1.92444	0.99699
500	99.92025	1.31842	0.0714	0.00209	0.74248	.02845	1.75318	0.99792

**Table 7.1.** Arrhenius equation parameters for each isothermal experiment done on pure powdered samples obtained by fitting the experimental data using the Avrami equation.

In Figure 7.13 the fitted parameters are plotted in the Arrhenius space. The activation energy ( $E_a$ ) expressed in kJ/mol (Equation 7.2b above), corresponds to the slope of the regression line through the data points.

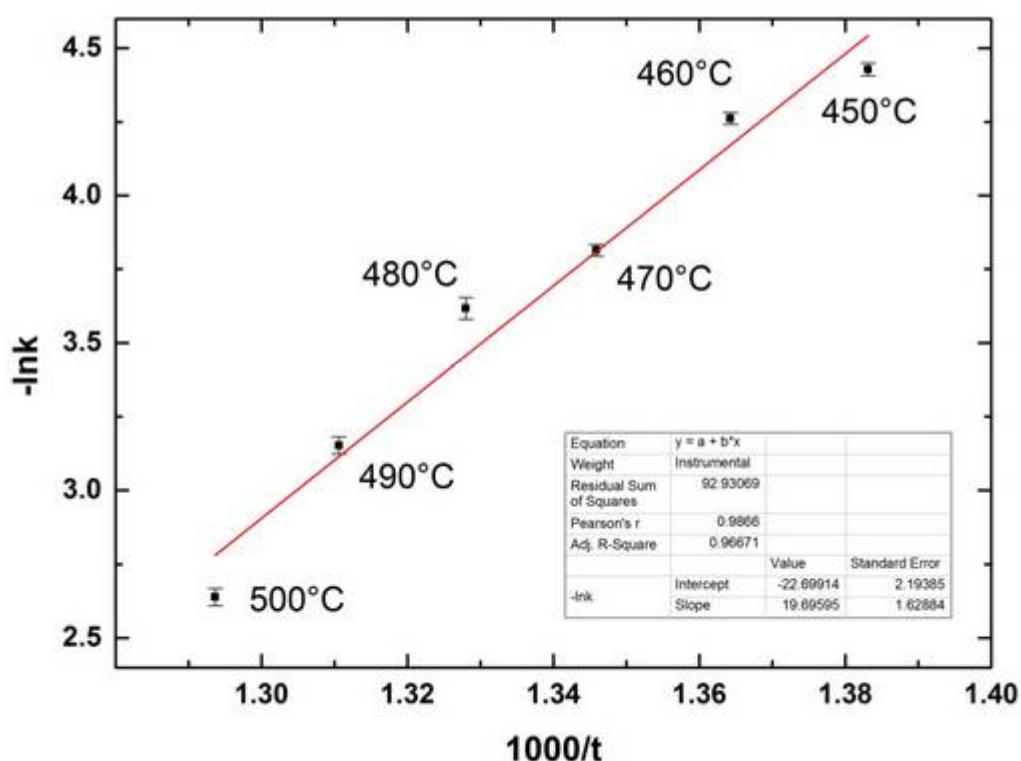


**Figure 7.13.** Arrhenius plot for the data listed in Table 7.1. The intercept and the slope of the regression line, with the relative standard deviations, are given in the inset.

The final  $E_a$  for the deprotonation/oxidation process for powdered riebeckite using the Avrami equation is  $20 \pm 2$  kJ/mol. Since this value was estimated from the curves of residual OH, the obtained result has to be intended as the amount of energy required for deprotonation/oxidation to happen, regardless of the actual mechanism of migration of protons toward the surface of the crystal.

In Table 7.2, the experimental results for  $H_2$  and  $H_2O$  diffusion through various silicate minerals and melts available in literature are reported. As can be noticed, the  $E_a$  obtained for our process is considerably lower than activation energies obtained for pure diffusive processes of  $H_2$  and  $H_2O$  molecules through several different

crystal structures. It is difficult to compare our result with the data found in the literature because most studies were done on materials where the diffusion occurs following mechanism extremely different to the one studied here. The only clear inference possible is that the process studied in this work occurs at lower temperatures and requires less energy than those addressed in the works listed in Table 7.2.

Mineral	Diffusing molecule	T (°C)	P (MPa)	$E_a$ (kJ/mol)	Reference
Biotite	H <sub>2</sub> O	500 - 800	100	143	Fortier and Giletti, 1991
Tourmaline	H <sub>2</sub> O	450 - 800	0	128	Jibao and Yaqian, 1997
Forsterite	H <sub>2</sub> O	900 - 1100	200	205	Demouchy and Mackwell, 2003
Quartzite	H <sub>2</sub> O	450 - 800	100	113	Farver and Yund, 1991
Beryl	H <sub>2</sub> O	500 - 700	50 - 150	133	Fukuda <i>et al.</i> , 2009
Kaersutite	H <sub>2</sub>	600 - 900	0.1	104±12	Ingrin and Blanchard, 2000

**Table 7.2.** Comparison of the experimental data for H<sub>2</sub>O and H<sub>2</sub> diffusion in various silicate minerals and melts found in the literature.

Only few data are available in the literature for amphiboles: Addison *et al.* (1962b) plotted the rate of O<sub>2</sub> absorbed by 1 gr of crocidolite in one hour versus the reciprocal temperature, and from the slope of the regression line calculated an activation energy for the oxidation process of 88 kJ/mol, when using a liquid nitrogen cold trap and 138 kJ/mol when using a carbon dioxide cold trap (see Chapter 2). Similar activation energies, in the range 67 to 104 kJ/mol, were obtained by Graham *et al.* (1981) for various amphiboles using D-H exchange experiments. Ingrin and Blanchard (2000) determined hydrogen diffusion rates in single crystals of kaersutite using sequential FTIR analysis. The experiments were done at 600-900 °C and 0.1 MPa pressure in a 90%Ar:10%2H<sub>2</sub> atmosphere. Activation energy of 104±12 kJ/mol was obtained. In addition, Ingrin and Blanchard (2000) data clearly demonstrate that hydrogen diffusion in amphibole is anisotropic, with transport along the c-axis being about a factor of five faster than along the b-axis. Wang *et al.* (2012) studied the electrical conductivity of amphibole-bearing rocks under middle to lower crust

conditions, performing alternating current measurements in the frequency range of  $10^{-10}$ – $10^{-6}$  Hz at 0.5–1.0 GPa and 100–600°C. The activation energy for the electrical conductivity up to 530°C, resulted to be 64–67 kJ/mol. They concluded that the dehydration in amphiboles is associated with the oxidation of iron, causing increased conductivity at HT. The sample studied by Wang *et al.* (2012) was however a rock consisting of 80% hornblende with intermediate Mg-Fe composition, plus additional minerals, and this explains the discrepancy of their value with the one obtained here.

Summarizing, a range of values have been obtained for amphiboles by the different authors, but these are difficult to compare because: (1) they have been obtained using extremely different procedures, thus referring to phenomena which are correlated but not identical (e.g. electron conductivity vs. H diffusion); (2) they have been obtained using different sample types (single crystals, fibrous crystals and powders) and we have shown above that the dehydration process is strongly dependent on the sample dimension, and (3) they have been obtained using different amphibole compositions and we have shown above that the dehydration process is strongly dependent on the Fe/Mg content of the sample.

## Chapter 8 Discussion and final remarks

---

The behavior of minerals at non-ambient conditions, and in particular at high temperatures, is of great interest in a wide variety of technology areas, including energy, electronic, photonic, and chemical applications. The physical and crystal-chemical properties of materials are in fact strongly dependent from the temperature, and admittedly material's properties, such as electrical, magnetic and chemical, measured at  $RT$ , cannot be extrapolated at  $HT$ . For example, chemical reactions not favourable at room- $T$  may become important at high temperatures and thermodynamic properties rather than kinetics tend to determine the high reactivity of such materials. This is reflected by the large number of disciplines interested in the study materials properties at high- $T$ , including ceramic science, chemistry, chemical engineering, electrical engineering, mechanical engineering, metallurgy, and physics. The diversity of interests ranges from experimental observations to predicting behaviour, from scientific principles to materials design, from atomic scale models to performance while in use.

Most natural (geologic/geophysics) and technical/industrial processes do involve processes as dehydration/deprotonation, chemical transformations and phase-transitions which need to be properly characterized to use mineral associations and compositions as geothermometers/geobarometers. This can be done using X-ray diffraction at  $HT$ , however it is now clear that the obtained information need to be complemented by additional techniques, such as TG/DTA, and, in particular  $HT$  spectroscopies.

FTIR spectroscopy is in absolute the most sensitive techniques to analyse hydrous species in minerals, and has therefore been widely used in high- $T$  materials research in the past. However recent studies (Keppler and Bagdassarov, 1993; Yamagishi *et al.*, 1997; Zhang *et al.*, 2007, 2010; Tokiwai and Nakashima, 2010a,b among the others) have shown that absorption coefficients measured at  $HT$  can be significantly affected by temperature, thus making quantitative studies using this technique difficult. This PhD work has been undertaken in order to investigate the

use of HT spectroscopy in different systems. As a preliminary test, the technique was applied to a sulfate system (homannite) where the mineral transformations as a function of  $T$  were relatively well constrained based on X-ray diffraction. The results were used to set-up some technical procedures and details, and are described at the beginning of this text. However, the main goal of this Thesis was focused on a particular issue in mineralogy: the HT processes in Fe-rich amphiboles. In most transformations involving important rock-forming minerals, the loss and subsequent diffusion of hydrogen is associated to simultaneous oxidation processes of Fe, with consequences on the physical properties of the rock where they occur. The high electrical conductivity in Earth's crust and in the upper mantle, for instance, has been related to these phenomena (e.g. Karato and Wang, 2012; Wang *et al.*, 2012; Wang and Karato, 2013). Dehydration reactions are expected to occur in a variety of geological processes, notably subduction at convergent plates margins, thus knowledge of their effects on the physical properties of minerals has paramount interest in geophysical modelling. Despite this, the influence of dehydration reactions on electrical conductivity of hydrous minerals is still unclear. In this connection, amphiboles have been widely studied with respect to their thermal stability in the last few years, and several crustal-chemical features controlling the chemical and structural adjustments accompanying HT treatments are now been clarified. However, several issues still need to be studied, including the way the proton diffuses throughout the mineral matrix, and the role of multiple-valence elements, notably Fe, in this process. The main goal of this Thesis was thus focused at gathering new knowledge on this subject by combining diffraction and spectroscopic methods.



## 8.1. The HT study of hohmannite, $\text{Fe}_2[\text{O}(\text{SO}_4)_2] \cdot x\text{H}_2\text{O}$

As discussed above, this study was undertaken as a test for the spectroscopic set-up for HT researches, and was finally employed to complement on-going X-ray studies, in collaboration with the crystallography group of the University of Bari. *In situ* X-ray diffraction data, combined with HT-IR spectroscopy analysis and with the aid of available TG and DTA data, allowed addressing the dehydration mechanisms during the heating of hohmannite (Chapter 1). The obtained results showed that the thermal decomposition of this Fe-sulfate, from RT up to 800°C, occurs in five steps. IR data proved to be crucial in revealing the presence of hydrous phases formed during the complex sequence of structural/chemical transformations in the studied system.

FTIR, along with TG data, allowed to detect the partial dehydration from hohmannite to metahohmannite between 80 and 120°C. A second step consists in the decomposition of metahohmannite and in the formation of an OH-bearing Fe-sulfate between 150 and 220°C. IR spectroscopy shows the appearance of the OH-combination band, and thus of the hydroxyl-bearing Fe-sulfate, at 220°C. The third step starts at 330°C and consists in the decomposition of the hydroxyl-bearing Fe-sulfate. FTIR spectra show the presence of OH-groups, and hence of the OH-bearing sulfate, up to 550°C.

## 8.2. HT study of Fe-rich amphiboles

Two Fe-end member amphiboles, were studied for this Thesis: a synthetic potassic-ferro-richterite and a riebeckite; the results of this work are described in Chapters 3 to 7, where the experiments done by combining both powder and single crystal diffraction, HT-FTIR and Mössbauer are reported. Three notable points of general significance for any HT study of Fe-silicates emerged during the work, i.e. (1) the difference between *in situ* and *ex situ* (quenched) measurements, (2) the difference due to the sample type (i.e. powder vs. single crystals), and (3) the importance of the confining atmosphere on the final results. A significant difference in the H-loss temperature was also observed between the XRD and FTIR results. In the following paragraphs I will thus try to combine the different information into a general picture of the deprotonation process of Fe-amphiboles, summarizing the main results obtained here and highlighting those issues that are still unclear.

### The deprotonation mechanism of Fe-amphiboles

HT-FTIR spectra collected during an heating ramp on both potassic-ferro-richterite and riebeckite, showed a quick loss of hydrogen in the 400-500 and 550-650°C *T* range for potassic-ferro-richterite (Chapter 3) and riebeckite (Chapter 5), respectively. Structural refinements (SREF), and in particular the variation of the cell parameters, <M-O> bond distances and electron densities at the relevant sites, showed an increasing amount of the oxo-component in the amphibole, coupled to increasing  $\text{Fe}^{2+} \rightarrow \text{Fe}^{3+}$  oxidation. In particular, SREF data suggest exclusively  $^{M(1)}\text{Fe}^{2+}$  oxidation (Oberti *et al.*, 2016). This conclusion is coherent with the Mössbauer results on riebeckite. These results are also consistent with preliminary XAS data collected on powdered potassic-ferro-richterite (B12 beamline, diamond Light Source, Oxford, UK: Salvatore Macis, pers. comm.) showing a significant increase of the  $\text{Fe}^{3+}/\text{Fe}^{2+}$  ration in the 350-450°C *T* range.

Careful examination of the SREF data collected for riebeckite (Section 6.1) showed also that the Fe-oxidation/deprotonation process is associated with a migration of cations from the *B*-sites to the *A*-sites, again necessary to provide additional bond-valence to those O(3) oxygens undercharged by the loss of hydrogen (e.g. Ungaretti *et al.*, 1980). Notably, the increasing occupancy of the *A*-site is not translated into the appearance of new bands in the FTIR spectra and this indicates strong SRO involving the oxo-component at O(3) and the *A*-cation. This local configuration, that can be expressed as  $^{M3}\text{Fe}^{2+M1}\text{Fe}^{2+M1}\text{Fe}^{3+}\dots\text{O}^{2-}\dots \text{A}$ , is in fact invisible to IR.

Therefore, combination of SREF, Mössbauer and FTIR definitively demonstrates that the deprotonation of Fe-amphiboles occurs via the oxidation of  $\text{Fe}^{2+}$  and is needed to restore local charge equilibrium. This feature had already been observed in earlier works (e.g. Ungaretti *et al.*, 1978; Ungaretti, 1980) and more recently in Oberti *et al.* (2016), however a complete study done by combining diffraction and spectroscopy (Mössbauer, FTIR) had never been done so far. IR spectra collected on the synthetic potassic-ferro-richterite after quenching (Chapter 3) showed the growth, in the O-H stretching region, of a new band related to the increase of  $\text{Fe}^{3+}$  at the *M*(1,3)-sites; in riebeckite (Chapter 5), however, there is the decrease in intensity of all bands without the appearance of additional components due to  $\text{Fe}^{3+}$  at the OH-coordinated sites. This different behaviour can be related to the lack of vibrational coupling between facing anionic sites in the riebeckite structure, due to the absence, in riebeckite, of a bridging cation at the alkali-site. Such behavior is in agreement with the work of Robert *et al.* (1999, 2000) on OH-F substituted amphiboles.

### The H-loss temperature: difference between the XRD and FTIR data

*In situ* HT-FTIR spectroscopy (this Thesis, Chapter 3) provided a deprotonation  $T$  for potassic-ferro-richterite that is almost 100°C higher than that provided by single crystal X-ray diffraction (Oberti *et al.*, 2016) on the same sample (Figure 8.1).

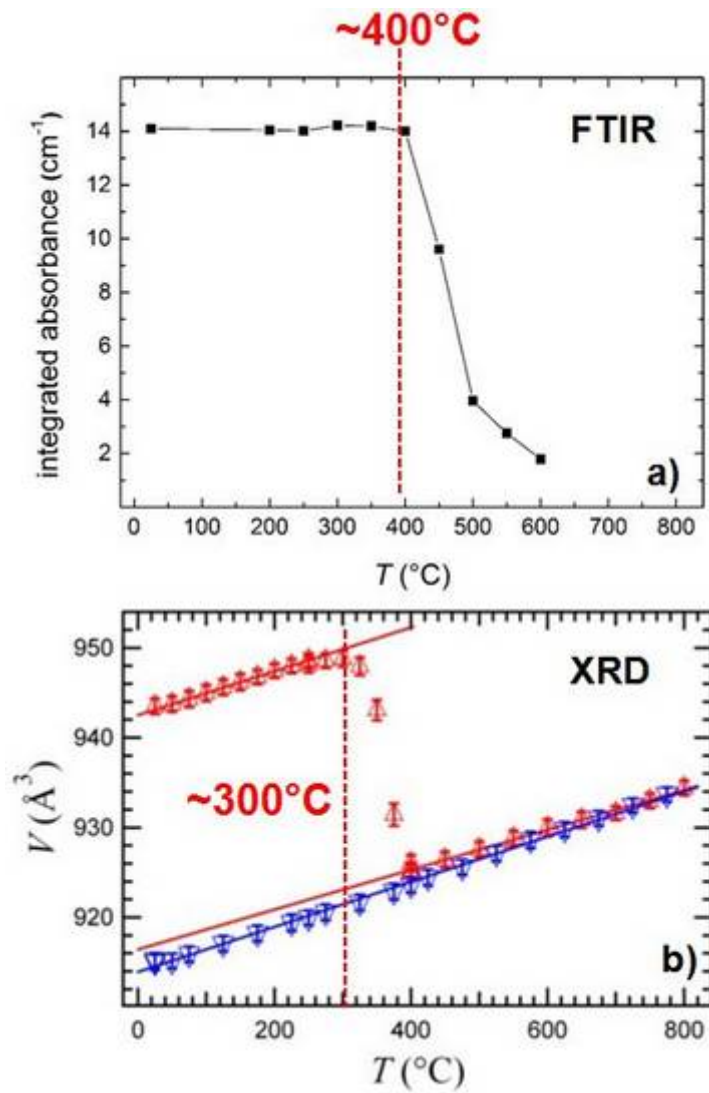


**Figure 8.1.** Evolution (a) of the OH-stretching absorbance (quenched data) obtained in this study, and (b) of the *in situ* cell volume of potassic-ferro-richterite (from Oberti *et al.*, 2016).

Both the heating stage used during this work, and the furnace used by Oberti *et al.* (2016) were calibrated against the melting point of known substances, thus the used set-ups cannot explain this discrepancy. One possible explanation could be looked for in the different heating regimes used for the two experiments, i.e. to the faster FTIR data collection with respect the XRD data collection. However, this possibility can be discarded just by noting that, if this was the case, the H-loss  $T$  yielded by FTIR had to be lower (for kinetic reasons) than that yielded by SREF, but the opposite is observed. In addition, preliminary data obtained on powdered potassic-ferro-richterite by simultaneous XRD/XAS experiments done at beamline B18 (Diamond, UK) yielded the same transition  $T$  (Fig. 8.2) as that reported by Oberti *et al.* (2016), suggesting that the sample type (i.e. powder vs single crystal) has not a significant effect for XRD results. Unfortunately we had no sample left for collecting powder HT-FTIR data for potassic-ferro-richterite. This problem was thus addressed in details for riebeckite, because in that case we had large amounts of sample to do all needed tests.

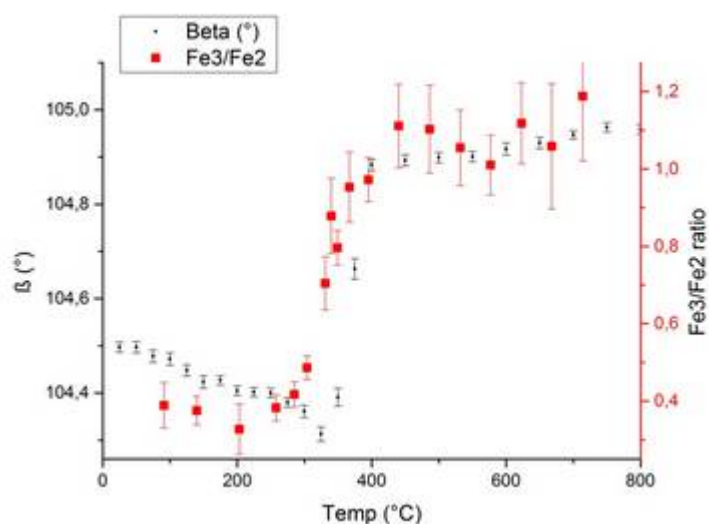


**Figure 8.2.** Evolution of the  $\text{Fe}^{3+}/\text{Fe}^{2+}$  ratio in synthetic potassic-ferro-richterite as a function of increasing  $T$ . The evolution of the  $\beta$  angle refined from simultaneous powder XRD data is also given (unpublished data, courtesy of S. Macis).

HT-FTIR spectra collected on powdered riebeckite (prepared without KBr matrix, for the reasons discussed below) yielded a complete hydroxyl loss for  $T > 400^{\circ}\text{C}$  (Section 5.3); refinement of HT X-ray powder diffraction patterns (Section 6.2) showed an abrupt contraction of the unit cell parameters at almost the same temperature. Since  $\text{Fe}^{3+}$  cations have smaller ionic radii compared to  $\text{Fe}^{2+}$  cations, the contraction of the  $b$  cell parameter is compatible with oxidation of  $\text{Fe}^{2+}$  at the  $M$ -sites, while a major contraction along the  $a^*$  direction is compatible with a loss of  $\text{H}^+$  in the same  $T$  range. Mössbauer spectra collected on heat-treated powders confirmed that  $\text{Fe}^{2+} \rightarrow \text{Fe}^{3+}$  oxidation becomes prominent starting from  $400^{\circ}\text{C}$  (Section 6.3). Based on this evidence we can confidently state that the Fe-oxidation/deprotonation process starts at  $T \geq 400^{\circ}\text{C}$  in riebeckite; the important point here is that when collecting data on powders, FTIR and XRD provide the same deprotonation  $T$ . It is also noteworthy that the same deprotonation  $T$  ( $400^{\circ}\text{C}$ ) was observed on riebeckite single crystals (R. Oberti, pers. comm.).

Summarizing, the same deprotonation temperatures are obtained when using *in situ* HT-FTIR and HT-XRD techniques on powders, while a  $100^{\circ}\text{C}$  shift is observed when using single crystal FTIR vs. both powder and single crystal XRD. The reason for this discrepancy must be connected with the deprotonation mechanism; as it will be discussed below, this process is basically a surface process, thus it is enhanced for powders with respect to single crystals. However, this enhancement is observed only when using FTIR. In other words considering that (1) the H-loss is connected to (2) the  $\text{Fe}^{2+}$  oxidation, the same  $T$  should be observed when probing (1) by FTIR and (2) by XRD, but this is not the case. This point still needs to be completely understood, but the above observation clearly suggests that the electron diffusion, consequent to the  $\text{Fe}^{2+}$  oxidation, must be faster than the proton diffusion. This point will be discussed in more details below.

### **Amphibole deprotonation: a surface process requiring external $\text{O}_2$**

HT-FTIR experiments done on riebeckite powders embedded within the classical KBr pellet showed no hydrogen loss after 180 minutes at  $520^{\circ}\text{C}$ , suggesting

the absolute necessity of the contact within the sample and the external oxygen for the Fe-oxidation (necessary for deprotonation) to occur. When using pure pressed powder instead of KBr pellets, the deprotonation process, in fact, proceeded as expected (Chapter 6). Additional FTIR experiments were done on single crystals using a flux of N<sub>2</sub> into the heating cell, and again a significantly reduction of proton loss (20% after four hours at 520°C) with respect to the same experiments done in presence of air, was obtained (see Fig. 7.3).

These results demonstrate that the Fe-oxidation/deprotonation process in amphiboles is extremely sensitive to the availability of oxygen in the surroundings of the sample. Addison *et al.* (1962a) and Hodgson *et al.* (1965) suggest that the whole process initiates at the crystal surface, where Fe<sup>2+</sup>, OH<sup>-</sup> and gaseous oxygen are available; it can be described by the reaction (Addison and Sharp, 1962b), here referred as “deprotonation reaction” (Chapter 2):



On the left-side of Equation 8.1, the reactants Fe<sup>2+</sup> and OH<sup>-</sup> are provided by the amphibole, while O<sub>2</sub> is provided by the external atmosphere. The important point is that Fe<sup>3+</sup> and O<sub>2</sub><sup>2-</sup> on the right-side of the equation are still part of the (oxo)-amphibole, while only H<sup>+</sup> is released and reacts at the crystal surface with gaseous O<sub>2</sub> to produce H<sub>2</sub>O. For the reaction to proceed, there is the need of continuous availability of Fe<sup>2+</sup> and H at the crystal surface, and these must be provided by the crystal interior, via electron and proton diffusion.

Schmidbauer *et al.* (2000) studied the electrical resistivity and Mössbauer spectra of three calcic amphiboles with different Fe contents. They concluded that for  $T < 600^\circ\text{C}$  their results were compatible with a charge transport mechanism due to electron hopping between Fe<sup>2+</sup> and Fe<sup>3+</sup> cation across the structure.

The results obtained during this Thesis show that Fe<sup>2+</sup> at M(1) is oxidized for increasing  $T$  and that this process is coupled with a simultaneous loss of H at the NN O(3)-site according to



This reaction thus produces one electron and one proton that are free to move. The electron can jump toward one adjacent  $\text{Fe}^{3+}$  within the same octahedral strip thus, forming a transient state, according to



At this point the new formed, transient  $\text{Fe}^{2+}$  cation, does not satisfy its local bond-valence requirements, and is instable, thus reverting immediately to the  $\text{Fe}^{3+}$  oxidation state, releasing the electron, according to



The electron is transferred to another adjacent  $\text{Fe}^{3+}$  cation (Equation 8.3) along the same octahedral strip, and so on.

We think that a similar process could produce an effective and fast migration of electrons from within the crystal to the surface along the octahedral strip, hence along the  $c$  crystallographic axis, as schematically shown in Figure 8.3, regenerating the reactant  $\text{Fe}^{2+}$  at the surface.

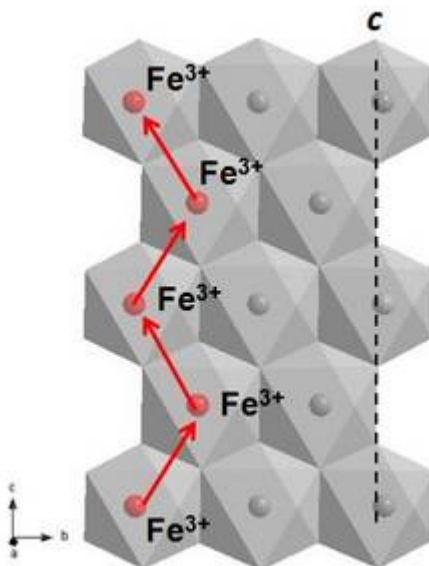


**Figure 8.3.** Schematic representation of the electron hopping among adjacent  $\text{Fe}^{3+}$  along the octahedral strip ( $c$  crystallographic direction).



The process described by Equation 8.1 indeed requires also the  $\text{OH}^-$  groups to be refurnished at the surface, and this implies the diffusion of the H ions released during the  $\text{Fe}^{2+} \rightarrow \text{Fe}^{3+}$  oxidation. As already stated above, careful examination of the data suggests that the proton diffusion is slower than the electron diffusion, an inference that is also in agreement with the fact that the diffusion in solid structures is strongly correlated with the size of the diffusive species. A further element supporting this inference comes from comparison of the evolution of the XRD data (representing the oxidation, to simplify), and the evolution of the FTIR data (representing the deprotonation) in powders. Inspection of Figure 8.4, in fact, shows that the process sampled by XRD occurs in a strongly reduced  $T$  interval ( $\sim 25\text{--}50^\circ\text{C}$ ) when compared to the process sampled by FTIR that is completed in a wider  $T$  interval ( $\sim 100^\circ\text{C}$ ).

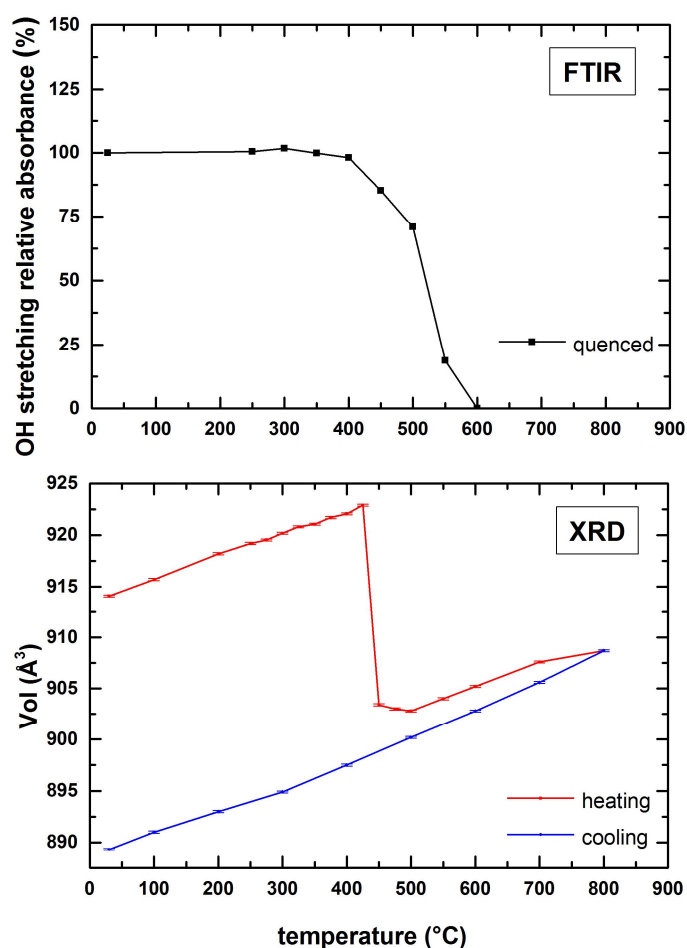


**Figure 8.4.** Comparison between HT X-ray diffraction and HT-FTIR OH results for powdered riebeckite.

The hydrogen diffusion in minerals is a complex process (Ingrin and Blanchard, 2006) and indeed few data are found in the mineralogical literature for amphiboles. The curves of residual OH from the FTIR isothermal experiments done here on pure riebeckite powders (Fig. 7.11), were fitted via the Avrami equation (Putnis *et al.*, 1990; Putnis, 1992). The obtained rate constants ( $k$ ) were plotted in the Arrhenius space, and the activation energy ( $E_a$ ) for the deprotonation process resulted to be  $20 \pm 2$  kJ/mol (Chapter 7). This value is lower than those derived by previous authors that are in the range 60 - 140 kJ/mol (Chapter 7). This discrepancy is readily explained once considering that the different values have been obtained using extremely different procedures, different sample types and different amphibole compositions, all issues that affect significantly the final results, as it has been demonstrated during this Thesis work. The direct implication is that additional studies done with modern techniques and by combining several methods are needed to address this topic that is of paramount importance in geology and geophysics.

### The OH-band intensity: *in situ* vs. quenched data

HT-FTIR experiments performed both on synthetic ferro-potassic-richterite (Chapter 3) and riebeckite (Chapter 5), showed a significant increase in OH-absorbance in the spectra collected *in situ* for increasing temperatures up to the deprotonation  $T$ . This increase cannot be explained with a gain in hydroxyl, since the IR spectra collected after quenching from the same temperatures show a constant OH-absorbance up to the deprotonation  $T$ ; this point needs now to be discussed.

Recent work (e.g. Zhang *et al.*, 2007, 2010; Tokiwai and Nakashima, 2010) has addressed the dependence of the OH-band intensities from  $T$  in a variety of minerals; the departure of the observed absorbance ( $A$ ) from that expected, based on the amount of water in the sample, has been explained as due to the dependence with  $T$  of the constant of proportionality (the molar absorption coefficient,  $\varepsilon$ ) between  $A$  and  $H_2O$  concentration in the Beer-Lambert equation. In all previous studies, however, a decrease in the OH-intensity has been systematically reported, while in our experiments (Fig. 8.5) a strong increase of the OH-band intensity is observed.

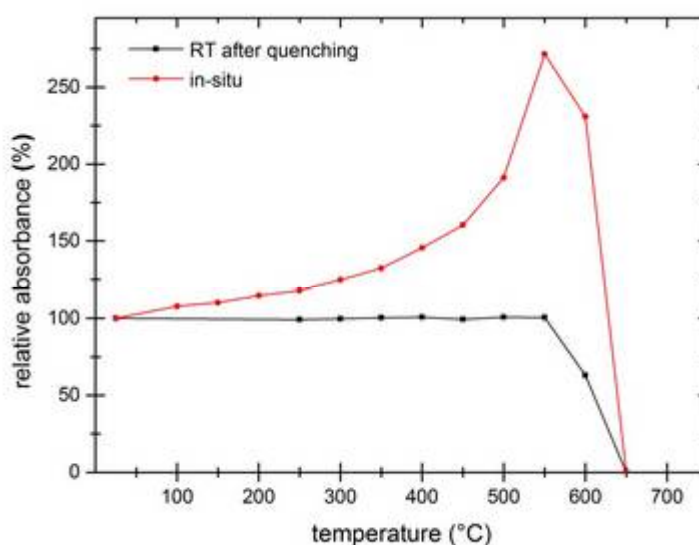


**Figure 8.5.** OH-stretching integrated absorbance (integration range is  $3711\text{-}3560\text{ cm}^{-1}$ ) as a function of  $T$ ,  $111\text{ }\mu\text{m}$ -thick doubly-polished section of riebeckite from Malawi.

Another point that is worth mentioning is that in all previous study a linear dependence between  $A$  and  $T$  has been reported, while for the studied Fe-amphiboles a non-linear trend is observed. For muscovite (see Tokiwai and Nakashima, 2010), the decrease in OH-intensity before deprotonation has been explained by taking into account a tilting of the O-H dipole during heating, causing a change in the experimental absorbance. However, this hypothesis cannot hold true in our case for different reasons: (1) the intensity increase is too high (the absorbance is more than doubled, Fig. 8.5) for single crystals; (2) although the measurements were done on non-oriented sections, the same kind of behavior has been observed on different sections of riebeckite, as well as on potassic-ferro-richterite, and we can hardly presume that all studied fragments had the same orientation with respect to the beam; (3) an intensity increase, although less pronounced, is observed also when collecting the data on powders (Fig. 8.6) and, (4) all measurements described in this Thesis have been done with unpolarized light.

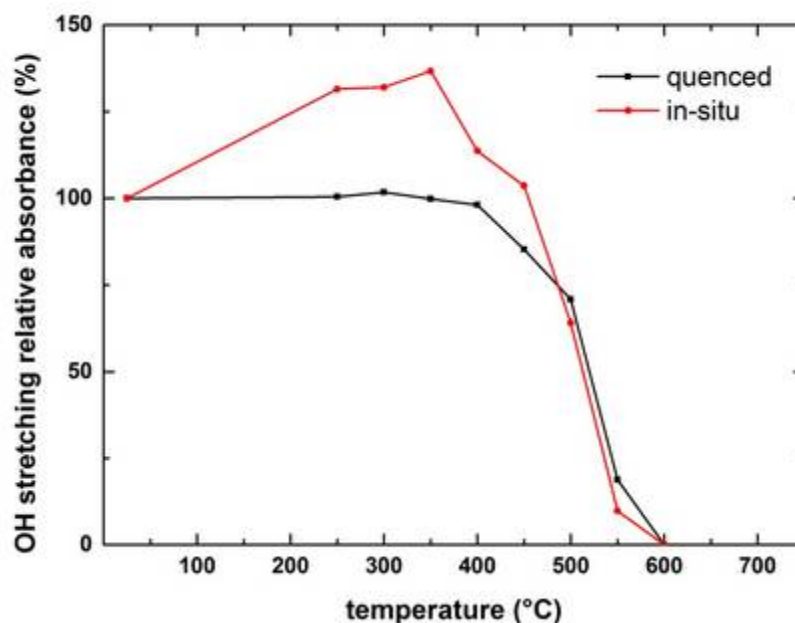


**Figure 8.6.** Comparison of the relative absorbance of the OH-stretching band measured in situ versus quenched samples as a function of  $T$ . Spectra collected on pure powdered riebeckite from Malawi; integration range  $3711\text{--}3560\text{ cm}^{-1}$ .

There is an additional point to consider: isothermal experiments, done at temperatures between  $450$  and  $500^\circ\text{C}$  on powdered riebeckite (Section 7.4) yielded a decrease in the OH-absorbance with time. On the other hand, the IR spectra collected during isothermal experiments on three doubly-polished crystals at  $500$ ,  $520$  and  $540^\circ\text{C}$  respectively, showed a significant increase in absorbance of the OH-stretching band before the onset of deprotonation (Section 7.1). Therefore, although the absorbance increase measured during the heating experiments could be explained by a change in the molar absorptivity ( $\epsilon$ ) with temperature (Chapter 5), the increase observed in the isothermal experiments cannot be explained in the same way.

This point is unresolved at the present, however we suspect that this kind of behaviour is in some way connected to the deprotonation mechanism of Fe-amphiboles. Work on Fe-free samples should be done to help solving this conundrum. The spatial distribution of the OH-absorbance on doubly-polished single crystals was studied using an FPA detector on quenched samples (Section 7.2). An

homogeneous absorbance decrease was found after subsequent heat-treatments at 520°C. FTIR mapping was carried out *in situ* at 520°C at different points (Section 7.3). From what observed, the increase in absorbance with time at HT, in the early stages of the experiments, seems to be restricted to the internal part of the crystal and not the in the rim. The reason for this is still unclear; further studies are needed to understand whether it is related to the protons migration through the structure, or is just a thermal effect.

---

## References

---

- Addison, C.C., Addison, W.E., Neal, G.H., and Sharp, J.H (1962a). Amphiboles. Part I. The oxidation of crocidolite. *Journal of Chemical Society*, 1962. 1468-1471.
- Addison, W.E., Neal, G.H., and Sharp, J.H (1962b). Amphiboles. Part II. The kinetics of oxidation of crocidolite. *Journal of Chemical Society*, 1962. 1472-1475.
- Addison, W.E. and Sharp, J.H. (1962a). Amphiboles. Part III. The reduction of crocidolite. *Journal of Chemical Society*, 1962. 3693-3698.
- Addison, W.E. and Sharp, J.H. (1962b). A mechanism for the oxidation of ferrous iron in hydroxylated silicates. Meeting of the Clay Minerals Group of the Mineralogical Society, Leeds, April 1962. 73-79.
- Addison, W.E. and Sharp, J.H. (1968). Redox behavior of iron in hydroxylated silicates. *Eleventh Conference on Clays and Clay Minerals* 1968, 95-104.
- Addison, W.E. and White, A.D. (1968). The oxidation of Bolivian crocidolite. *Mineralogical Magazine* 36, 1968. 791-796.
- Avrami, M. (1939). Kinetics of Phase Change. I. General Theory. *Journal of Chemical Physics*, 7. 1103-1112.
- Avrami, M. (1940). Kinetics of Phase Change. II. Transformation-Time Relations for Random Distribution of Nuclei. *Journal of Chemical Physics*, 8. 212-224.
- Avrami, M. (1941). Kinetics of Phase Change. III. Granulation, Phase Change, and Microstructure. *Journal of Chemical Physics*, 9. 177-184.
- Bancroft, G.M. and Maddock, A.G. (1967). Determination of cation distribution in the cummingtonite-grunierite series by Mössbauer spectra. *Amer. Mineral.* 52. 1009–1026.
- Bancroft, G.M. and Burns, R.G. (1969). Mössbauer and absorption spectral study of alkali amphiboles. *Min. Soc. Amer. Special Pap.* 2. 137 – 148.
- Barnes, V. E. (1930). Changes in orneblende at about 800°C. *American Mineralogist*, 15. 393-417.

- Brown, L. D. (1981). The bond-valence method: an empirical to chemical structure and bonding. *Structure and Bonding in Crystals II* (M. O'Keffee and A. Navrotsky, eds.) Academic Press, N. Y.. 1-30.
- Brown, L. D. (1992). Chemical and steric constraints in inorganic solids. *Acta Crystallogr.* B48. 553-572.
- Brown, L. D. and Altermatt D. (1985). Bond-valence parameters obtained from a systematic analysis of the inorganic crystal structure database. *Acta Crystallogr.* B41. 244-247.
- Brown, L. D. and Shannon R.D. (1973). Empirical bond-strength bond-length curves for oxides. *Acta Crystallogr.* A29. 266-282.
- Bruker (2003) SAINT Software Reference Manual. Version 6. Bruker AXS Inc., Madison, Wisconsin, USA.
- Burns, P.C. and Strens, R. G. J. (1966). Infrared study of the hydroxyl bonds in clinoamphiboles. *Science* 153. 890-892.
- Busing, W.R., and Levy, H.A. (1964). The effect of thermal motion on the estimation of bond lengths from diffraction measurement. *Acta Crystallographica*, 17. 142-146.
- Cannillo, E., Germani, G., & Mazzi, F. (1983). New crystallographic software for Philips PW11000 single crystal diffractometer. CNR Centro di Studio per la Cristallografia, Internal Report 2.
- Clark, R.N., King, T.V.V., Klejwa, M., Swayze, G.A., Vergo, N. (1990). High spectral resolution reflectance spectroscopy of minerals. *J. Geophys. Res.*, 95. 12653-12680.
- Carbone, M., Ballirano, P., Caminiti, R. (2008). Kinetics of gypsum dehydration at reduced pressure: an energy dispersive X-ray diffraction study. *European Journal of Mineralogy*, 20. 621-627.
- Della Ventura, G. (1992). Recent developments in the synthesis and characterization of amphiboles. Synthesis and crystal-chemistry of richterites. *Trends in Mineralogy*, 1. 153-192.
- Della Ventura, G., Robert, J.-L., Hawthorne, F.C. (1996). Infrared spectroscopy of synthetic (Ni,Mg,Co)-potassium-richterite. *Geochimica and Cosmochimica Acta*, vol. spec. 5. 55-63.

- Della Ventura, G., Robert, J.-L., Raudsepp, M., Hawthorne, F.C., Welch, M. (1997). Site occupancies in synthetic monoclinic amphiboles: Rietveld structure-refinement and infrared spectroscopy of (nickel, magnesium, cobalt)-richterite. *American Mineralogist*, 82. 291-301.
- Della Ventura, G., Robert, J.-L., Hawthorne, F.C., Raudsepp, M., Welch, M.D. (1998). Contrasting  $^{[6]}\text{Al}$  ordering in synthetic Mg- and Co-pargasite. *Canadian Mineralogist*, 36. 1237-1244.
- Della Ventura, G., Redhammer, G.J., Iezzi, G., Hawthorne, Papin, A., Robert, J.-L. (2005a). A Mössbauer and FTIR study of synthetic amphiboles along the magnesioriebeckite – ferri-clinoholmquistite join. *Physics and Chemistry of Minerals*, 32.103-113.
- Della Ventura, G., Iezzi, G., Redhammer, G.J., Hawthorne, F.C., Scaillet, B., Novembre, D. (2005b). Synthesis and crystal-chemistry of alkali amphiboles in the system  $\text{Na}_2\text{O-MgO-FeO-Fe}_2\text{O}_3\text{-SiO}_2\text{-H}_2\text{O}$  as a function of  $f_{\text{O}_2}$ . *American Mineralogist*, 90. 1375-1383.
- Della Ventura, G., Oberti, R., Hawthorne, F.C., Bellatreccia, F. (2007). Single-crystal FTIR study Ti-rich pargasites from Lherz: the spectroscopic detection of  $^{\text{O}3}\text{O}^{2-}$  in amphiboles. *American Mineralogist*, 92. 1645-1651.
- Della Ventura, G. *et al.* (2015) *Can Min* (to be submitted).
- Demouchy, S. and Mackwell, S. (2003). Water diffusion in synthetic iron-free forsterite. *Physics and Chemistry of Minerals*, 30. 486–494.
- Ernst, W.G. (1962). Synthesis, stability relations and occurrence of riebeckite and riebeckite - arfvedsonite solid solutions. *J. Geol.* 70. 689–736.
- Ernst, W.G. and Wai, M. (1970). Mössbauer, infrared, X-ray and optical study of cation ordering and dehydrogenation in natural and heat-treated sodic amphiboles. *The American Mineralogist* 55, July-august, 1970. 1226-1258.
- Francis, G.H. (1955). Gedrite from Glen Urquhart, Inverness-Shire. *Mineralogical Magazine* 30, 1955. 709-716.
- Farver, J.R. and Yund R.A. (1991). Measurement of oxygen grain boundary diffusion in natural, fine grained, quartz aggregates. *Geochimica Cosmochimica Acta*, 55. 1597-1607.



- Fortier, S.M. and Giletti B.J. (1991). Volume self-diffusion of oxygen in biotite, muscovite, and phlogopite micas. *Geochimica Cosmochimica Acta*, 55. 1319-1330.
- Fukuda, J., Shinoda, K., Nakashima, S., Miyoshi, N., Aikawa, N. (2009). Polarized infrared spectroscopic study of diffusion of water molecules along structure channels in beryl. *American Mineralogist*, 94. 981-985.
- Giampaolo, C., and Putnis, A. (1989). The kinetics of dehydration and order-disorder of molecular H<sub>2</sub>O in Mg-cordierite. *European Journal of Mineralogy*, 1. 193-202.
- Gottschalk, M. and Andrut, M. (1998). Structural and chemical characterization of synthetic (Na,K)-richterite solid-solutions by EMP, HRTEM, XRD and OH-valence vibrational spectroscopy. *Phys. Chem. Miner.*, 25. 101-111.
- Graham, C.M. (1981). Experimental hydrogen isotope studies III: Diffusion of hydrogen in hydrous minerals, and stable isotope exchange in metamorphic rocks. *Contributions to Mineralogy and Petrology*, 76. 216-228.
- Hafner, S.S. and Ghose S. (1971). Iron and magnesium distribution in cumingtonites, (Fe,Mg)<sub>7</sub>Si<sub>8</sub>O<sub>22</sub>(OH)<sub>2</sub>. *Z Krist* 133. 301–326.
- Hancock, J.D., Sharp, J.H. (1972). Method of Comparing Solid-State Kinetic Data and Its Application to the Decomposition of Kaolinite, Brucite, and BaCO<sub>3</sub>. *Journal of the American Ceramic Society*, 55. 74-77.
- Hawthorne, F.C. (1978). The crystal structure and site chemistry of fluor-riebeckite. *Can. Min.* 16. 187–194.
- Hawthorne, F.C. (1983). The crystal chemistry of amphiboles. *The Canadian Mineralogist*, Vol. 35. 173–480.
- Hawthorne, F.C., Ungaretti, L. & Oberti, R. (1995). Site populations in minerals: terminology and presentation of results. *Canadian Mineralogist*, 33. 907–911.
- Hawthorne, F.C., Della Ventura, G., Robert, J.L. (1996). Short-range order and long-range order in amphiboles: A model for the interpretation of infrared spectra in the principal OH-stretching region. *Geochimica and Cosmochimica Acta*, vol. spec. 5. 49-54.
- Hawthorne, F.C. (1997). Short-range order in amphiboles: A bond-valence approach. *The Canadian Mineralogist*, Vol. 35. 201–216.

- Hawthorne, F.C., Della Ventura, G., Oberti R., Robert., J.L. and Iezzi, G. (2005). Short-range order in minerals: Amphiboles. *Can. Min.* 43. 1895–1920.
- Hawthorne, F. C. and Della Ventura, G. (2007). Short-range order in amphiboles. In, F.C. Hawthorne, R. Oberti, G. Della Ventura, and A. Mottana (eds.). *Amphiboles: crystal-chemistry, occurrence, and health issues. Reviews in Mineralogy and Geochemistry*, 67. 173-222.
- Hawthorne, F.C. and Oberti, R. (2007). Amphiboles: Crystal Chemistry. *Rev. Mineral. Geochem.* 67. 1–54.
- Hawthorne, F.C., Oberti, R., Harlow, G.E., Maresch, W.V., Martin, R.F., Schumacher, J.C., and Welch, M.D. (2012). Nomenclature of the amphibole supergroup. *American Mineralogist*, 97. 2031-2048.
- Hodgson, A.A., Freeman, A.G., Taylor, H.F.V. (1965). The thermal decomposition of crocidolite from Koegas, South Africa. *Mineralogical Magazine* 35, 1965. 5-29.
- Iezzi, G., Cámara, F., Della Ventura, G., Oberti, R., Pedrazzi, G., Robert, J.-L. (2004). Synthesis, crystal structure and crystal-chemistry of ferri-clinoholmquistite,  $\text{Li}_2\text{Mg}_3\text{Fe}^{3+}_2\text{Si}_8\text{O}_{22}(\text{OH})_2$ . *Physics and Chemistry of Minerals*, 31. 375-385.
- Iezzi, G., Della Ventura, G., Hawthorne, F.C., Pedrazzi, G., Robert, J.-L., Novembre, D. (2005). The  $(\text{Mg},\text{Fe}^{2+})$  substitution in ferri-clinoholmquistite,  $\square\text{Li}_2(\text{Mg},\text{Fe}^{2+})_3\text{Fe}^{3+}_2\text{Si}_8\text{O}_{22}(\text{OH})_2$ . *European Journal of Mineralogy*, 17. 733-740.
- Ingrin, J., Blanchard, M. (2000). Hydrogen mobility in single crystal kaersutite. EMPG VIII, *Journal of Conference Abstracts*, 5. 52.
- Jibao G. and Yaqian Q. (1997). Hydrogen isotope fractionation and hydrogen diffusion in the tourmaline-water system. *Geochimica Cosmochimica Acta*, 21. 4679-4688.
- Karato, S. and Wang, D. (2012). Electrical conductivity of minerals and rocks. In Karato S. (ed) *Physics and chemistry of the deep earth*. Wiley.
- Keppler, H., Bagdassarov, N.S. (1993). High-temperature FTIR spectra of  $\text{H}_2\text{O}$  in rhyolite melt to 1300 °C. *American Mineralogist*, 78. 1324-1327.
- Larson, A.C. and Von Dreele, R.B. "General Structure Analysis System (GSAS)", Los Alamos National Laboratory Report LAUR 86-748 (2000).

- Laukamp, C., Termin, K.A., Pejčić, B., Haest, M., Cudahy, T. (2012). Vibrational spectroscopy of calcic amphiboles - applications for exploration and mining. *Eur. J. Mineral.*, 24. 863-878.
- Law, A.D. (1976). A model for the investigation of Hydroxyl spectra of amphiboles. In *the Physics and Chemistry of Minerals and Rocks* (ed. R.G.J. Strens). 677–686.
- Libowitzky, E. and Rossman, G.R. (1997). An IR absorption calibration for water in minerals. *American Mineralogist*, 82. 1111–1115.
- Mustard, J.F. (1992). Chemical analysis of actinolite from reflectance spectra. *American Mineralogist*, 77. 345–358.
- Oberti R., Ungaretti L., Cannillo E., Hawthorne F.C. (1992). The behaviour of Ti in amphiboles: I. Four- and six-coordinated Ti in richterites. *European Journal of Mineralogy*, 4. 425-439.
- Oberti R., Hawthorne F.C., Cannillo E., Càmarà F. (2007). Long-range order in amphiboles. In: *Amphiboles: Crystal Chemistry, Occurrence and Health Issues* published by F.C. Hawthorne, R. Oberti, G. Della Ventura e A. Mottana. *Reviews in Mineralogy and Geochemistry*, vol. 67. 125-172.
- Oberti, R., Hawthorne, F.C., Cannillo, E., Càmarà, F. (2007). Long-range order in amphiboles. *Rev. in Mineral. and Geochem.* 67. 125-172.
- Oberti, R., Zema, M., Boiocchi, M. (2012). High-temperature behaviour of ferroholmquistite: thermal expansion and dehydrogenation. 41° Congresso AIC, Verona, 11-14 settembre 2012, Abstracts. 136.
- Oberti, R., Boiocchi, M., Welch, M.D., Zema, M. (2013). Towards a model for HT behaviour of (orthorhombic and monoclinic) amphiboles. GAC-MAC Meeting, Winnipeg, Canada, Abstracts. 153.
- Oberti, R., Boiocchi, M., Zema, M., Della Ventura, G. (2016). Synthetic potassic-ferro-richterite: 1. Composition, crystal structure refinement and HT behavior by in operando single-crystal X-ray diffraction. *Canadian Mineralogist* in press.
- Okumura, S. and Nakashima, S. (2005). Molar absorptivities of OH and H<sub>2</sub>O in rhyolitic glass at room temperature and at 400–600 °C. *American Mineralogist*, 90. 441–447.
- Paterson, M.S. (1982). The determination of hydroxyl by infrared absorption in quartz, silicate glasses and similar materials. *Bulletin de Mineralogy*, 105. 20–29.

- Pauling, L., (1961). *Nature of the Chemical Bond*, Third Edition. Cornell University Press, New York, 1961. 547.
- Phillips, M.W., Popp, R.K., Clowe, C.A. (1988). Structural adjustments accompanying oxidation-dehydrogenation in amphiboles. *Amer. Mineral.*, 73. 500-506.
- Phillips, M.W., Popp, R.K., Clowe, C.A. (1991). A structural investigation of oxidation effects in air-heated grunerite. *Amer. Mineral.*, 76. 1502-1509.
- Putnis, A. (1992). *Introduction to mineral science*. Cambridge University Press. 457.
- Putnis, A., Winkler B., Fernandez-Diaz L. (1990). In situ IR spectroscopic and thermogravimetric study of the dehydration of gypsum. *Mineralogical Magazine*, 54. 123-128.
- Rancourt, D.G. and Ping, J.Y. (1991). Voigt-based methods for arbitrary-shape static hyperfine parameter distributions in Mössbauer spectroscopy. *Nuclear Instruments and Methods in Physics Research B (NIMB)*, 58. 85-97.
- Rancourt, D.G., McDonald, A.M., Lalonde, A.E., Ping, J.Y. (1993). Mössbauer absorber thickness for accurate site populations in Fe-bearing minerals. *American Mineralogist*, 78. 1-7.
- Rancourt, D.G., Ping, J.Y., Boukili, B., Robert, J.-L. (1996). Octahedral-site Fe<sup>2+</sup> quadrupole splitting distributions from Mössbauer spectroscopy along (OH, F)-annite join. *Physics and Chemistry of Minerals*, 23. 63-71.
- Radica, F., Della Ventura, G., Bellatreccia, F., Cestelli Guidi, M. (2015). HT-FTIR micro-spectroscopy of cordierite: the CO<sub>2</sub> absorbance from in situ and quenched experiments. *Phys. Chem. Miner.*, (in press).
- Redhammer, G.J. and Roth, G. (2002). Crystal structure and Mössbauer spectroscopy of the synthetic amphibole potassic-ferri-ferrorichterite at 298 K and low temperatures (80–110 K) *Eur. J. Mineral.* 2002, 14. 105–114
- Reynard, B., Mibe, K., Van de Moortèle, B. (2011). Electrical conductivity of the serpentinised mantle and fluid flow in subduction zones. *Earth and Planetary Science Letters* 307. 387–394.
- Robert, J.L., Della Ventura, G. and Thauvin, J.L. (1989). The infrared OH-stretching region of synthetic richterites in the system Na<sub>2</sub>O-K<sub>2</sub>O-CaO-MgO-SiO<sub>2</sub>-H<sub>2</sub>O-HF. *European Journal of Mineralogy*, 1. 203-211.
- Sheldrick, G.M. (1996). SADABS Siemens Area Detector Absorption Correction Program. University of Göttingen, Göttingen.

- Sheldrick, G.M. (2008). A short history of SHELX. *Acta Cryst.*, A64. 112–122.
- Schmidbauer E., Kunzmann T., Fher T., Hochleitner R. (2000). Electrical resistivity and  $^{57}\text{Fe}$  Mössbauer spectroscopy of Fe-bearing calcic amphiboles. *Phys Chem Miner*, 27. 347-356.
- Shannon, R.D. (1976). Revised effective ionic radii and systematic studies of interatomic distances in halides and chalcogenides, *Acta Cryst.*, A32. 751–767.
- Strens, R.S.J. (1966). Infrared study of cation ordering and clustering in some (Fe, Mg) amphibole solid solutions. *Chem. Commun.* 519.
- Strens, R.S.J. (1974). The common chain, ribbon and ring silicates. In V.C. Farmer, Ed., *The infrared spectra of minerals*, 4. Mineralogical Society Monograph, London. 305-330.
- Susta, U., Della Ventura, G., Bellatreccia, F., Hawthorne, F.C., Boiocchi, M., Oberti, R. (2016). HT-FTIR spectroscopy of riebeckite. (to be submitted).
- Tokiwai, K. and Nakashima, S. (2010a). Integral molar absorptivities of OH in muscovite at 20 to 650 °C by in-situ high-temperature IR microspectroscopy. *American Mineralogist*, 95. 1052–1059.
- Tokiwai, K., Nakashima, S. (2010b). Dehydration kinetics of muscovite by in situ infrared microspectroscopy. *Physics and Chemistry of Minerals*, 37. 91-101.
- Ungaretti, L., Oberti R., Rossi G. (1978). Variazioni cristallografiche indotte da riscaldamento a 650°C su una riebeckite metamorfica. *Convegno SIMP*, Napoli 13-14 Ottobre 1978. *Rendiconti S.I.M.P.* (1979), 35-1. 464.
- Ungaretti, L. (1980). Recent developments in X-ray single crystal diffractometry applied to the crystal-chemical study of amphiboles. *Godisnjak Jugoslavenskog Centra za Kristalografiju*, 15. 29-65.
- Wang, L., Zhang, M., Redfern, S.A.T., Zang, Z.Y. (2002). Dehydroxylation and transformations of the 2:1 phyllosilicate pyrophyllite at elevated temperatures: an infrared spectroscopic study. *Clays and Clay Minerals*, 50. 272-283.
- Wang, D., Guo, Y., Yu, Y., Karato, S. (2012). Electrical conductivity of amphibole-bearing rocks: influence of dehydration. *Contribution to Mineralogy and Petrology* 164. 17–25
- Wang, D., Guo, Y., Yu, Y., Karato, S. (2013). Electrical conductivity of talc aggregates at 0.5 GPa: influence of dehydration *Physics and Chemistry of Minerals*, 40. 11–17

- Ward, J.R. (1975). Kinetics of talc dehydroxylation. *Thermochimica Acta*, 13. 7-14.
- Welch, M.D., Cámara, F., Della Ventura, G., Iezzi, G. (2007). Non-ambient in situ studies of amphiboles. In, F. C. Hawthorne, R. Oberti, G. Della Ventura, A. Mottana, eds., *Amphiboles: Crystal Chemistry, Occurrence, and Health Issues*, *Reviews in Mineralogy and Geochemistry*, 67. 223–260.
- Welch, M.D., Cámara, F., Oberti, R. (2011). Thermoelasticity and high-T behaviour of anthophyllite. *Physics and Chemistry of Minerals*, 38. 321–334.
- Withers, A.C., Zhang, Y., and Behrens, H. (1999). Reconciliation of experimental results on H<sub>2</sub>O speciation in rhyolitic glass using in situ and quenching techniques. *Earth and Planetary Science Letters*, 173. 343–349.
- Yamagishi, H., Nakashima, S., and Ito, Y. (1997). High temperature infrared spectra of hydrous microcrystalline quartz. *Physics and Chemistry of Minerals*, 24. 66–74.
- Zema, M., Welch, M.D., and Oberti, R. (2012). High-T behaviour of gedrite: thermoelasticity and dehydrogenation. *Contributions to Mineralogy and Petrology*, 163. 923-937.
- Zhang, M., Wang, L., Hirai, S., Redfern, S.A.T., Salje EKH (2005). Dehydroxylation and CO<sub>2</sub> incorporation in annealed mica (sericite): an infrared spectroscopic study. *American Mineralogist*, 90. 173-180.
- Zhang, M., Salje, E.K.H., Carpenter, M.A., Wang, J.Y., Groat, L.A., Lager, G.A., Wang L., Beran, A., Bismayer, U. (2007). Temperature dependence of IR absorption of hydrous/hydroxyl species in minerals and synthetic materials. *American Mineralogist*, 92. 1502-1517.
- Zhang, M., Redfern, S.A.T., Salje, E.K.H., Carpenter, M.A., and Wang, L. (2010). H<sub>2</sub>O and the dehydroxylation of phyllosilicates: An infrared spectroscopic study. *American Mineralogist*, 95. 1686–1693.